



# DEPARTMENT OF PHYSICS

UNIVERSITY OF CAPE TOWN

IYUNIVESITHI YASEKAPA • UNIVERSITEIT VAN KAAPSTAD

Search for  $tWZ$  production in the Full Run 2 ATLAS  
dataset using events with four leptons

Jake Reich

Student Number: RCHJAK001

Supervisor: Dr. James Keaveney

Co-Supervisor: Dr. Sahal Yacoob

<sup>1</sup>

A thesis submitted in fulfilment  
of the requirements for the degree of  
Master in Science

August 2021

# Abstract

3 The search for  $tWZ$  production using  $139 \text{ fb}^{-1}$  of  $pp$  collision data at a centre-of-mass energy of  $\sqrt{s} = 13$   
4 TeV, recorded by the ATLAS experiment at CERN, is presented. Events that contain exactly four  
5 leptons (electrons or muons) are selected. Additional criteria are applied based on the number of jets,  
6 the number of  $b$ -tagged jets and the number of  $Z$  boson candidates to define signal and control regions.  
7 The large  $t\bar{t}Z$  and  $ZZ$  backgrounds are distinguished from signal by a BDT-based algorithm. Inputs to  
8 the BDT-based algorithm include, a kinematic reconstruction algorithm which reconstructs leptonically  
9 decaying top quarks and a variable constructed from the output of a BDT-based algorithm which aims to  
10 classify  $\ell b$  systems originating from top quarks. The expected signal strength is extracted via a blinded  
11 maximum-likelihood fit to multiple signal and control regions. The expected signal strength was measured  
12 as,  $\mu(tWZ) = 1.91^{+0.95}_{-0.82}$ , leading to an expected significance of  $1.44\sigma$ . An expected upper limit on the  
13 signal strength is set to  $\mu_{up}^{exp} = 1.61^{+2.35}_{-1.16}$ . Furthermore, a combined blinded maximum-likelihood fit was  
14 performed across the tetralepton channel and an independent analysis of the trilepton channel, to further  
15 increase the sensitivity this analysis to the  $tWZ$  cross section. The expected signal strength was measured  
16 as,  $\mu(tWZ) = 1.80^{+0.70}_{-0.65}$ , leading to an expected significance of  $1.61\sigma$ . An expected upper limit on the  
17 signal strength is set to  $\mu_{up}^{exp} = 1.43^{+2.04}_{-1.03}$ .

# Declaration

19 *I certify that this assignment/report is my own work, based on my personal study and/or research and  
20 that I have acknowledged all material and sources used in its preparation, whether they be books, articles,  
21 reports, lecture notes, and any other kind of document, electronic or personal communication. I also  
22 certify that this assignment/report has not previously been submitted for assessment in any other unit,  
23 except where specific permission has been granted from all unit coordinators involved, or at any other time  
24 in this unit, and that I have not copied in part or whole or otherwise plagiarised the work of other students  
25 and/or persons.*

# Acknowledgements

# Contents

27

28	<b>1 Introduction</b>	7
29	<b>2 Theory</b>	8
30	2.1 Standard Model of Particle Physics . . . . .	8
31	2.1.1 The Top Quark . . . . .	10
32	2.2 $tWZ$ . . . . .	12
33	2.2.1 Tetralepton Channel . . . . .	12
34	2.2.2 Comparison to Trilepton Channel . . . . .	13
35	<b>3 The ATLAS Experiment and Detector</b>	15
36	3.1 The ATLAS Experiment . . . . .	15
37	3.1.1 Large Hadron Collider (LHC) . . . . .	15
38	3.2 The ATLAS Detector . . . . .	17
39	3.2.1 Coordinate System and Kinematics . . . . .	18
40	3.2.2 Inner Detector . . . . .	18
41	3.2.3 Electromagnetic and Hadronic Calorimeters . . . . .	19
42	3.2.4 Muon Spectrometer . . . . .	19
43	3.2.5 Trigger and Data Acquisition System . . . . .	19
44	3.2.6 Particle Identification and Object Reconstruction . . . . .	19
45	<b>4 The search for <math>tWZ</math> production using events with four leptons</b>	22
46	4.1 Data and Monte Carlo Simulation . . . . .	22
47	4.1.1 Data Samples . . . . .	22
48	4.1.2 Monte Carlo Samples . . . . .	23
49	4.1.3 Trigger Strategy . . . . .	24
50	4.2 Physics objects . . . . .	26
51	4.2.1 Leptons . . . . .	26
52	4.2.2 Jets . . . . .	27
53	4.2.3 $b$ -tagging . . . . .	27
54	4.2.4 Overlap Removal Procedure . . . . .	28
55	4.3 Kinematic cuts . . . . .	28
56	4.4 Regions and Event Selection . . . . .	28
57	4.4.1 Optimization studies for event selection . . . . .	29

58	4.5	Signal and Control Regions . . . . .	32
59	4.5.1	$tWZ$ OF SR . . . . .	33
60	4.5.2	$tWZ$ SF SR . . . . .	34
61	4.5.3	$t\bar{t}Z$ CR . . . . .	34
62	4.5.4	$ZZb$ CR . . . . .	37
63	4.5.5	$(tWZ)_{\text{fake}}$ CR . . . . .	39
64	4.6	Fake Lepton Estimation . . . . .	39
65	4.7	Improving signal vs background discrimination . . . . .	42
66	4.7.1	Two Neutrino Scanning Method ( $2\nu\text{SM}$ ) Algorithm . . . . .	42
67	4.7.2	Boosted Decision Trees . . . . .	48
68	4.7.3	Object-level BDT . . . . .	49
69	4.7.4	Event-level BDT . . . . .	56
70	4.8	Systematic Uncertainties . . . . .	62
71	4.8.1	Experimental uncertainties . . . . .	62
72	4.8.2	Theoretical uncertainties . . . . .	63
73	4.8.3	Generic shape systematic uncertainties . . . . .	64
74	4.9	Analysis Pipeline and TRExFitter . . . . .	64
75	4.9.1	Fitting Procedure . . . . .	65
76	4.10	Results . . . . .	67
77	4.10.1	Tetralepton Channel . . . . .	68
78	4.10.2	Trilepton and Tetralepton Channels . . . . .	70
79	<b>5</b>	<b>Summary and Conclusions</b>	<b>76</b>

80

# Chapter 1

81

## Introduction

82 The production of a single top quark in association with a  $W^\pm$  and  $Z$  boson ( $tWZ$ ) at the CERN LHC is  
83 sensitive to both the neutral and charged electroweak couplings of the top quark as the process involves  
84 the simultaneous production of a  $W$  boson and a  $Z$  boson in association with the top quark. Due to the  
85 very large coupling of the top quark to the Higgs boson, the electroweak couplings of the top quark are a  
86 theoretically well-motivated area in which to search for the first signs of new physics [80, 52] that could  
87 offer a resolution to the Hierarchy Problem [62, 30]. The recent lack of signs of new physics from LHC  
88 data tells us that new physics is either very heavy, or is very weakly coupled to Standard Model particles,  
89 therefore signs of new physics might only be observed in anomalous rates of well-chosen processes. A  
90 prime example of such a process is  $tWZ$ . This has an extremely low production cross section ( $\approx 160$  fb  
91 for  $\sqrt{s} = 13$  TeV [25]), meaning that it is an extremely rare process and subsequently, it has never been  
92 observed by any particle physics experiment.

93

94 The latest datasets recorded by the ATLAS experiment at the CERN LHC are sufficiently large to  
95 potentially allow for an observation of  $tWZ$  production. In this analysis, the Full Run 2 dataset recorded  
96 by ATLAS is used to search for  $tWZ$  production in the tetralepton channel ( $tWZ$  with exactly four  
97 final state leptons). A kinematic reconstruction technique is used which aims to discriminate between  
98  $tWZ$  and our most prominent background process,  $t\bar{t}Z$ . In addition to this, Machine Learning techniques  
99 are implemented to further isolate our  $tWZ$  signal. Backgrounds from Standard Model (SM) processes  
100 including those in which one or more leptons originate from the semileptonic decay of a heavy hadron  
101 or a photon conversion are estimated by fitting predictions from simulation to data in dedicated control  
102 regions. As this work forms the basis of an official ATLAS analysis, only blinded results are shown.  
103 A maximum likelihood fit is performed over our two  $tWZ$  signal regions and three control regions, to  
104 measure the cross section of  $tWZ$  in the tetralepton channel. In this thesis only the tetralepton channel  
105 is explored, however, the results of a combined fit that includes an entirely independent analysis of the  
106 trilepton channel is presented with no overlap of events between the regions defined for these channels.

107

# Chapter 2

108

## Theory

### 2.1 Standard Model of Particle Physics

110 The SM is a model based on Quantum Field Theory (QFT) which classifies all known elementary particles  
 111 and describes their interactions. It is a well-tested model and has shown to be hugely successful in  
 112 describing experimental data to great precision [8, 7]. For example, in the top quark sector, the  $t\bar{t}$  cross  
 113 section predictions have been confirmed to 3.9% accuracy [40, 71]. It incorporates three of the four  
 114 fundamental forces of nature: the electromagnetic, the weak and the strong forces. In Figure 1, all known  
 115 elementary particles described by the SM, are shown.

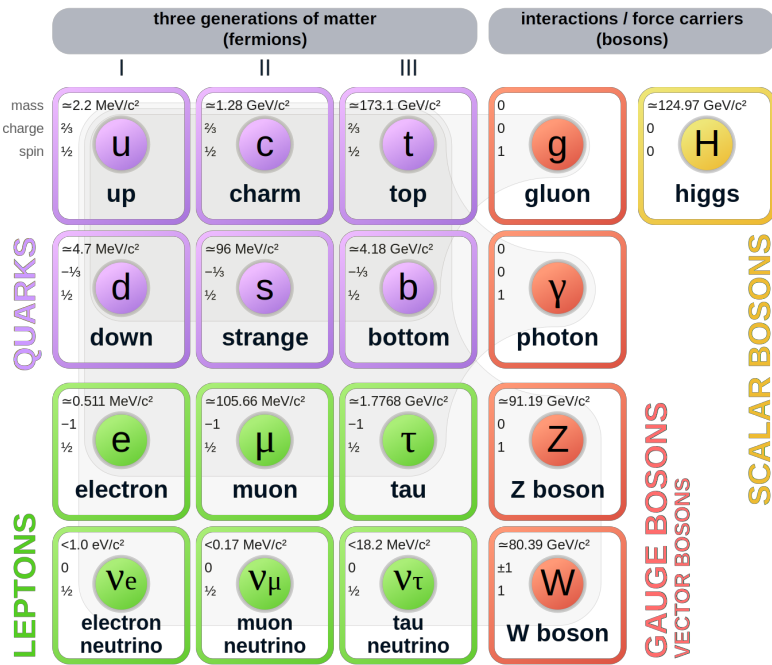


Figure 1: A summary of the elementary particles described by the SM [75] is shown. Fermions are shown on the left, with quarks shown in purple and leptons shown in green. Bosons are shown on the right, with gauge bosons shown in red and the Higgs boson shown in yellow. The mass, electric charge and spin of each particle is shown on the top left of each particle's block.

116 Particles in the SM are uniquely described by their quantum numbers: electric charge and spin. The  
117 SM particles are split into main two classes, based off their spin quantum numbers. Particles which  
118 have half-integer spin are called fermions, and those which have integer spin are called bosons. Fermions  
119 are further divided into three generations, each comprising of two quarks, one charged lepton and one  
120 neutrino. In a generation, the more massive quark has an electric charge of  $+2/3$  (up-type) and the less  
121 massive quark has an electric charge of  $-1/3$  (down-type). All charged leptons have an electric charge  
122 of  $-1$  and all neutrinos are electrically neutral. The masses of the particles in a generation increase  
123 with increasing generation number, with generation 1 particles being the least massive and generation 3  
124 particles being the most massive. Quarks carry electric and colour charge, and can therefore interact via  
125 the electromagnetic, weak and strong forces. Colour charge can take on three values: red, green and blue.  
126 It is important to note that colour charge is completely unrelated to the everyday meaning of colour, and  
127 it just represents the quantum state of the particle. Due to colour confinement [100], quarks cannot be  
128 isolated from one another. They exist in colourless bound states, called hadrons, consisting of two or more  
129 quarks. Hadrons consisting of an even number of quarks are known as mesons and those consisting of an  
130 odd number of quarks are known as baryons. On the other hand, charged leptons (electron ( $e$ ), muon ( $\mu$ )  
131 and tau ( $\tau$ )) only carry electric charge and can therefore interact electromagnetically and weakly, but not  
132 through the strong interaction. The electric and colour neutral fermions, neutrinos, can only interact via  
133 the weak force.

134  
135 Particles are able to interact with one-another via the exchange of a gauge boson (boson with spin-1).  
136 Photons are massless, spin-1 gauge bosons which mediate electromagnetic interactions between particles  
137 which carry electric charge, such as quarks and charged leptons ( $e$ ,  $\mu$  and  $\tau$ ). The weak interaction is  
138 mediated by three massive gauge bosons, the electrically charged  $W^+$  and  $W^-$  bosons and the electrically  
139 neutral  $Z$  boson. Gluons are massless, spin-1 gauge bosons which mediate strong interactions between  
140 particles which carry colour charge, such as quarks. Since gluons carry colour charge, they interact with  
141 themselves. The massive, spin-0, electrically neutral Higgs boson mediates the Higgs field which gives  
142 mass to the  $W^\pm$  and  $Z$  bosons via the so-called Brout-Englert-Higgs mechanism [46, 58, 57]. The Brout-  
143 Englert-Higgs mechanism induces spontaneous electroweak symmetry breaking to provide mass terms for  
144 the  $W^\pm$  and  $Z$  bosons in the electroweak Lagrangian of the SM. All particles described in the SM have  
145 their own antiparticle, with the same mass, but opposite charges. Some particles, such as the photon, are  
146 their own antiparticle.

147  
148 Although the SM is hugely successful, it is incomplete and fails to describe certain observed phenomena.  
149 The most notable example being the absence of gravity. The gravitational force is  $\approx 10^{29}$  [92] weaker than  
150 the weak force, therefore quantum gravitational effects are expected to only become significant at energies  
151 much larger than that currently accessible by the LHC (known as the Planck scale  $\approx 10^9$  GeV) [62]. This  
152 large difference in strength between the weak force and gravity is known as the Hierarchy Problem.  
153 Cosmological observations infer that around 84% of the matter in the universe consists of gravitationally  
154 interacting matter known as dark matter [61]. None of the particles described in the SM are good dark  
155 matter candidates, therefore the SM only accounts for a small fraction of the total matter of the universe.  
156 The large discrepancy between the observed amount of matter and antimatter in the universe, sometimes

referred to as the matter-antimatter asymmetry, is not fully explained by the SM. Neutrinos in the SM are assumed to be massless, however observations of neutrino oscillations (neutrinos undergoing flavour change as they travel through space) imply that neutrinos do have mass [49]. Beyond the Standard Model (BSM) theories attempt to explain the phenomena which the SM cannot. For example, a popular extension to the SM, Supersymmetry (SUSY) introduces new particles to the SM which are counterparts to the existing SM particles with the same quantum numbers, except for their spins [64]. It provides elegant explanations to many shortcomings of the SM, however none of the supersymmetric particles described by SUSY have been observed experimentally [34].

### 2.1.1 The Top Quark

The top quark is the heaviest particle in the SM, with a mass of  $172.76 \pm 0.30$  GeV [55]. According to the SM, since the coupling to the Higgs boson is proportional to the mass of the interacting particle, the top quark is strongly coupled to the Higgs boson. Therefore, physics processes involving top quarks is a theoretically well-motivated area to search for new physics, since top quarks are the most likely particles to couple to new physics theories at the TeV scale. Its large mass also makes it highly unstable, with a mean lifetime of  $\approx 0.5 \times 10^{-24}$  s [55]. The top quark's lifetime is shorter than that of the hadronisation process, and it therefore decays before hadronising. The top quark can therefore be measured indirectly via its decay products. Top quarks almost always decay to a  $W$  boson and a  $b$ -quark ( $\frac{\Gamma(Wb)}{\Gamma(Wq(q=b,s,d))} = 0.957 \pm 0.034$  [55]). The  $b$ -quark is the second heaviest quark in the SM, however its lifetime is still longer than the hadronisation time scale [55]. In hadron collider experiments,  $b$ -quarks travel a short distance in the detector before hadronising to form jets. In Table 1, the dominant final state branching fractions of the top quark are shown.

Decay Mode	Branching Fraction ( $\frac{\Gamma_i}{\Gamma}$ )
$t \rightarrow Wb \rightarrow e\nu_e b$	$(11.10 \pm 0.30)\%$
$t \rightarrow Wb \rightarrow \mu\nu_\mu b$	$(11.40 \pm 0.20)\%$
$t \rightarrow Wb \rightarrow \tau\nu_\tau b$	$(10.70 \pm 0.50)\%$
$t \rightarrow Wb \rightarrow q\bar{q}b$	$(66.50 \pm 1.40)\%$

Table 1: The dominant final state branching fractions of the top quark [55] are shown.

Top quark decays with hadronic final states are more than twice as likely than those with leptonic final states. Final state decays to different lepton flavours are roughly equally probable.

180

Top quark production can be placed into two main categories: pair production ( $t\bar{t}$ ) and single-top production ( $t$ ) [88]. In the LHC, top quarks are mainly produced in pairs via strong interactions in gluon-gluon fusion ( $gg \rightarrow t\bar{t}$ ) or quark annihilation ( $q\bar{q} \rightarrow t\bar{t}$ ). Top quark production via gluon-gluon fusion is the dominating process [23]. The production cross section for  $t\bar{t}$  (leptonic final state) in  $pp$  collisions with  $\sqrt{s} = 13$  TeV was measured by ATLAS with a value of  $830 \pm 0.4(\text{stat}) \pm 36(\text{syst}) \pm 14(\text{lumi})$  pb [4], with good agreement between measurement and theoretical prediction.

187

188 Single top production occurs via the weak interaction. The most abundant production mechanisms leading  
 189 to single top production are the  $s$ -,  $t$ - and  $Wt$ - channels [55]. In the  $s$ -channel, an initial quark annihilates  
 190 with an anti-quark of different flavour, producing a virtual  $W$  boson which decays to a top quark and  
 191 anti-bottom quark. In the  $t$ -channel, an initial  $b$  quark interacts with a different flavour quark via the  
 192 exchange of a  $W$  boson. This interaction produces a top quark and another quark. In the  $Wt$ -channel,  
 193 an initial gluon interacts with a  $b$  quark to produce a top quark and a  $W$  boson, either via the absorption  
 194 of the gluon by the  $b$  quark or via the exchange of a top quark. In Table 2, single top production cross  
 195 sections in  $pp$  collisions at  $\sqrt{s} = 13$  TeV for the  $s$ -,  $t$ - and  $Wt$ -channels, are shown.

Channel	Process	Total Cross Section [pb]
$s$	$q\bar{q}' \rightarrow W \rightarrow \bar{b}t$	$10.32^{+0.40}_{-0.36}$
$t$	$bq' \rightarrow W \rightarrow tq$	$216.99^{+9.04}_{-7.71}$
$Wt$	$bg \rightarrow b/t \rightarrow Wt$	$71.7 \pm 3.85$

Table 2: Single top production cross sections in  $pp$  collisions at  $\sqrt{s} = 13$  TeV for the  $s$ -,  $t$ - and  $Wt$ - channels [35] are shown. The prime superscript on  $q'$  indicates that the quark has a different flavour to  $q$ .

196 Single top production is suppressed compared to pair produced top production, with  $t\bar{t}$  production (lepto-  
 197 nomic final state) being around three times as likely to occur than single top production across all decay  
 198 channels.

### 199 2.1.1.1 Motivation for the search for $tWZ$ production in the tetralepton channel

200 The recent lack of signs of new physics from LHC data [91] tells us that new physics is either very heavy,  
 201 or is very weakly coupled to SM particles. We therefore might only observe signs of new physics in  
 202 anomalous rates of well-chosen processes. The  $tWZ$  process is a prime example of such a process. It  
 203 has an extremely low production cross section of  $\approx 160$  fb for  $\sqrt{s} = 13$  TeV [25], and has subsequently  
 204 never been observed by any particle physics experiment. Since  $tWZ$  involves a charged  $W$  boson and  
 205 neutral  $Z$  boson, its cross section is sensitive to the charged and neutral couplings to the top quark. In  
 206 turn, the top quark is strongly coupled to the Higgs boson, due to the top quark's large mass. Due to  
 207 the large coupling of the top quark to the Higgs boson, corrections to the Higgs boson mass diverge in  
 208 the SM. The top quark's couplings are modified, in order to remove this divergence, in many scenarios  
 209 of new physics that aim to resolve the Hierarchy Problem. Since the  $Z$  boson may be radiated from the  
 210 initial-state  $b$ -quark, the final-state top quark, or the final-state  $Z$  boson, the  $tWZ$  process embeds the  
 211  $b - Z$ ,  $t - Z$  and  $W - Z$  electroweak couplings which are often modified in BSM physics. Therefore  $tWZ$   
 212 is an important process in the search for signs of new physics and BSM physics.

213  
 214 One such BSM theory which is sensitive to  $tWZ$  production [66, 73] is the Standard Model Effective Field  
 215 Theory (SMEFT) [27]. The SMEFT attempts to describe physics at large energy scales which we have  
 216 not yet been able to probe experimentally. The SMEFT inherits the same QFT framework as the SM,  
 217 and adds terms to the SM Lagrangian which describe the interactions of SM particles at higher energy  
 218 scales. Analogous to the coupling constants found in the SM Lagrangian, which indicate the interaction

strengths between different particles, SMEFT contains scalar coefficients which operate in the same way. These scalar coefficients are known as Wilson coefficients. It has been shown that the cross section of  $tWZ$  is sensitive to many Wilson coefficients. An experimental constraint on the cross section of  $tWZ$  is therefore expected to be impactful on a global fit on all the Wilson coefficients in SMEFT.

223

Prior to this analysis, only three experimental studies of  $tWZ$  in ATLAS have been performed. Two of the studies utilised the trilepton channel to search for  $tWZ$  production, whereas the third study utilised both the tri- and tetralepton channels. The first search utilised  $36 \text{ fb}^{-1}$  of ATLAS data and an upper limit on the cross section of  $tWZ$  was set at a value of  $\approx 6$  times the SM cross section [79]. The second search in the trilepton channel utilised  $139 \text{ fb}^{-1}$  of ATLAS data and an expected upper limit on the cross section of  $tWZ$  was set at a value of  $\approx 2.6$  times the SM cross section [99]. In Section 4.10.2, the aforesaid analysis will be used in combination with this analysis, in order to further increase the sensitivity of this analysis to the cross section of  $tWZ$ . The third study investigated the feasibility of a cross section measurement of  $tWZ$  production with CMS Run 3 data ( $300 \text{ fb}^{-1}$ ) [98], by utilising the tri- and tetralepton channels. The study showed that it is possible to exclude  $\mu(tWZ)$  at the  $7\sigma$  significance level using  $300 \text{ fb}^{-1}$  of data. This study needs to be further investigated, since its findings seem improbable given the results obtained in this thesis.

## 236 2.2 $tWZ$

### 237 2.2.1 Tetralepton Channel

In Figure 2, the Leading Order (LO) Feynman diagram for  $tWZ$  in the tetralepton channel, is shown.

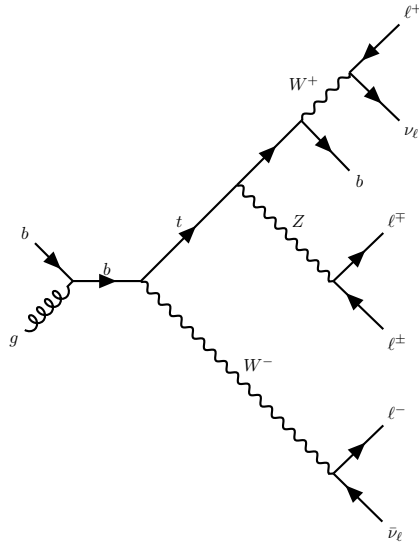
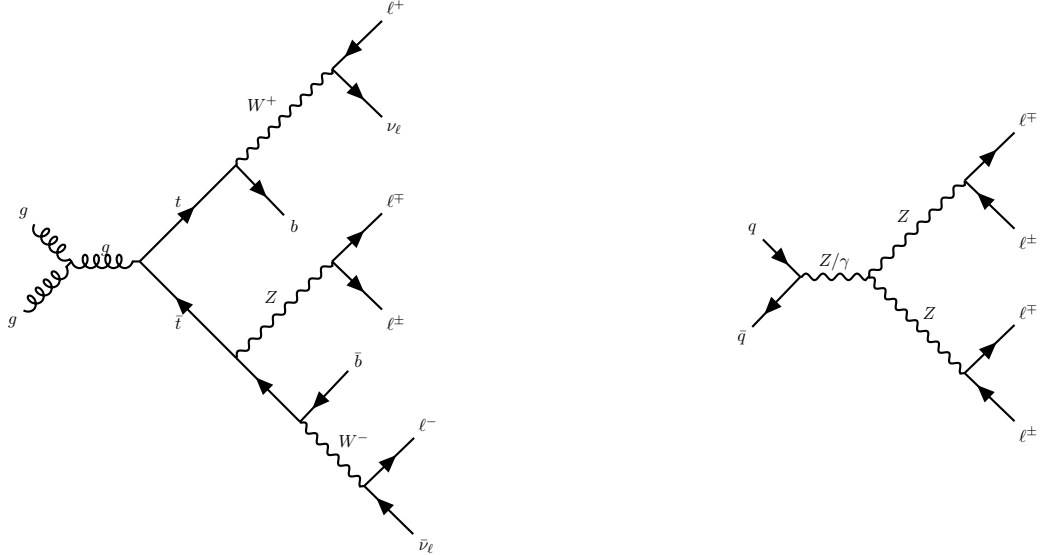


Figure 2: The LO Feynman diagram of  $tWZ$  production in the tetralepton channel is shown.

239 **2.2.1.1 Backgrounds**

240 The main backgrounds for  $tWZ$  (tetralepton channel) are the production of a two tops, both in the  $\ell\nu b$ <sup>1</sup>  
 241 final state channel, together with a  $Z$  boson ( $t\bar{t}Z$ ) and diboson production with fully leptonic final states  
 242 ( $ZZ$ ). In Figure 2.2.1.1, LO Feynman diagrams for  $t\bar{t}Z$  and  $ZZ$  in the tetralepton channel, are shown.



243

244

Figure 3: The LO Feynman diagrams for  $t\bar{t}Z$  (left) and  $ZZ$  (right) in the tetralepton channel are shown.

245 The  $t\bar{t}Z$  process contains fours leptons and two  $b$ -quarks in its final state ( $\sigma_{(t\bar{t}Z).Br(4\ell)}^{\text{NLO}} = 0.95 \pm 0.08_{\text{stat}} \pm$   
 246  $0.10_{\text{syst}} \text{ pb at } \sqrt{s} = 13 \text{ TeV}$  [2]) and can easily mimic the  $tWZ$  signal process, for instance, by one of its  
 247  $b$ -jets being undetected or mis-identified in the detector. The  $ZZ$  process contains four leptons and zero  
 248  $b$ -quarks in its final state ( $\sigma_{(ZZ).Br(4\ell)}^{\text{NNLO}} = 14.6^{+1.9}_{-1.8}(\text{stat})^{+0.5}_{-0.3}(\text{syst}) \pm 0.2(\text{theo}) \pm 0.4(\text{lumi}) \text{ pb at } \sqrt{s} = 13$   
 249  $\text{TeV}$  [63]). One way in which  $ZZ$  can mimic the  $tWZ$  signal process is by reconstruction of a non-prompt  
 250  $b$ -jet.

251 **2.2.2 Comparison to Trilepton Channel**

252 The most apparent difference between the tri and tetralepton channels is the number of events present,  
 253 with the tetralepton channel having far less events in its phase space than that of the tri-lepton channel.  
 254 The lack of statistics in the tetralepton channel can be attributed to its low cross section times branching  
 255 ratio of  $\sigma_{(tW^\pm Z).Br(4\ell)}^{\text{NLO}} = 0.7 \text{ fb}$  [25]. The tri-lepton channel has a cross section times branching ratio of  
 256  $\sigma_{(tW^\pm Z).Br(3\ell)}^{\text{NLO}} = 3.9 \text{ fb}$  [25], which is around a factor of four larger than that of the tetralepton channel.  
 257 This difference between the production cross section of the two decay channels can be largely attributed  
 258 to the difference in branching ratios ( $\frac{\Gamma_i}{\Gamma}$ ) between a hadronically decaying  $W$  boson,  $\frac{\Gamma_{W \rightarrow \text{had}}}{\Gamma_W} = (67.41 \pm$   
 259  $0.27)\%$  [55], present in the tri-lepton channel and a leptonically decaying  $W$  boson,  $\frac{\Gamma_{W \rightarrow \ell\nu}}{\Gamma_W} = (10.86 \pm$   
 260  $0.09)\%$  [55], present in the tetralepton channel. Despite the tetralepton channel's low statistics, it is not  
 261 subject to the large  $WZ$  background present in the trilepton channel [99]. The tetralepton channel has

<sup>1</sup>In this thesis,  $\ell$  refers to an electron or muon,  $\nu$  refers to a neutrino or anti-neutrino and  $b$  refers to a bottom quark or anti-bottom quark

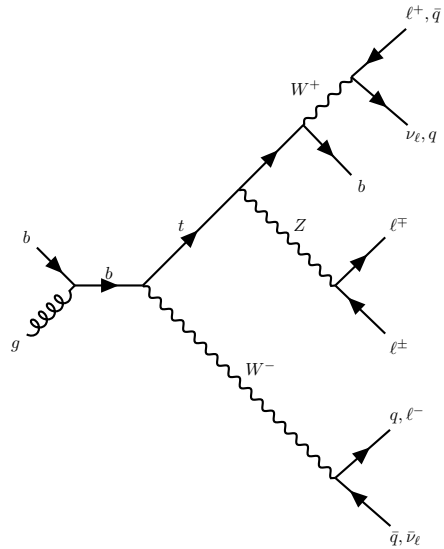


Figure 4: The LO Feynman diagram of  $tWZ$  production in the tri-lepton channel.

262 a substantial amount of  $ZZ$  background (not present in the trilepton channel), fortunately this can be  
263 easily suppressed due to the full reconstructability of the two leptonically decaying  $Z$ -bosons.

264

# Chapter 3

## 265 The ATLAS Experiment and Detector

### 266 3.1 The ATLAS Experiment

267 The ATLAS (A Toroidal LHC ApparatuS) detector is one of two general purpose detectors at CERN  
 268 (the European Organization for Nuclear Research) near Geneva in Switzerland. These detectors collect  
 269 data from the collisions provided by the worlds highest energy particle accelerator [29], the Large Hadron  
 270 Collider (LHC) situated at CERN.

271

272 In this section, information about the LHC and the ATLAS detector are given. This includes technical  
 273 aspects of the ATLAS detector and the processing of data into meaningful physics objects<sup>1</sup> to be used  
 274 in analyses. The following chapter consists of information from "The LHC Design Report" [29], "LHC  
 275 Machine" [48] and "The ATLAS Experiment at the CERN Large Hadron Collider" [41] unless otherwise  
 276 stated.

#### 277 3.1.1 Large Hadron Collider (LHC)

278 The LHC is a circular 27 km particle accelerator located in an underground tunnel on the border between  
 279 France and Switzerland. The accelerator consists of supercooled, superconducting magnets which  
 280 accelerate and collide beams of protons at centre-of-mass energies up to  $\sqrt{s} = 13$  TeV at instantaneous  
 281 luminosities of  $\mathcal{L} \sim 10^{34}$  cm $^{-2}$ s $^{-1}$ . In the LHC,  $pp$  beams consist of bunches of protons which collide  
 282 every 25 ns, corresponding to a frequency of 40 MHz. Several accelerator systems are used to accelerate  
 283 protons and heavy ions to such high energies. Protons are extracted from a tank of ionised hydrogen gas  
 284 and are injected into the Linear Accelerator 2 (LINAC), where they are linearly accelerated to momenta  
 285 of 50 MeV. The proton bunches are then sequentially accelerated by a chain of circular accelerators. The  
 286 chain starts with the Booster which accelerates the protons to momenta of up to 1.4 GeV. The proton  
 287 bunches are then fed through to the Proton Synchrotron (PS) and the Super Proton Synchrotron (SPS)  
 288 which accelerate the protons to momenta of up to 25 GeV and 450 GeV respectively. The protons are  
 289 then transferred to two beam pipes of the LHC where they travel in opposite directions. Both proton  
 290 beams are accelerated to their final momenta of 6.5 TeV, resulting in a centre-of-mass energy of 13 TeV.  
 291 These proton beams then collide at one of the four main interaction points (positions along the beam

---

<sup>1</sup>a detector signal (or a combination of detector signals) that represent a candidate for a particle (e.g leptons and jets)

292 pipe where collisions occur) situated along the LHC.

293

294 The four main experiments located at the interaction points are ATLAS, the Compact Muon Solenoid  
 295 (CMS), Large Hadron Collider Beauty (LHCb) Experiment and A Large Ion Collider Experiment (AL-  
 296 ICE). The ATLAS and CMS detectors are general-purpose detectors which investigate a wide range of  
 297 physics processes. Since both ATLAS and CMS can measure the same processes, they are able to cross-  
 298 check and validate measurements taken by one another. The LHCb detector is specifically designed to  
 299 study decays of particles containing  $b$ -quarks. The ALICE detector is designed to study the strongly  
 300 interacting quark-gluon plasma which is formed at extremely high energy densities. At the interaction  
 301 points, the two proton beams which consist of protons in closely packed bunches, travel in opposite direc-  
 302 tions to one another and collide. Many hard  $pp$  collisions (events) can occur per bunch crossing, however  
 303 it is the most energetic collision in the bunch crossing that is interesting for discovery potential. The  
 304 most energetic collision is therefore chosen to be studied and any additional collisions are aimed to be  
 305 rejected. These additional collisions are referred to as *pile-up*. Pileup complicates the reconstruction of  
 306 the particles originating from the hard collision of interest.

### 307 3.1.1.1 Luminosity

308 This section consists of information from "Modern Particle Physics" [92], unless otherwise stated. The  
 309 event production rate at the LHC,  $R(t)$ , for a certain process of interest is given by,

$$R(t) = \mathcal{L}(t)\sigma \quad (3.1)$$

310 where  $\mathcal{L}(t)$  is the instantaneous luminosity and  $\sigma$  and is the cross section of the process of interest. The  
 311 instantaneous luminosity,  $\mathcal{L}(t)$ , is independent on the process of interest, and depends on various collider  
 312 and beam parameters.  $\mathcal{L}(t)$  can be written in terms of these parameters as,

$$\mathcal{L}(t) = f \frac{N n_1 n_2}{4\pi \sigma_x \sigma_y} \quad (3.2)$$

313 where  $f$  is the beam revolution frequency,  $N$  is the number of proton bunches colliding per second,  $n_1$   
 314 and  $n_2$  are the number of protons in the colliding bunches,  $\sigma_x$  and  $\sigma_y$  are the beam spread in the  $x$  and  $y$   
 315 directions respectively. The average number of visible (particles that are measurable by the detector)  $pp$   
 316 interactions per bunch crossing,  $\langle \mu \rangle$ , can be written as,

$$\langle \mu \rangle = \frac{\sigma_{inel} \mathcal{L}}{N f} \quad (3.3)$$

317 where  $\sigma_{inel}$  is the inelastic  $pp$  interaction cross section. The total integrated luminosity,  $L$ , across some  
 318 time interval, is given by,

$$L = \int \mathcal{L} dt. \quad (3.4)$$

319 The units of  $L$  are inverse area, and are given by  $\text{fb}^{-1}$  at the LHC and the ATLAS detector. In Figure 5,  
 320 the total integrated luminosity vs time, recorded by ATLAS for  $\sqrt{s} = 13$  TeV  $pp$  collisions at the LHC is  
 321 shown [94].

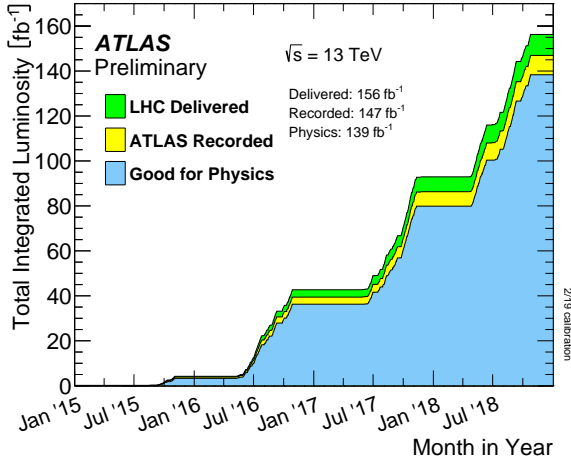


Figure 5: The total integrated luminosity vs time, recorded by ATLAS for  $\sqrt{s} = 13$  TeV  $pp$  collisions at the LHC is shown [94]. The total integrated luminosity delivered by the LHC, recorded by ATLAS and certified to be good quality data are shown by the green, yellow and blue histograms respectively. The month and year of data taking is shown on the x-axis and the total integrated luminosity (in  $\text{fb}^{-1}$ ) is shown on the y-axis.

322 A total integrated luminosity of  $139 \text{ fb}^{-1}$  of data certified as good for physics was recorded by ATLAS  
 323 between 2015 and 2018. This data taking period is referred to as Run 2. It occurred after the Run 1 data  
 324 taking period (2011 and 2012) and the Long Shutdown 1 LHC upgrade period (2013 and 2014). In this  
 325 analysis, we use the Full Run 2 dataset.

### 326 3.2 The ATLAS Detector

327 In Figure 6, the schematic of the ATLAS detector, is shown.

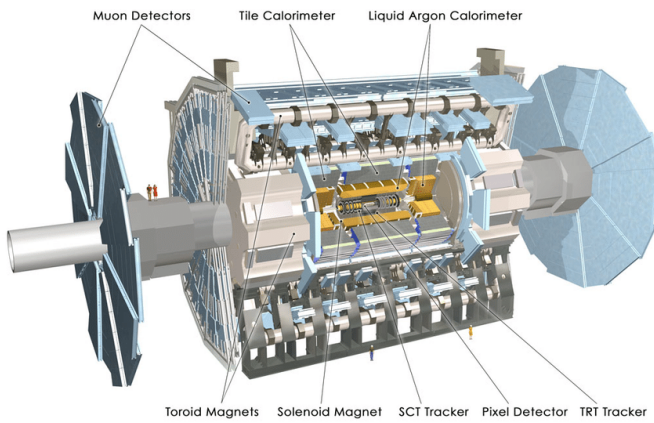


Figure 6: A schematic of the ATLAS detector is shown. [41]

328 The detector is cylindrically shaped which covers close to  $4\pi$  in solid angle. It has a length of 44 m,  
 329 a diameter of 25 m and a mass of 7000 tons. The ATLAS detector consists of four main sub-detectors  
 330 arranged in concentric cylindrical layers around the beam pipe. These include the inner detector, the  
 331 electromagnetic calorimeter, the hadronic calorimeters and the muon spectrometer. The sub-detectors

332 record the momenta, energies and trajectories of different particles produced in the collider, allowing for  
 333 the reconstruction and identification of these particles to be used in physics analyses.

### 334 3.2.1 Coordinate System and Kinematics

335 The ATLAS detector adopts a right-handed coordinate system. The origin is at the nominal interaction  
 336 point with the  $z$ -axis defined to be counter-clockwise along the beam line. The  $x - y$  plane (or transverse  
 337 plane) is perpendicular to the beam line, with the  $x$ -axis pointing towards the centre of the LHC ring and  
 338 the  $y$ -axis pointing upwards towards the Earth's surface. The azimuthal angle,  $\phi \in [-\pi, \pi]$ , is measured  
 339 in the transverse plane with respect to the positive  $x$ -axis. The polar angle,  $\theta \in [0, \pi]$ , is measured in  
 340 the  $z - y$  plane with respect to the positive  $y$ -axis. A quantity called the pseudorapidity,  $\eta \in [0, \infty]$  is  
 341 defined as,

$$\eta = -\ln \tan\left(\frac{\theta}{2}\right) \quad (3.5)$$

342 The polar angle,  $\eta$ , is often used instead of  $\theta$ , since the difference in  $\eta$  between two particles,  $\Delta\eta$ , is  
 343 invariant under a Lorentz boost in the  $z$ -direction [95]. The angular distance between two physics  
 344 objects,  $\Delta R$ , can be written as,

$$\Delta R = \sqrt{(\Delta\phi)^2 + (\Delta\eta)^2} \quad (3.6)$$

345 where  $\Delta\phi$  is the difference in  $\phi$  between the two physics objects of interest. Quantities defined in the  
 346 transverse plane are often used to describe the kinematics of physics objects in hadron collider experiments.  
 347 The transverse momentum,  $p_T$ , is defined as,

$$p_T = \sqrt{(p_x)^2 + (p_y)^2} \quad (3.7)$$

348 where  $p_x$  and  $p_y$  are the  $x$  and  $y$  components of the physics object's momenta, respectively. The transverse  
 349 energy,  $E_T$ , is defined as,

$$E_T = \sqrt{m^2 + p_T^2} \quad (3.8)$$

350 where  $m$  is the invariant mass of the physics object.

### 351 3.2.2 Inner Detector

352 The inner detector is the first layer of concentric cylindrical sub-detector layers in the ATLAS detector.  
 353 It is used to identify charged particles and reconstruct the trajectories of charged particles produced in  
 354 the collisions via energy deposition in semiconductor material (hits) and the ionisation of gas. It consists  
 355 of three complementary sub-detectors (in order from nearest to farthest from the beam pipe): the Pixel  
 356 Detector, the Semiconductor Tracker (SCT) and the Transition Radiation Detector (TRT). The Pixel  
 357 Detector and SCT are based on semiconductor technology and have the highest granularity of any sub-  
 358 detector in ATLAS, in order to cope with the high frequency of collisions near the interaction point. The  
 359 TRT consists of drift tubes (straws) containing a gas mixture, which allows measurement of the energy  
 360 deposited by charged particles through the ionisation of the gas. Solenoid magnets surround the inner

361 detector and bend the trajectories of charged particles. The charges and transverse momenta of particles  
362 can be inferred from their bent trajectories, which are reconstructed by the hits produced via energy  
363 deposition in the Inner Detector.

### 364 **3.2.3 Electromagnetic and Hadronic Calorimeters**

365 The Electromagnetic Calorimeter (ECAL) and Hadronic Calorimeter (HCAL) surround the Inner Detec-  
366 tor, with the ECAL nearer to the beam line. The ECAL and HCAL provide accurate measurements of  
367 the energy of particles which interact electromagnetically (e.g. photons and electrons) and hadronically  
368 (e.g. jets), respectively. Particles entering the calorimeters interact with the detector material and create  
369 either a electromagnetic shower (in the ECAL) or a hadronic shower (in the HCAL), depositing all their  
370 energy in the calorimeter cells. The primary mechanism of energy deposition in the ECAL is through  
371 bremsstrahlung (for electrons) and pair production (photons). Hadrons usually deposit a small amount  
372 of their energy in the ECAL, and interact via inelastic scattering with the nuclei of the detector material.  
373 The hadronic showers (jets) produced in these nuclear interactions travel much further than an electro-  
374 magnetic shower, and for that reason, the volume of the HCAL is designed to occupy a much larger space  
375 than that of the ECAL.

### 376 **3.2.4 Muon Spectrometer**

377 The Muon Spectrometer (MS) is the outermost sub-detector of ATLAS and surrounds the HCAL. Muons  
378 traverse through the inner detector and calorimeters, with minimal energy loss, before reaching the MS.  
379 The MS consists of trigger and high-precision tracking systems. Large superconducting toroid shaped  
380 magnets deflect the incoming muons to measure their trajectories and subsequently their momenta via  
381 the curvature of the trajectories. The MS measures muon trajectories as they ionize gas (filled with Ar  
382 and CO<sub>2</sub> gas) in the MS drift chambers.

### 383 **3.2.5 Trigger and Data Acquisition System**

384 The Trigger and Data Acquisition System (TDAQ) manages and handles the large amount of data pro-  
385 duced within the ATLAS detector. In Run 2,  $pp$  bunch crossings occur every 25 ns, corresponding to  
386 an event rate of 40 MHz. The TDAQ system performs a fast preliminary reconstruction to select events  
387 with signatures which are interesting for physics analyses. The information collected from these events  
388 are permanently stored for offline reconstruction and analysis, and the rest (the vast majority of events)  
389 are discarded. The trigger system reduces the 40 MHz data rate to around 1 kHz.

### 390 **3.2.6 Particle Identification and Object Reconstruction**

391 Particles originating from  $pp$  collisions, or from their subsequent decays, traverse through the ATLAS  
392 detector and interact with its different sub-detectors, producing characteristic electronic signals. These  
393 signals are then processed by various algorithms to reconstruct and identify the physics objects (e.g.  
394 electrons, muons, jets) in the event. This section outlines the procedures used to define these physics  
395 objects.

---

**396 3.2.6.1 Tracks and primary vertices**

397 The trajectories of charged particles, or tracks, are reconstructed in the ID. First, energy is deposited by  
 398 charged particles (hits) in pixels or strips, in the Pixel and SCT detectors respectively. Adjacent pixels  
 399 or strips are grouped together in *energy clusters*. Energy clusters define 3D space-points indicating the  
 400 location where the charged particle traversed. Track seeds are then defined as sets of three space-points,  
 401 in either the Pixel or SCT detectors. A Kalman filter [11] is then used to build track candidates from the  
 402 track seeds. Often, multiple track candidates are built per track seed, therefore an ambiguity solver [38]  
 403 is needed for finding the track which best represents the traversal of the charged particle. The ambiguity  
 404 solver ranks each track from a given seed based on, the number of associated hits, the number of holes  
 405 (expected hits which are absent), track momenta and the  $\chi^2$  of the track fit. Low ranked tracks are then  
 406 discarded. High ranked tracks are refitted, introducing information from the TRT.

407  
 408 The primary vertex is the location of the  $pp$  collision of interest (i.e. from the hard scatter). The primary  
 409 vertex from the hard scatter needs to be identified, to isolate the event of interest from unwanted pile-  
 410 up events. In the event reconstruction procedure [72], the primary vertex is defined as the vertex of  
 411 the event with the largest sum of  $(p_T)^2$  (corresponding to the measured  $(p_T)^2$  of the particle from its  
 412 reconstructed track) of its associated tracks. Furthermore, the primary vertex is required to have at least  
 413 two associated tracks. To reduce contamination from fake tracks used in primary vertex reconstruction,  
 414 only tracks which pass certain tight selection criteria are used in the reconstruction procedure. An iterative  
 415 fitting procedure is then used to reconstruct the primary vertex by finding a set of reconstructed tracks  
 416 which have a common vertex.

**417 3.2.6.2 Electrons**

418 Since electrons are charged particles, they give rise to tracks in the Inner Detector. They also deposit  
 419 energy in the ECAL via electromagnetic showering. Electrons are therefore reconstructed and identified  
 420 from signals in the Inner Detector and ECAL. Electrons are reconstructed using a dynamic clustering  
 421 algorithm [1] which matches electron candidate tracks in the Inner Detector to energy clusters in the  
 422 ECAL. The dynamic clustering algorithm matches tracks to energy clusters which have local maxima, to  
 423 form electron candidates. A likelihood discriminant is used to identify electrons. Quantities measured  
 424 in the Inner Detector and ECAL are used as input, such that they discriminate well between prompt  
 425 isolated electrons and other physics objects (e.g. jets, electron from a photon conversion, electron from a  
 426 semi-leptonically decaying hadron). Important input variables include the shape of the electromagnetic  
 427 shower, track quality in the Inner Detector and information from the TRT.

**428 3.2.6.3 Muons**

429 Muons leave tracks in the Inner Detector and the MS. They traverse the ECAL and HCAL with no  
 430 significant energy loss. Muons are therefore reconstructed and identified from information in the Inner  
 431 Detector and MS. Tracks are reconstructed [5] in the Inner Detector and MS independently. Both tracks  
 432 are combined, using a global  $\chi^2$  fit, resulting in reconstructed muon candidates. Similar to electron  
 433 identification, muons use a likelihood discriminant to identify prompt muons and suppress background

<sup>434</sup> contamination (mainly from pion and kaon decays).

### <sup>435</sup> 3.2.6.4 Jets and $b$ -tagging

<sup>436</sup> Coloured particles emerging from the interaction point result in collimated streams of colourless particles,  
<sup>437</sup> known as jets. Jets can deposit energy in the Inner Detector and in the HCAL. Jets in ATLAS are  
<sup>438</sup> reconstructed from topological clusters using the anti- $k_t$  algorithm [31]. Topological clusters are groups  
<sup>439</sup> of adjacent calorimeter cells which contain energy deposition above the average amount of noise expected  
<sup>440</sup> in the cell. Adjacent cells are grouped together under certain criteria to form topological clusters which  
<sup>441</sup> form jets.

<sup>442</sup>

<sup>443</sup> Different tagging algorithms are used to identify the quark flavour which initiated a jet. Tagging of  $b$ -  
<sup>444</sup> quarks is used extensively in top physics, due to the  $b$ -quark present in the top quark's dominant decay  
<sup>445</sup> channel (See Table 1). Hadrons arising from  $b$ -quark hadronisation have mean lifetimes  $\sim 1.5$  ps and  
<sup>446</sup> travel (on average) a few millimetres before decaying. This creates a secondary vertex within the jet  
<sup>447</sup> (See Figure 7). This characteristic decay signature, along with several other unique features of  $b$ -jets,  
<sup>448</sup> are exploited in  $b$ -tagging algorithms to distinguish  $b$ -jets from  $c$ - or light flavour jets. In Figure 7, an  
<sup>449</sup> illustration of the production of a  $b$ -jet, is shown.

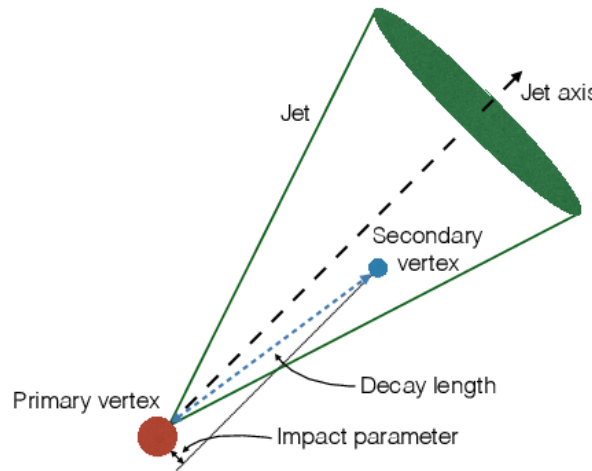


Figure 7: An illustration [42] of the production of a  $b$ -jet is shown. The jet is represented by the cone and axis of the jet is represented by the dotted black line drawn at a right angle to the circular base of the cone. The primary vertex is represented by the red circle and the secondary vertex is represented by the blue circle. The dotted blue line represents the path travelled by the hadron before decaying at its secondary vertex. The impact parameter is shown by a black line drawn from the secondary vertex.

<sup>450</sup> This illustrates the presence of a secondary vertex within a  $b$ -jet. In this analysis, we use the recommended  
<sup>451</sup> DL1r (Deep-Learning Flavour Tagger) tagging algorithm [17]. The DL1r algorithm combines outputs from  
<sup>452</sup> several low-level tagging algorithms using a Deep Neural Network and outputs the probability that a given  
<sup>453</sup> input jet is identified as a  $b$ ,  $c$  or light flavoured jet.

454

# Chapter 4

## The search for $tWZ$ production using events with four leptons

457 In this chapter, the full analysis procedure is presented for  $tWZ$  production in the tetralepton channel  
458 based on an integrated luminosity of  $139 \text{ fb}^{-1}$  of data recorded by ATLAS. This includes a description  
459 of the data and simulation, definitions of physics objects, event selection and the subsequent definition of  
460 signal and control regions used in this analysis. Furthermore, estimation of the fake lepton component  
461 using the MC template method is described. A kinematic reconstruction algorithm and various Machine  
462 Learning techniques, used to discriminate between signal and background events, are described. An  
463 outline of the systematic uncertainties affecting the measurement are presented. Finally, the results of  
464 the analysis and a study of the analysis projected to higher luminosities is presented.

### 465 4.1 Data and Monte Carlo Simulation

#### 466 4.1.1 Data Samples

467 The  $pp$  collision data used in this analysis was collected with the ATLAS detector at the LHC from 2015  
468 to 2018. This data period of data taking is referred to as Run 2. During this period,  $pp$  collisions at  
469  $\sqrt{s} = 13 \text{ TeV}$ , corresponding to an integrated luminosity of  $156 \text{ fb}^{-1}$ , were delivered by the LHC. The  
470 ATLAS detector recorded  $147 \text{ fb}^{-1}$  of this total delivered data.  $139 \text{ fb}^{-1}$  of the data recorded by ATLAS  
471 is considered to be good enough for physics analyses (the data passes certain quality control criteria)  
472 and placed into the *Good Runs List* [53]. Specific time-intervals where the luminosity is assumed to be  
473 constant are known as *lumi-blocks*. Only events from lumi-blocks in which LHC beams were stable and all  
474 ATLAS detectors were operational are selected. The list of suitable run and lumi-blocks is summarised  
475 in the official Good Runs Lists for 2015-2018 data, as specified in Ref. [53]. The integrated luminosities  
476 corresponding to the individual datasets for years 2015, 2016, 2017 and 2018 are  $3.2 \text{ fb}^{-1}$ ,  $33.0 \text{ fb}^{-1}$ ,  $44.3$   
477  $\text{fb}^{-1}$  and  $58.5 \text{ fb}^{-1}$  respectively.

478 **4.1.2 Monte Carlo Samples**

479 Simulated Monte Carlo (MC) samples were generated and used to model the SM  $tWZ$  signal and its  
480 backgrounds. The following background processes are considered:

481 •  **$t\bar{t}Z$ :**  $t\bar{t}$  with an associated  $Z$ -boson, in the tetralepton final state. Therefore, both top quarks  
482 decay leptonically (e.g.  $t \rightarrow W^+ b \rightarrow \ell^+ \nu b$ ) and of these top quarks emits a  $Z$ -boson which decays  
483 leptonically ( $Z \rightarrow \ell^\pm \ell^\mp$  (OSSF lepton pair) ). This results in a final state with 4 leptons and 2  
484 b-quarks.

485 •  **$ZZ$ :** Diboson production with a tetralepton final state, therefore both  $Z$ -bosons decay leptonically  
486 ( $Z \rightarrow \ell^\pm \ell^\mp$  (OSSF lepton pair) ).

487 • **other:** Processes with a relatively minimal, but non-negligible background contribution

488 -  $VVV(V = W/Z)$

489 -  $t\bar{t}$

490 -  $t\bar{t}W$

491 -  $t\bar{t}WW$

492 -  $t\bar{t}H$

493 -  $WZ$

494 -  $t\bar{t}t$

495 -  $t\bar{t}t\bar{t}$

496 -  $tZq$

497 The MC simulations are achieved via the use of event generators and parton shower generators. The  
498 parton shower generators simulate any incoming or outgoing particles from the hard process, which carry  
499 QCD color charge and can therefore lead to parton showers. The production of  $tWZ$  events is simulated  
500 with the **MADGRAPH5\_AMC@NLO 2.3.3** [9] generator providing matrix element (ME) calculations at NLO  
501 (next-to-leading order) in QCD. The events are interfaced with **PYTHIA 8.235** for the parton shower. The  
502 production of  $t\bar{t}Z$  and  $t\bar{t}W$  events are simulated with the **MADGRAPH5\_AMC@NLO 2.3.3** generator providing  
503 ME calculations at NLO in QCD. The events are interfaced with **PYTHIA 8.210** [90] for the parton  
504 shower. Event generation of  $tWZ$  and  $t\bar{t}Z$  results in diagrams which overlap with one another, that is,  
505 these diagrams contain the same initial and final state particles. Several methods exist in order to separate  
506 between the two processes, by removing the overlap, therefore avoiding double counting. There are two  
507 different diagram removal procedures, diagram removal procedure 1 (DR1) [44] and diagram removal  
508 procedure 2 (DR2). The DR1 scheme is used to remove the overlap between  $tWZ$  and  $t\bar{t}Z$ . A comparison  
509 to the DR2 scheme is used to estimate part of the theoretical systematic on the modelling of the  $tWZ$   
510 signal (See Section 4.8.2). Diboson processes which feature the three charged leptons and one neutrino  
511 or four charged lepton in their final states, such as  $WZ$  and  $ZZ$ , are simulated using **SHERPA 2.2.2** [26]  
512 at NLO in QCD precision. The events are interfaced with **SHERPA** for the parton shower. Triboson  
513 processes such as  $WWW$ ,  $WWZ$ ,  $WZZ$ , and  $ZZZ$  containing up to six leptons in their final states are

514 simulated using **SHERPA 2.2.2** at NLO in QCD precision. The events are interfaced with **SHERPA** for the  
 515 parton shower. The production of  $t\bar{t}$  events are simulated with the **POWHEG** [51] generator providing ME  
 516 calculations at NLO in QCD. The events are interfaced with **PYTHIA 8.210** for the parton shower. The  
 517 production of  $t\bar{t}t$ ,  $t\bar{t}\bar{t}$  and  $t\bar{t}WW$  are simulated using the **MADGRAPH5\_AMC@NLO 2.2.2** generator at LO in  
 518 QCD precision. The events are interfaced with **PYTHIA 8.186** [89] for the parton shower. The production  
 519 of  $t\bar{t}$  with an associated Higgs boson,  $t\bar{t}H$ , are generated using the **MADGRAPH5\_AMC@NLO 2.6.0** generator  
 520 at NLO in QCD precision. The events are showered using **PYTHIA 8.230** [90]. The production of  $t\bar{t}$   
 521 events are simulated with the **POWHEG** generator providing ME calculations at NLO in QCD. The events  
 522 are showered using **PYTHIA 8.230**. The production of a single top quark in association with a  $Z$ -boson  
 523 and an extra parton,  $tZq$ , is simulated using **MADGRAPH5\_AMC@NLO 2.3.3** at NLO in QCD precision. The  
 524 events are interfaced with **PYTHIA 8.230** for the parton shower. In Table 3, the event generator and  
 525 parton shower used for each process's sample are shown.

Process	Event Generator	Cross section calculation	Parton Shower
$tWZ$	<b>MADGRAPH5_AMC@NLO 2.3.3</b>	NLO	<b>PYTHIA 8.235</b>
$t\bar{t}Z$	<b>MADGRAPH5_AMC@NLO 2.3.3</b>	NLO	<b>PYTHIA 8.210</b>
$ZZ, WZ$	<b>SHERPA 2.2.2</b>	NLO	<b>SHERPA</b>
$VVV(V = W/Z)$	<b>SHERPA 2.2.2</b>	NLO	<b>SHERPA</b>
$t\bar{t}$	<b>POWHEG</b>	NLO	<b>PYTHIA 8.230</b>
$t\bar{t}W$	<b>MADGRAPH5_AMC@NLO 2.3.3</b>	NLO	<b>PYTHIA 8.210</b>
$t\bar{t}WW$	<b>MADGRAPH5_AMC@NLO 2.2.2</b>	LO	<b>PYTHIA 8.186</b>
$t\bar{t}H$	<b>MADGRAPH5_AMC@NLO 2.6.0</b>	NLO	<b>PYTHIA 8.230</b>
$t\bar{t}t, t\bar{t}\bar{t}$	<b>MADGRAPH5_AMC@NLO 2.2.2</b>	LO	<b>PYTHIA 8.186</b>
$tZq$	<b>MADGRAPH5_AMC@NLO 2.3.3</b>	NLO	<b>PYTHIA 8.230</b>

Table 3: The event generator and parton shower used for the signal and background process's MC samples is shown.

#### 526 4.1.3 Trigger Strategy

527 Events in data and simulation are selected via either single lepton or dilepton (electron or muon) triggers.  
 528 To selected events, a logical **OR** between the triggers is applied. This means that events have to be  
 529 selected by at least one of the single or dilepton triggers. Electrons and muons may be surrounded by  
 530 other particles which could lead to problems in the reconstruction and identification process. They are  
 531 therefore required to be sufficiently isolated from other particles. This is done by defining an isolation  
 532 variable which ensures that the summed energies of the particles in a cone defined around the muon, with  
 533 radius  $\Delta R$ , are small. The isolation variable for a cone of radius  $x$ ,  $I_{\Delta R=x}$ , is given by,

$$I_{\Delta R=x} = \frac{\sum_i E_i}{p_T^{e/m}} \quad (4.1)$$

534 where  $E_i$  is the energy of the  $i^{\text{th}}$  particle within the cone and  $p_T^{e/m}$  is the  $p_T$  of the electron or muon.  
 535 In order to identify an electron or muon, various properties and detector signals related to them are fed  
 536 into different Machine Learning classifiers to determine the likelihood of the particle being an electron  
 537 or a muon. Cuts are applied to the output of the classifiers to define working points which correspond

to different selection efficiencies. The names commonly given to different working points, in order of decreasing efficiency, are very loose, loose, medium and tight. The single-muon trigger used to select muons in 2015 data and simulation requires a muon with  $p_T > 20$  GeV, an identification criteria corresponding to a loose working point and  $I_{\Delta R=0.2} < 0.12$ . Two single-muon triggers are used to select muons in 2016-2018 data and simulation. The first requires a muon with  $p_T > 26$  GeV, an identification criteria corresponding to a medium working point and  $I_{\Delta R=0.3} < 0.06$ . The second requires a muon with  $p_T > 50$  GeV. Two single-electron triggers are used to select electrons in 2015 data and simulation. The first requires an electron with  $p_T > 24$  GeV and an identification criteria corresponding to a medium working point. The second requires an electron with  $p_T > 120$  GeV and an identification criteria corresponding to a loose working point. Three single leptons triggers are used to select electrons in 2016-2018 data and simulation. The first requires an electron with  $p_T > 26$  GeV, an identification criteria corresponding to a tight working point and  $I_{\Delta R=0.2} < 0.1$ . The second requires an electron with  $p_T > 60$  GeV and an identification criteria corresponding to a medium working point. The third requires an electron with  $p_T > 140$  GeV and an identification criteria corresponding to a loose working point. The di-muon trigger used to select muons in 2015 data and simulation requires that one muon have  $p_T > 18$  GeV and another muon to have  $p_T > 8$  GeV. The di-muon trigger used to select muons in 2016-2018 data and simulation requires that one muon have  $p_T > 22$  GeV and another muon to have  $p_T > 8$  GeV. The di-electron trigger used to select electrons in 2015 data and simulation requires two electrons, each with  $p_T > 12$  GeV, and identification criteria corresponding to loose working points. The di-electron trigger used to select electrons in 2016-2018 data and simulation requires two electrons, each with  $p_T > 17$  GeV, and identification criteria corresponding to very loose working points. A final electron-muon trigger is used to select electrons and muons in 2016-2018 data and simulation that requires an electron with  $p_T > 17$  GeV and a muon with  $p_T > 14$  GeV, and identification criteria corresponding to loose working points. In Table 4, a summary of the triggers used to select muons and electrons in data and simulation are shown.

Trigger	Selection [GeV]	Working Point
Single-muon*	$p_T > 20$	loose
Single-muon	$p_T > 26$	medium
Single-muon	$p_T > 50$	-
Single-electron*	$p_T > 24$	medium
Single-electron*	$p_T > 120$	loose
Single-electron	$p_T > 26$	loose
Single-electron	$p_T > 60$	medium
Single-electron	$p_T > 140$	loose
Di-muon*	$p_T > 18, p_T > 8$	-
Di-muon	$p_T > 18, p_T > 8$	-
Di-electron*	$p_T > 12$	loose
Di-electron*	$p_T > 12$	loose
Di-electron	$p_T > 17$	very loose
Electron-Muon	electron $p_T > 17$ , muon $p_T > 14$	loose

Table 4: Single lepton and dilepton (electron and muon) triggers used to select events in data and simulation. Triggers labelled with \* are only used for 2015 data and simulation.

## 562 4.2 Physics objects

563 In this section the physics objects (leptons, jets and  $b$ -tagged jets) used in this analysis are outlined.

### 564 4.2.1 Leptons

565 In this analysis only  $e$  and  $\mu$  leptons are considered, since  $\tau$  leptons are difficult to detect in the AT-  
 566 LAS detector. They are challenging to detect since they have an extremely short lifetime ( $290.3 \pm 0.5$   
 567 fs [55]) which causes them to decay before reaching any detector components and therefore can only be  
 568 reconstructed via their decay products. In addition to our selection criteria of exactly four leptons, it is  
 569 required that the Leading (L), Next-to-Leading (NL), Next-to-Next-to-Leading (NNL) and Next-to-Next-  
 570 to-Next-to-Leading (NNNL) leptons have  $p_T$  greater than 28, 18, 10 and 10 GeV respectively. Relativity  
 571 loose object-level cuts are chosen in an attempt to maximize our signal statistics, since the analysis is  
 572 heavily statistically limited. Reconstructed electrons are required to be within  $|\eta| < 2.47$  and excluding  
 573 the transition region between the barrel and end-cap calorimeters at  $1.37 < |\eta| < 1.52$ . Reconstructed  
 574 muons are required to be within  $|\eta| < 2.5$ . The transverse impact parameter,  $d_0$ , is defined as the minimal  
 575 spacial distance between the object's (referring to leptons) trajectory and the primary vertex (the vertex  
 576 associated with the  $pp$  hard scatter). The longitudinal impact parameter,  $z_0$ , is defined as the value of  
 577  $z$  of the point on the object's trajectory which determines  $d_0$ . To ensure consistency between the lepton  
 578 and the primary vertex, it is required that  $|\frac{d_0}{\sigma(d_0)}| < 5$ ,  $|z_0 \sin \theta| < 0.5$  mm for electrons and  $|\frac{d_0}{\sigma(d_0)}| < 3$ ,  
 579  $|z_0 \sin \theta| < 0.5$  mm for muons, following the current recommendations [93]. To avoid instances where one  
 580 detector signal can result in multiple different reconstructed objects, an overlap removal procedure is ap-  
 581 plied which ignores all but one of these objects (See Section 4.2.4). Electrons are selected using a likelihood  
 582 based discriminant [1] which takes measurements from the tracking system, calorimeter system and quan-  
 583 tities derived from both the tracking and calorimeter system as input. Muons are selected using the Muon  
 584 Selection Tool [78]. Loose electrons are defined with the criteria above, using the `LooseAndBLayerLH`  
 585 ( $\sim 91\%$  selection efficiency for electrons with  $E_T > 30$  GeV [45]) identification algorithm (which has a  
 586 certain cut applied). Similarly, tight electrons are defined with the criteria above, using the `TightLH` ( $\sim$   
 587 80% selection efficiency for electrons with  $E_T > 30$  GeV [45]) algorithm (which has a certain cut applied).  
 588 Both loose and tight muons use the `Medium` ( $\sim 95\%$  selection efficiency [5]) algorithm (which has a certain  
 589 cut applied). Tight leptons additionally require that they are sufficiently isolated from other particles  
 590 produced in the collision. This is done by defining a cone of radius  $\Delta R = \sqrt{\Delta\eta^2 + \Delta\phi^2}$  around the parti-  
 591 cle of interest and summing the  $p_T$  of all the reconstructed particles surrounding the particle of interest,  
 592 situated within the cone. A quantity,  $I_{rel}$ , is then defined as,  $I_{rel} = \frac{\sum p_T(\text{surrounding candidate})}{p_T(\text{candidate})}$ , the ratio of  
 593 this sum to the  $p_T$  of the lepton candidate. If this value is large, is it likely that the particle of interest  
 594 originated from a jet (together with many other particles), whereas a prompt decay product resulting from  
 595 the hard scatter will have little to no energy surrounding it ( $I_{rel} \ll 1$ ). The `IsolationSelectionTool`  
 596 with the `PLVTight` ( $\sim 70\%$  efficiency [6]) and `PLVTight` ( $\sim 70\%$  efficiency at  $p_T = 30$  GeV [37]) algorithm  
 597 are used for tight electrons and tight muons respectively (following the current recommendations [85]).  
 598 In Table 5, a summary of the selection criteria for leptons is shown.

	Electrons		Muons	
	Tight	Loose	Tight	Loose
$p_T$ cuts	$p_T(\ell_1, \ell_2, \ell_3, \ell_4) > (28, 18, 10, 10)$ GeV			
Overlap Removal	Described in Section 4.2.4			
$\eta$ cuts	$ \eta(\ell_e)  < 2.47$ excluding $1.37 <  \eta(\ell_e)  < 1.52$		$ \eta(\ell_\mu)  < 2.5$	
Impact Parameters	$ \frac{d_0}{\sigma(d_0)}  < 5$ , $ z_0 \sin \theta  < 0.5$ mm		$ \frac{d_0}{\sigma(d_0)}  < 3$ , $ z_0 \sin \theta  < 0.5$ mm	
Identification WP	TightLH	LooseAndBLayerLH	Medium	Medium
Isolation WP	PLVTight	Not Used	PLVTight	Not Used

Table 5: A summary of the requirements applied for selecting tight and loose leptons ( $e, \mu$ ) is shown.

### 599 4.2.2 Jets

600 Jets are reconstructed using the anti- $k_t$  algorithm (See Section 3.2.6.4). The `AntiKt4EMPFflowjets` ( $\sim$   
 601 97% average efficiency with JVT (outlined in the subsequent paragraph)  $> 0.2$  [93]) algorithm (which  
 602 has a certain cut applied) is used, following the current recommendations [93]. The jet-vertex-tagger  
 603 (JVT) and the forward jet-vertex-tagger (fJVT) [50] are likelihood discriminant which aim to suppress  
 604 pile-up jets. The Medium algorithm (which has a certain cut applied) is used for the JVT and the fJVT  
 605 (following the current recommendations [83]). Additionally, a requirement that jets have a JVT value  
 606 greater than 0.5 is applied. In the same way as with leptons, ambiguities are removed where one detector  
 607 signal can result in multiple different reconstructed objects, via overlap removal (See Section 4.2.4). Jets  
 608 are required to be within  $p_T(\text{jet}) > 20$  GeV. These relatively loose  $p_T$  cuts are applied in an attempt to  
 609 increase our limited signal statistics. A forward jet is a signature of single top quark production, jets are  
 610 therefore required to have  $|\eta| < 4.5$  in order to include these forward jets.

### 611 4.2.3 $b$ -tagging

612 The DL1r  $b$ -tagger [76] was used to identify jets as  $b$ -jets (See Section 3.2.6.4). Different DL1r working  
 613 points are used to identify  $b$ -jets in our event selection (See Section 4.4). The working points are defined  
 614 as different cuts on the DL1r score corresponding to a  $b$ -jet tagging efficiency of 60%, 70%, 77% and  
 615 85%. The efficiency of the DL1r  $b$ -tagger is measured using control samples in data and in simulation.  
 616 From these measurements, correction factors are derived to correct the tagging rates in the simulation.  
 617 In the case of  $b$ -tagged jets, the correction factors and their uncertainties are estimated from data using  
 618 dileptonic  $t\bar{t}$  events [15, 12]. Sources of uncertainty affecting the  $b$ -tagging efficiencies are evaluated as  
 619 a function of jet  $p_T$ , including bin-to-bin correlations. Since this analysis is heavily statistically limited,  
 620 the amount of statistics in our regions are aimed to be maximized. In an attempt to achieve this goal in  
 621 the  $t\bar{t}Z$  CR,  $b$ -tagged jets were placed under *tight* and *loose* definitions. A tight  $b$ -tagged jet is defined  
 622 as a jet which passes the 77%, 70%, 65% or 60% DL1r  $b$ -tagger working point. A loose  $b$ -tagged jet is  
 623 defined as a jet which passes 85% DL1r  $b$ -tagger working point, but not the 77%, 70%, 65% or 60% DL1r  
 624  $b$ -tagger working points. Different numbers and definitions of tight and loose  $b$ -tagged jets were tried in  
 625 each region, with the final selection criteria being chosen which maximised the expected significance of  
 626  $\sigma(tWZ)$  (See Section 4.4.1).

**4.2.4 Overlap Removal Procedure**

An overlap removal procedure is performed to avoid instances where one detector signal can result in multiple different reconstructed objects. The overlap removal procedure is used on pre-selected leptons and jets. It is performed sequentially, in the following steps:

1. If the separation between a pre-selected electron and pre-selected muon is within  $\Delta R < 0.01$ , or they share a track, the pre-selected electron is discarded.
2. If the separation between a jet and a pre-selected electron is within  $\Delta R < 0.2$ , the jet is discarded.
3. Any remaining electron or muon closer than  $\Delta R = 0.4$  to a jet, is discarded.
4. If the distance between a jet and a pre-selected muon is  $\Delta R < 0.4$  and the jet has more than two associated tracks, then the muon is discarded, otherwise the jet is discarded.

**4.3 Kinematic cuts**

In order to suppress potential fakes and quarkonia (low mass resonances such as  $J/\psi$  and upsilon) a requirement that all OSSF lepton pairs have an invariant mass,  $m_{\text{OSSF}}$ , greater than 10 GeV is applied. The final state lepton charges must sum to zero. Therefore a requirement of  $\sum_{i=1}^4 \text{charge}(\ell_i) = 0$  is applied. The invariant mass of the OSSF lepton pair coming from the  $Z$  boson must equal the invariant mass of the  $Z$  boson, and noting that  $e,\mu$  reconstruction and identification in the ATLAS detector has a high efficiency [67], these OSSF leptons are used to reconstruct  $Z$  bosons with relatively high confidence. A  $Z$  candidate is defined in this analysis as an OSSF lepton pair with an invariant mass,  $m_{\text{OSSF}}$ , satisfying the condition,  $|m_{\text{OSSF}} - m_Z| < 30$  GeV, where  $m(Z)$  is the nominal  $Z$  boson mass (91.1876 GeV [55]). This wider mass window is used in order to cover the full range of the  $m(Z)$  distribution, in an attempt to increase the number of events which pass our baseline selections. Multiple  $Z$  candidates can be present in certain decay channels (e.g.  $eeee$ ,  $\mu\mu ee$ ,  $\mu\mu\mu\mu$ ). In these cases, the  $Z$  candidate which has an invariant mass closest to the nominal  $Z$  boson mass is chosen.

**4.4 Regions and Event Selection**

Two  $tWZ$  SRs are defined in an attempt to suppress and constrain the  $ZZ$  background. Both  $tWZ$  SRs are required to have exactly four tight leptons, exactly one  $Z$ -boson candidate, exactly one tight  $b$ -tagged jet (from the decay of the top quark) and greater than or equal to one jet. The two  $tWZ$  SR's differ by the flavours of their leptons which don't originate from the decay of a  $Z$ -boson (non- $Z$  leptons). The  $ZZ$  background has two  $Z$ -bosons which decay into a pair of OSSF lepton pairs, in order to mimic the  $tWZ$  signal. This is taken advantage of, to define a  $tWZ$  region enrich in  $ZZ$  background and one with a minimal  $ZZ$  background component. This is done by requiring that one of the  $tWZ$  SRs has its two non- $Z$  leptons to have opposite flavour and the other  $tWZ$  SR is required to have its non- $Z$  leptons to have the same flavour. These two disjoint  $tWZ$  SRs are named  $tWZ$  OF SR and  $tWZ$  SF SR respectively. It is therefore expected that the  $tWZ$  SF SR contains the majority of the  $ZZ$  background events across both  $tWZ$  SRs. In order to check the modelling of the most dominant

background components in our signal region,  $t\bar{t}Z$  and  $ZZb$  control regions are defined. The  $t\bar{t}Z$  control region has the same requirement on the number of reconstructed  $Z$  boson candidates in the signal region (due to a commonality on the number of  $Z$  bosons present in both processes), however it is required that there are at least two jets and that exactly two of these jets are  $b$ -tagged (corresponding to the  $b$ -quark jets originating from the two top quark decays). A  $ZZb$  region is defined, as opposed to a  $ZZ$  region, since the  $ZZ$  background present in the  $tWZ$  signal region contains exactly one  $b$ -tagged jet. Therefore defining a region with  $ZZ$  plus exactly one  $b$ -jet more closely resembles the  $ZZ$  background present in the signal region. In addition to this, mis-modelling of  $ZZ$  has been seen in other analyses [3, 39], further motivating the use of a  $ZZb$  control region over a  $ZZ$  CR. The  $ZZb$  CR requires exactly two  $Z$  boson candidates and exactly one  $b$ -tagged jet, resulting in an implicit requirement on the number of jets ( $N_{jet} \geq 1$ ).

Fake leptons are objects reconstructed as leptons, but do not correspond to the leptons that are of interest in our analysis. Fake leptons can be split up into two main categories, irreducible fakes and reducible fakes. Irreducible fakes are true leptons which do not come from the process of interest. Reducible fakes are objects which are mis-identified or incorrectly reconstructed as leptons. In the ATLAS detector, the probability for a fake to occur is very low. In order to constrain the fake lepton component contained within the  $t\bar{t}Z$  sample, a  $(tWZ)_{fake}$  CR is defined which is as similar as possible to the  $tWZ$  SRs but is enhanced in fakes. This is achieved by defining the  $(tWZ)_{fake}$  CR to inherit the same selection criteria as the  $tWZ$  SRs however, in this case, a requirement of exactly 3 tight leptons and exactly 1 loose (and NOT tight) lepton is applied. Loose leptons are required in this region, since looser leptons are more likely to be fakes compared to tighter leptons. A  $(t\bar{t}Z)_{fake}$  CR, requiring exactly 3 tight leptons and exactly 1 loose (and NOT tight) lepton, was tried as an alternative to the  $(tWZ)_{fake}$  CR, however a much larger suppression of fakes were observed in this region compared to the  $(tWZ)_{fake}$  CR. This suppression of fakes can be explained by the extra  $b$ -tagged jet requirement (exactly two  $b$ -tagged jets are required in the  $t\bar{t}Z$  region, compared to exactly one in the  $tWZ$  SRs (See Table 6)) which causes suppression of fakes via the overlap removal procedure (See Section 4.2.4). In Table 6, a summary of the final selection criteria and region definitions is shown.

#### 4.4.1 Optimization studies for event selection

In order to find the selection criteria for jets and leptons which maximized sensitivity to the  $tWZ$  signal, studies were performed by plotting the expected significance ( $Z_\mu^{exp}$ ) and expected upper limit ( $\mu_{up}^{exp}$ ) for different selection criteria. The fitting procedure as described in Section 4.9.1 was used to calculate the expected upper limits and expected significances in this study (these metrics are fully described later in Section 4.9.1). The same selection criteria and regions defined in Table 6 was used (unless otherwise specified), except for the selection(s) which were being optimised in each case. In Figure 8 the expected significance ( $Z_\mu^{exp}$ ) and expected upper limits ( $\mu_{up}^{exp}$ ) for different  $\eta(jet)$  cuts are shown. From Figure 8, it can be seen that the  $\eta(jet)$  cut which maximises the sensitivity of  $tWZ$  in the tetralepton channel is requiring that  $\eta(jet) < 4.5$ . This selection criteria was set for the  $\eta(jet)$  across all regions. In Figure 9 the expected significance ( $Z_\mu^{exp}$ ) and expected upper limits ( $\mu_{up}^{exp}$ ) for different  $p_T(jet)$  cuts are shown. From Figure 9, it can be seen that the  $p_T(jet)$  cut which maximises the sensitivity of  $tWZ$  is requiring that  $p_T(jet) > 20$  GeV. This selection criteria was set for the  $p_T(jet)$  across all regions. In Figure 10 the

Baseline selections								
$N_\ell = 4$								
	$p_T(\ell_1, \ell_2, \ell_3, \ell_4) > (28, 10, 10, 10)$ GeV							
	$p_T(\text{jet}) > 20$ GeV, $ \eta(\text{jet})  < 4.5$ , $\text{jvt} > 0.5$							
	$ \eta(\ell_e)  < 2.47$ excluding $1.37 <  \eta(\ell_e)  < 1.52$							
	$ \eta(\ell_\mu)  < 2.5$							
	$\sum_{i=1}^4 \text{charge}(\ell_i) = 0$							
All OSSF lepton pairs require $m_{\text{OSSF}} > 10$ GeV								
Regions								
$tWZ$ OF SR	$tWZ$ SF SR	$t\bar{t}Z$ CR	$ZZb$ CR	$(tWZ)$ fake C				
$N_\ell(\text{tight}) = 4$	$N_\ell(\text{tight}) = 4$	$N_\ell(\text{tight}) = 4$	$N_\ell(\text{tight}) = 4$	$N_\ell(\text{tight}) = N_\ell(\text{loose and NOT tight})$				
$N_Z \text{ candidate} = 1$	$N_Z \text{ candidate} = 1$	$N_Z \text{ candidate} = 1$	$N_Z \text{ candidate} = 2$	$N_Z \text{ candidate} = 2$				
$N_{\text{jet}} \geq 1$	$N_{\text{jet}} \geq 1$	$N_{\text{jet}} \geq 2$	$N_{\text{jet}} \geq 1$	$N_{\text{jet}} \geq 1$				
$N_{\text{b-jet}}(\text{tight}) = 1$	$N_{\text{b-jet}}(\text{tight}) = 1$	$N_{\text{b-jet}}(\text{tight}) \geq 1$ $N_{\text{b-jet}}(\text{loose}) \geq 0$	$N_{\text{b-jet}}(\text{tight}) = 1$	$N_{\text{b-jet}}(\text{tight}) = 1$				
$N_{\text{b-jet}}(\text{tight}) + N_{\text{b-jet}}(\text{loose}) = 2$								
Opp. Flavour non-Z leptons	Same Flavour non-Z leptons	-	-	-				

Table 6: A summary of the requirements applied for selecting events in the signal and control regions is shown.

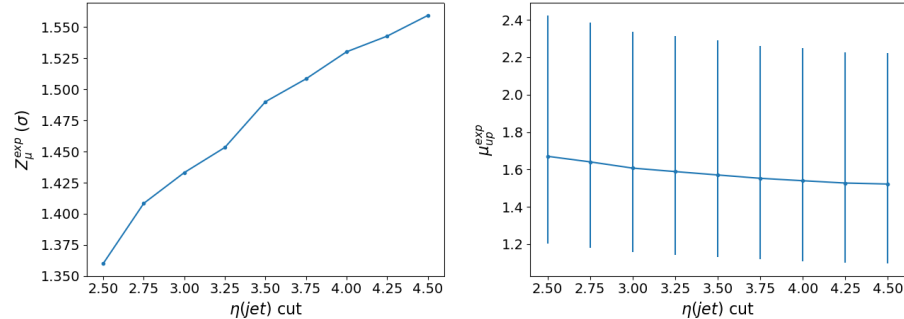


Figure 8: **Left:** The expected significance ( $Z_\mu^{\text{exp}}$ ) for different  $\eta(\text{jet})$  cuts is shown. The cuts applied on the  $\eta(\text{jet})$  are shown on the x-axis and the corresponding expected significance from the likelihood fit is shown on the y-axis. **Right:** Expected upper limit ( $\mu_{\text{up}}^{\text{exp}}$ ) for different  $\eta(\text{jet})$  cuts is shown. The cuts applied on the  $\eta(\text{jet})$  are shown on the x-axis and corresponding expected upper limits are shown on the y-axis. Error bars representing the total uncertainty on the expected upper limits are shown as vertical lines.

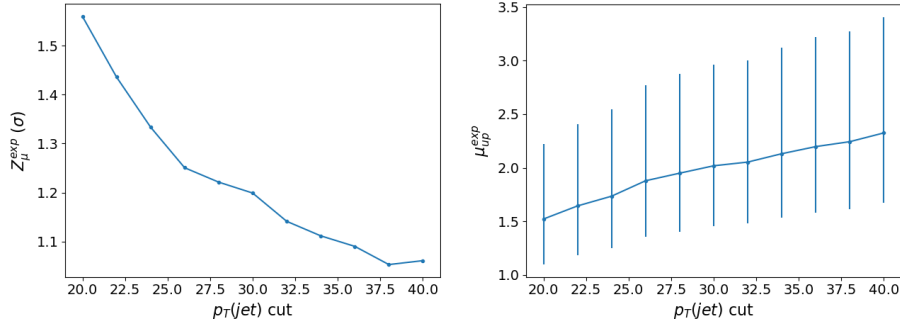


Figure 9: **Left:** The expected significance ( $Z_\mu^{exp}$ ) for different  $p_T(jet)$  cuts is shown. The cuts applied on the  $p_T(jet)$  are shown on the x-axis and the corresponding expected significance from the likelihood fit is shown on the y-axis. **Right:** Expected upper limit ( $\mu_{up}^{exp}$ ) for different  $p_T(jet)$  cuts is shown. The cuts applied on the  $p_T(jet)$  are shown on the x-axis and corresponding expected upper limits are shown on the y-axis. Error bars representing the total uncertainty on the expected upper limits are shown as vertical lines.

702 expected significance ( $Z_\mu^{exp}$ ) and expected upper limits ( $\mu_{up}^{exp}$ ) for a range of different configurations of DL1r  $b$ -tagged jet working points across different regions. From Figure 10, it can be seen that requiring

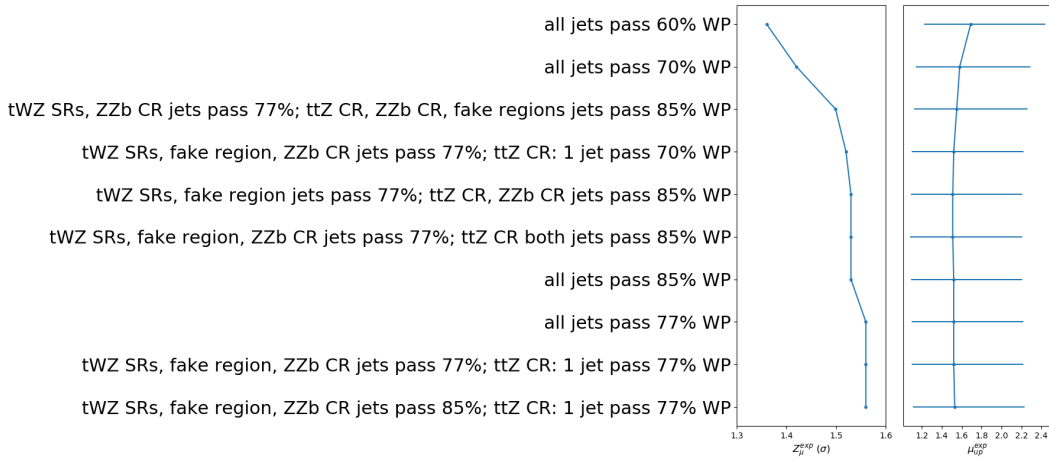


Figure 10: Expected significance ( $Z_\mu^{exp}$ ) and expected upper limit ( $\mu_{up}^{exp}$ ) for different configurations of DL1r  $b$ -tagged jet working points is shown. The common y-axis shows the different configurations of DL1r  $b$ -tagged jet working points. On the left panel, the expected significance from the likelihood fit is shown on the x-axis. On the right panel, the expected upper limit from the likelihood fit is shown on the x-axis (with the corresponding total uncertainty represented by horizontal lines).

703  
 704 that  $b$ -tagged jets pass the 77% DL1r WP in the  $tWZ$  SR,  $(tWZ)_{fake}$  CR and the  $ZZb$  CR and that  
 705 at least one  $b$ -tagged jet in the  $t\bar{t}Z$  SR passes the 77% DL1r WP (the other jet is just required to pass  
 706 the 85% DL1r WP) maximises the sensitivity overall (compared to the other investigated configurations).  
 707 This configuration was chosen  $b$ -tagged jets. The  $p_T(L$  Lepton) is constrained by the single lepton triggers  
 708 4. A cut was chosen to be applied on the  $p_T(NL$  Lepton) slightly tighter than the tightest single lepton  
 709  $p_T$  cut in the trigger. The  $p_T(NL$  Lepton) cut can be optimized by comparing the expected significance  
 710 and limit for a range of  $p_T(NL$  Lepton) cuts to determine the cut which maximizes sensitivity. In Figure  
 711 11 the expected significance ( $Z_\mu^{exp}$ ) and expected upper limits ( $\mu_{up}^{exp}$ ) for different  $p_T(NL$  Lepton) cuts is

shown. Since there is a very small change between the different  $p_T(\text{NL Lepton})$  cuts on the sensitivity

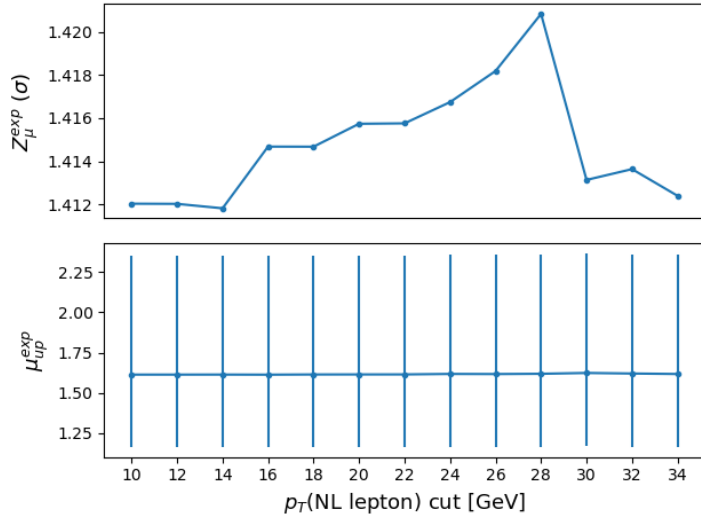


Figure 11: Expected significance ( $Z_\mu^{\text{exp}}$ ) and expected upper limit ( $\mu_{\text{up}}^{\text{exp}}$ ) for different  $p_T(\text{NL Lepton})$  cuts is shown. The common x-axis shows cut applied to the  $p_T$  of the next-to-leading lepton. On the top panel, the expected significance from the likelihood fit is shown on the y-axis. On the bottom panel, the expected upper limit from the likelihood fit is shown on the y-axis (with the corresponding total uncertainty represented by vertical lines).

712  
 713 of  $tWZ$ , a  $p_T(\text{NL Lepton})$  cut is applied at 18 GeV (avoiding a  $p_T$  cut near the sharp drop in expected  
 714 significance after 28 GeV), therefore applying a cut above the tightest, looser dilepton trigger  $p_T$  cut (17  
 715 GeV) to suppress any systematic from the modelling of the trigger efficiency.

## 716 4.5 Signal and Control Regions

717 In this section, expected number of events in each region are shown. For each figure in  
 718 this section, the data is given by the black points and the MC predictions for each process are given by  
 719 the filled histograms. The vertical lines on the data points represent the statistical uncertainty in the  
 720 data and the diagonally-lined bands represent the total (statistical and systematic added in quadrature)  
 721 uncertainty. The lower panel in each plot shows the ratios of the data to the theoretical predictions. In  
 722 order to suppress a bias towards large signal observations in the development of the analysis, data has  
 723 not been analysed in bins where the expected  $\frac{\text{signal}}{\text{background}}$  exceeds 0.1. This is known as blinding. Blinded  
 724 bins in the CRs are shaded with black diagonal lines and their data points are omitted. All data points  
 725 are omitted in the SRs. In Table 7, the expected number of events for each sample in each region are  
 726 shown. The finite number of events expected to be observed in data (MC simulation) carries an associated  
 727 statistical uncertainty. To first order, this uncertainty can be written as the square root of the expected  
 728 number of events to be observed in data. In contrast to this, predictions based on MC simulation carry  
 729 uncertainties due to the finite number of simulated events utilised. This uncertainty can be quantified  
 730 by the Number of Equivalent Events [47],  $N_{\text{equiv}}$ , which relates the sample of  $N$  events (weighted by MC  
 731 event weights) to  $N_{\text{equiv}}$  events with all MC event weights equal to 1, that would have the same relative

		$tWZ$ OF SR	$tWZ$ SF SR	$t\bar{t}Z$ CR	$ZZb$ CR	$(tWZ)_{fake}$ CR
$t\bar{t}Z$ $t\bar{t}Z$ fakes $tWZ$ $ZZ$	$t\bar{t}Z$	$13.9 \pm 1.8$	$10.1 \pm 1.4$	$31.7 \pm 4.5$	$5.3 \pm 0.7$	$19.1 \pm 2.5$
	$t\bar{t}Z$ fakes	$0.068 \pm 0.048$	$0.032 \pm 0.026$	$0.07 \pm 0.04$	$0.05 \pm 0.03$	$5.0 \pm 2.5$
	$tWZ$	$3.8 \pm 0.4$	$2.6 \pm 0.3$	$2.6 \pm 0.9$	$1.4 \pm 0.2$	$5.0 \pm 0.7$
	$ZZ$	$0.5 \pm 0.2$	$8.8 \pm 2.7$	$1.2 \pm 0.4$	$46 \pm 14$	$7.8 \pm 2.4$
other	$t\bar{t}$	$6e-06 \pm 3e-06$	$0.25 \pm 0.44$	$0.27 \pm 0.22$	$6e-06 \pm 3e-06$	$2.4 \pm 0.9$
	$tZq$	$0.08 \pm 0.04$	$0.08 \pm 0.04$	$0.06 \pm 0.03$	$0.06 \pm 0.02$	$4.9 \pm 0.8$
	$t\bar{t}W$	$0.007 \pm 0.007$	$0.003 \pm 0.003$	$6e-06 \pm 3e-06$	$0.002 \pm 0.006$	$1.0 \pm 0.3$
	$WZ$	$0.04 \pm 0.02$	$0.04 \pm 0.02$	$0.013 \pm 0.013$	$0.05 \pm 0.03$	$1.8 \pm 0.4$
	$t\bar{t}t$	$0.0010 \pm 0.0008$	$0.002 \pm 0.001$	$0.014 \pm 0.004$	$6e-06 \pm 3e-06$	$0.010 \pm 0.004$
	$t\bar{t}\bar{t}$	$0.0093 \pm 0.0081$	$0.011 \pm 0.009$	$0.057 \pm 0.021$	$6e-06 \pm 3e-06$	$0.02 \pm 0.01$
	$t\bar{t}WW$	$0.029 \pm 0.026$	$0.03 \pm 0.02$	$0.26 \pm 0.10$	$0.01 \pm 0.03$	$0.20 \pm 0.06$
	$VVV(V = W/Z)$	$0.28 \pm 0.09$	$0.20 \pm 0.06$	$0.07 \pm 0.02$	$0.20 \pm 0.05$	$0.3 \pm 0.1$
	$t\bar{t}H$	$0.85 \pm 0.18$	$0.67 \pm 0.14$	$2.0 \pm 0.4$	$0.15 \pm 0.04$	$2.2 \pm 0.5$
Total		$19.7 \pm 2.0$	$22.9 \pm 3.1$	$38.4 \pm 4.6$	$53.2 \pm 14.0$	$49.5 \pm 4.8$
data		-	-	36	49	57

Table 7: The expected number of events for each sample in each region is shown.

statistical fluctuation. The Number of Equivalent Events,  $N_{equiv}$ , can be written as,

$$N_{equiv} = \frac{(\sum_i^N w_i)^2}{\sum_i^N w_i^2} \quad (4.2)$$

where  $w_i$  is the MC event weight for event  $i$ . The standard uncertainty of  $N_{equiv}$  is given by  $u(N_{equiv}) = \sqrt{N_{equiv}}$ . The Number of Equivalent Events for each sample in each region can be studied in order to ensure that the number of events simulated for a given process is large in comparison to the number of events expected for that process in data, thereby ensuring that uncertainties from MC statistics will be small (or sub-leading). In Table 8, the number of equivalent events,  $N_{equiv}$ , is shown for each sample in each region.  $N_{equiv}$  is much larger compared to the number of expected events (See Table 7) for the signal

	$tWZ$ OF SR	$tWZ$ SF SR	$t\bar{t}Z$ CR	$ZZb$ CR	$(tWZ)_{fake}$ CR
	$N_{equiv}$	$N_{equiv}$	$N_{equiv}$	$N_{equiv}$	$N_{equiv}$
$tWZ$	$6463 \pm 80$	$4153 \pm 64$	$4800 \pm 69$	$2497 \pm 50$	$8645 \pm 93$
$t\bar{t}Z$	$1364 \pm 37$	$1031 \pm 32$	$3237 \pm 57$	$561 \pm 24$	$1923 \pm 44$
$ZZ$	$51 \pm 7$	$975 \pm 31$	$268 \pm 16$	$7023 \pm 84$	$969 \pm 31$
other	$748 \pm 27$	$2.5 \pm 1.6$	$4.2 \pm 2.1$	$255 \pm 16$	$21.5 \pm 4.6$
$t\bar{t}Z$ fakes	$6.7 \pm 2.6$	$1.3 \pm 1.1$	$16.1 \pm 4.0$	$7.2 \pm 2.7$	$484 \pm 22$
Total	$8633 \pm 93$	$6163 \pm 79$	$8326 \pm 91$	$10344 \pm 102$	$12044 \pm 110$

Table 8: The number of equivalent events,  $N_{equiv}$ , is shown for each sample in each region.

and background processes in all regions. This tells us that there is a large number of simulated events for these samples. Therefore ensuring that uncertainties resulting from MC statistics will be small (or sub-leading).

### 742 4.5.1 $tWZ$ OF SR

743 In this section, comparisons of simulation and data for different variables in the  $tWZ$  OF SR are shown.  
 744 In Figure 12, comparisons of simulation and data for  $p_T$ ,  $\eta$  and  $\phi$  for leading (L) leptons and leading (NL)  
 745 jets in the  $tWZ$  OF SR are shown.

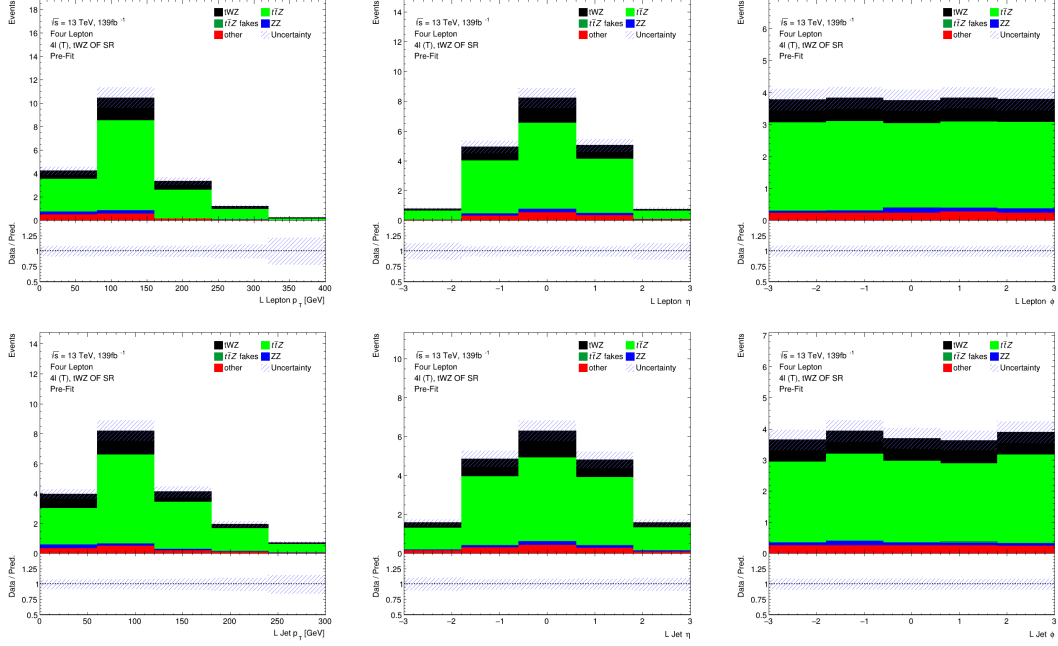


Figure 12: Comparisons of simulation and data of  $p_T$ ,  $\eta$  and  $\phi$  for leading (L) leptons (top row) and leading (NL) jets (bottom row) in the  $tWZ$  OF SR are shown.

746 The bins in all of the plots in Figure 12 have  $\frac{signal}{background}$  exceeding 0.1. This region is enriched in  $tWZ$   
 747 signal events. In Figure 13, comparisons of simulation and data of  $H_T$  (scalar sum of Jet  $p_T$ ), the Number  
 748 of jets, the scalar sum of  $b$ -tagged jet  $p_T$  and the number of  $b$ -tagged jets in the  $tWZ$  OF SR are shown.  
 749 All bins for each plot in Figure 13 have  $\frac{signal}{background}$  exceeding 0.1 and are therefore blinded. This region is  
 750 therefore enriched in  $tWZ$  signal events.

### 751 4.5.2 $tWZ$ SF SR

752 In this section, expected number of events of variables in the  $tWZ$  SF SR are shown. In Figure 14,  
 753 comparisons of simulation and data of  $p_T$ ,  $\eta$  and  $\phi$  for leading (L) leptons and leading (NL) jets in the  
 754  $tWZ$  SF SR are shown. All bins for each plot in Figure 14 have  $\frac{signal}{background}$  exceeding 0.1 and are therefore  
 755 blinded. This region is therefore enriched in  $tWZ$  signal events. In Figure 15, comparisons of simulation  
 756 and data of  $H_T$  (scalar sum of Jet  $p_T$ ), the Number of jets, the scalar sum of  $b$ -tagged jet  $p_T$  and the  
 757 number of  $b$ -tagged jets in the  $tWZ$  SF SR are shown. The vast majority of bins in each plot in Figure 15  
 758 have  $\frac{signal}{background}$  exceeding 0.1 and are therefore blinded. This region is therefore enriched in  $tWZ$  signal  
 759 events. The deviations in data and simulation in the two bins (in the  $HT$  and  $\sigma b$  jet  $p_T$  distributions)  
 760 which are not blinded, are within the expected uncertainties.

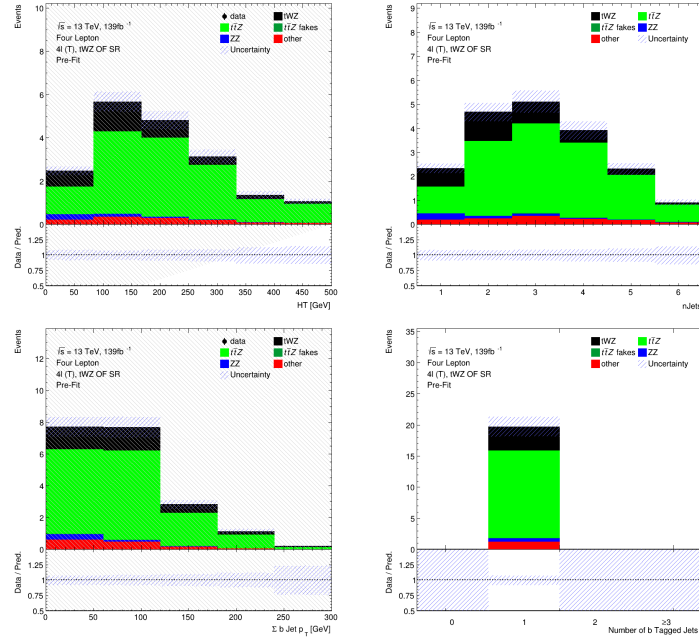


Figure 13: Comparisons of simulation and data of  $H_T$  (scalar sum of Jet  $p_T$ ), the Number of jets, the scalar sum of  $b$ -tagged jet  $p_T$  and the number of  $b$ -tagged jets (top left to bottom right) in the  $tWZ$  OF SR are shown.

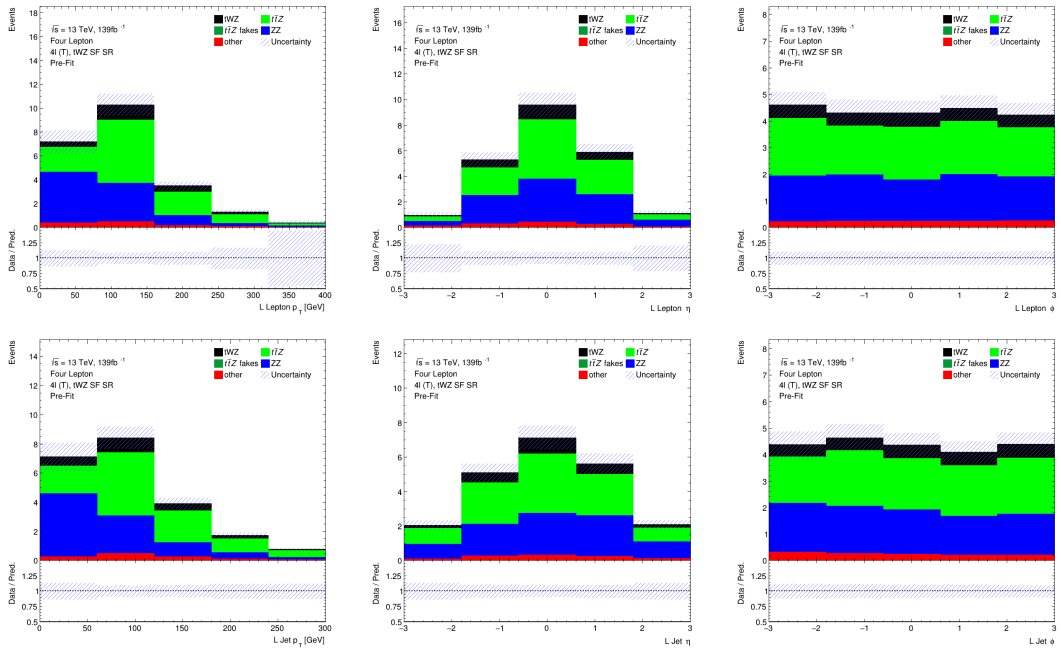


Figure 14: Comparisons of simulation and data of  $p_T$ ,  $\eta$  and  $\phi$  for leading (L) leptons (top row) and leading (NL) jets (bottom row) in the  $tWZ$  SF SR are shown.

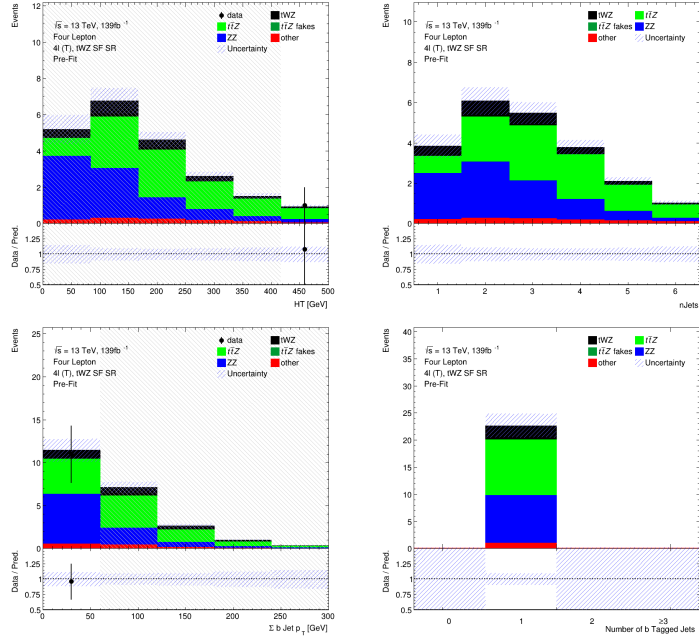


Figure 15: Comparisons of simulation and data of  $H_T$  (scalar sum of Jet  $p_T$ ), the Number of jets, the scalar sum of  $b$ -tagged jet  $p_T$  and the number of  $b$ -tagged jets (top left to bottom right) in the  $tWZ$  SF SR are shown.

### 761 4.5.3 $t\bar{t}Z$ CR

762 In this section, expected number of events of variables in the  $t\bar{t}Z$  CR are shown. In Figure 16, comparisons  
 763 of simulation and data of  $p_T$ ,  $\eta$  and  $\phi$  for leading (L) leptons and leading (NL) jets in the  $t\bar{t}Z$  CR are  
 764 shown. The majority of the deviations in data and simulation for each plot in Figure 16 are within the  
 765 expected uncertainties. The few plots which have bins where there is a disagreement between data and  
 766 simulation are either within  $2\sigma$  (L Jet  $\phi$ ) or  $3\sigma$  (L Jet  $\eta$ ) standard uncertainties from one another, or are  
 767 show more than a  $3\sigma$  (L Lepton  $p_T$ ) disagreement. The disagreement in the L Lepton  $p_T$  distribution  
 768 could be due to statistical fluctuations in data or simulation, since there are so few events in these bins.  
 769 In Figure 17, comparisons of simulation and data of  $H_T$  (scalar sum of Jet  $p_T$ ), the Number of jets, the  
 770 scalar sum of  $b$ -tagged jet  $p_T$  and the number of  $b$ -tagged jets in the  $t\bar{t}Z$  CR are shown. Almost all of  
 771 the deviations in data and simulation for each plot in Figure 17 are within the expected uncertainties.  
 772 There is a  $2\sigma$  disagreement in one of the bins in the nJets distribution and a large disagreement ( $> 5\sigma$ )  
 773 in one of the bins in the HT distribution. The large disagreement between data and simulation in the  
 774 HT distribution is surprising since all other bins in the distribution agree within  $1\sigma$  uncertainties, and it  
 775 is therefore not fully understood.

### 776 4.5.4 $ZZb$ CR

777 In this section, expected number of events of variables in the  $ZZb$  CR are shown. In Figure 18, comparisons  
 778 of simulation and data of  $p_T$ ,  $\eta$  and  $\phi$  for leading (L) leptons and leading (NL) jets in the  $ZZb$  CR are  
 779 shown. Most of the deviations in data and simulation for each plot in Figure 18 are within the expected  
 780 uncertainties. There are a few bins with  $2\sigma$  and  $> 2\sigma$  disagreements between data and simulation in the

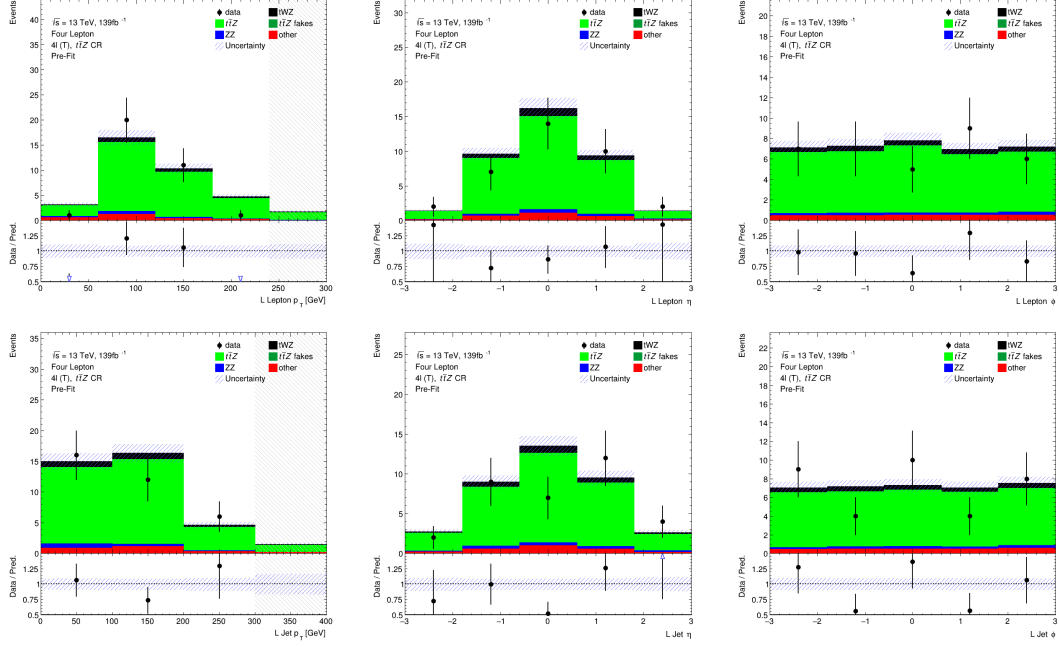


Figure 16: Comparisons of simulation and data of  $p_T$ ,  $\eta$  and  $\phi$  for leading (L) leptons (top row) and leading (NL) jets (bottom row) in the  $t\bar{t}Z$  CR are shown.

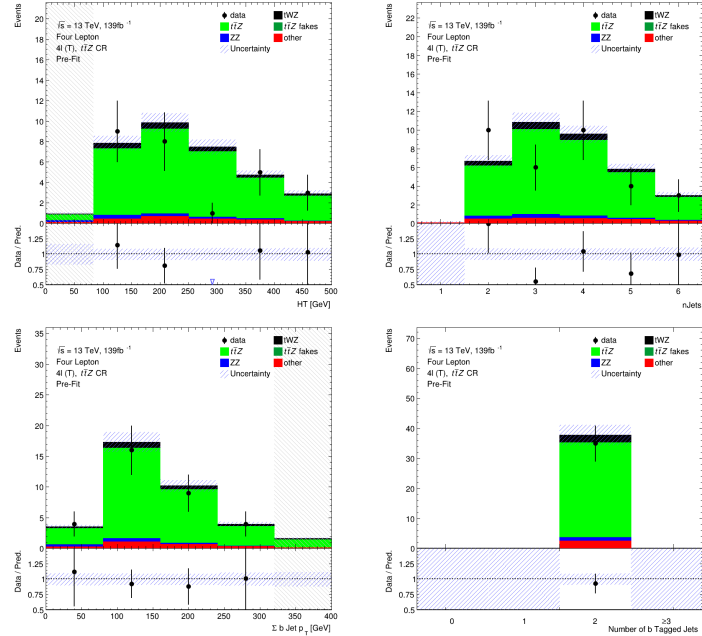


Figure 17: Comparisons of simulation and data of  $H_T$  (scalar sum of Jet  $p_T$ ), the Number of jets, the scalar sum of  $b$ -tagged jet  $p_T$  and the number of  $b$ -tagged jets (top left to bottom right) in the  $t\bar{t}Z$  CR are shown.

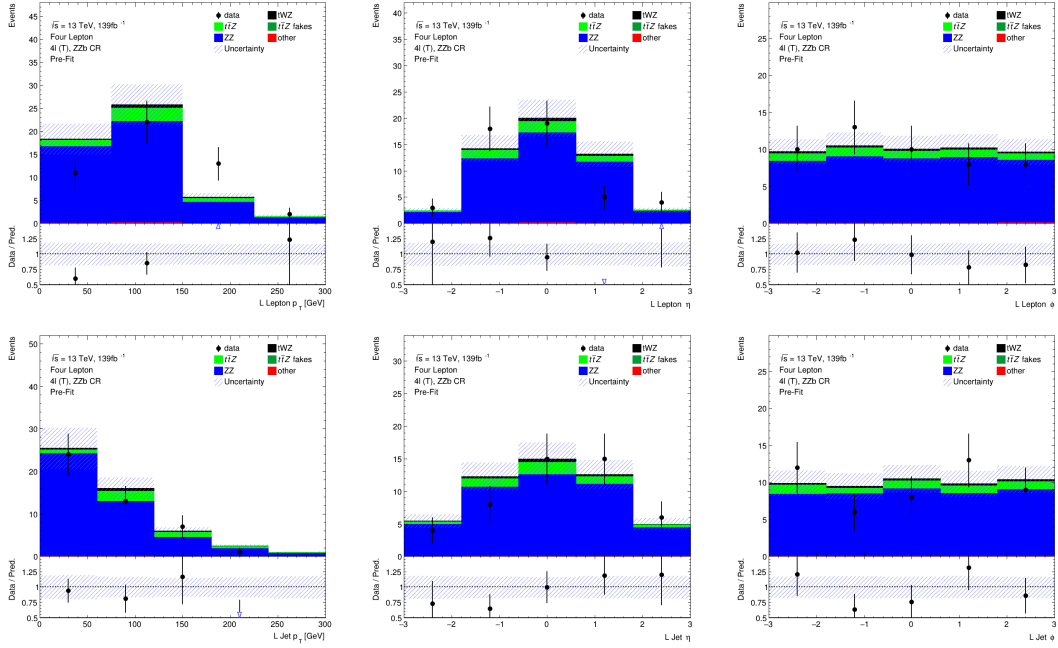


Figure 18: Comparisons of simulation and data of  $p_T$ ,  $\eta$  and  $\phi$  for leading (L) leptons (top row) and leading (NL) jets (bottom row) in the  $ZZb$  CR are shown.

781 L Lepton  $p_T$ , L Lepton  $\eta$  and L Jet  $p_T$  distributions, with the disagreement being much more noticeable  
 782 in the L Lepton distributions. This could suggest some mis-modelling for L Leptons in this region. In  
 783 Figure 19, comparisons of simulation and data of  $H_T$  (scalar sum of Jet  $p_T$ ), the Number of jets, the  
 784 scalar sum of  $b$ -tagged jet  $p_T$  and the number of  $b$ -tagged jets in the  $ZZb$  CR are shown. Most of the  
 785 deviations in data and simulation for each plot in Figure 18 are within the expected uncertainties.

#### 786 4.5.5 $(tWZ)_{\text{fake}}$ CR

787 In this section, expected number of events of variables in the  $(tWZ)_{\text{fake}}$  CR are shown. In Figure 20,  
 788 comparisons of simulation and data of  $p_T$ ,  $\eta$  and  $\phi$  for leading (L) leptons and leading (NL) jets in the  
 789  $(tWZ)_{\text{fake}}$  CR are shown. The vast majority of bins in each plot in Figure 20 have  $\frac{\text{signal}}{\text{background}}$  exceeding  
 790 0.1 and are therefore blinded. This region is therefore enriched in  $tWZ$  signal events. Most deviations  
 791 in data and simulation in the bins which are not blinded, are within the expected uncertainties. Only  
 792 two out of seven unblinded bins are not within expected uncertainties and are within a  $2\sigma$  uncertainty.  
 793 In Figure 21, comparisons of simulation and data of  $H_T$  (scalar sum of Jet  $p_T$ ), the Number of jets, the  
 794 scalar sum of  $b$ -tagged jet  $p_T$  and the number of  $b$ -tagged jets in the  $(tWZ)_{\text{fake}}$  CR are shown.  
 795 The majority of bins in each plot in Figure 21 have  $\frac{\text{signal}}{\text{background}}$  exceeding 0.1 and are therefore blinded.  
 796 This region is therefore enriched in  $tWZ$  signal events. Most deviations in data and simulation in the  
 797 bins which are not blinded, are within the expected uncertainties. Only two out of seven unblinded bins  
 798 are not within expected uncertainties and are within a  $2\sigma$  uncertainty.

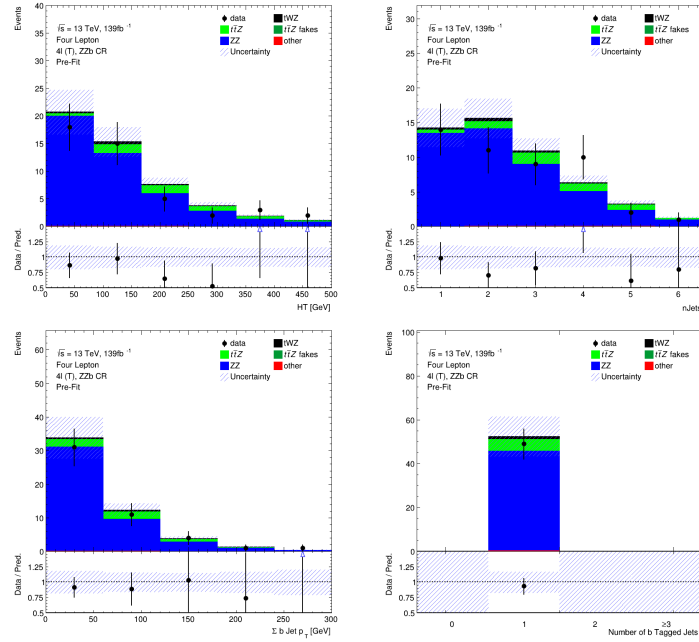


Figure 19: Comparisons of simulation and data of  $H_T$  (scalar sum of Jet  $p_T$ ), the Number of jets, the scalar sum of  $b$ -tagged jet  $p_T$  and the number of  $b$ -tagged jets (top left to bottom right) in the  $ZZb$  CR are shown.

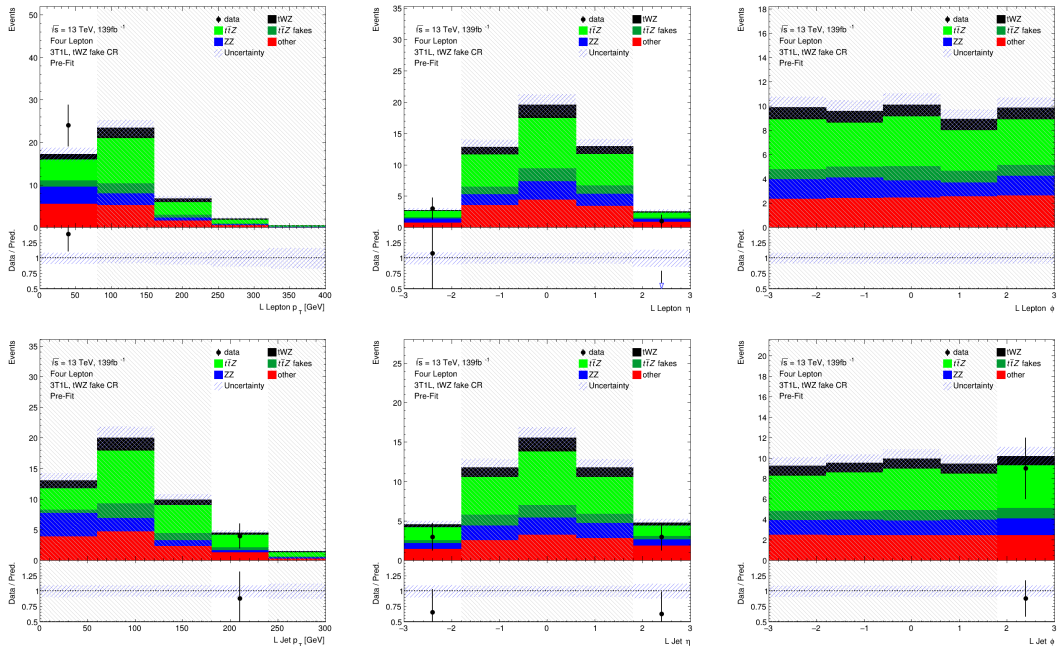


Figure 20: Comparisons of simulation and data of  $p_T$ ,  $\eta$  and  $\phi$  for leading (L) leptons (top row) and leading (NL) jets (bottom row) in the  $(tWZ)$ fake CR are shown.

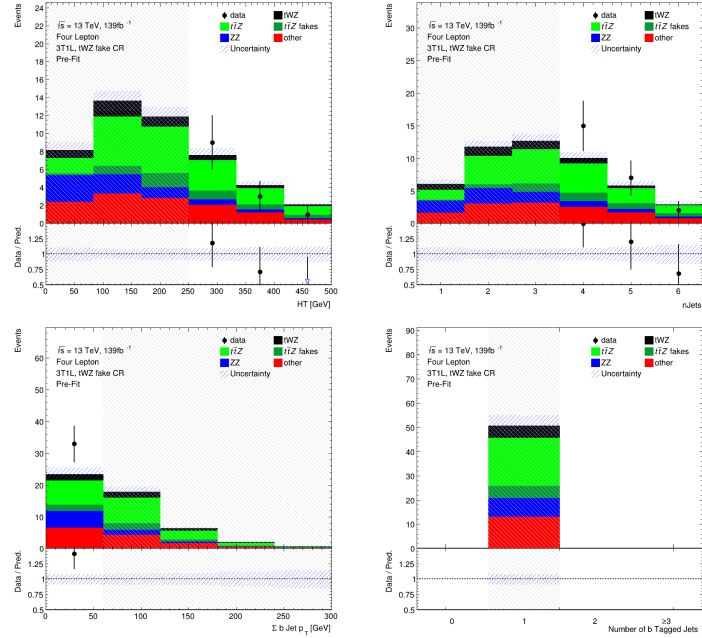


Figure 21: Comparisons of simulation and data of  $H_T$  (scalar sum of Jet  $p_T$ ), the Number of jets, the scalar sum of  $b$ -tagged jet  $p_T$  and the number of  $b$ -tagged jets (top left to bottom right) in the  $(tWZ)_{\text{fake}}$  CR are shown.

## 799 4.6 Fake Lepton Estimation

800   Fake leptons are physics objects reconstructed as leptons, but do not correspond to the leptons which  
 801   originate from the hard scatter process or those physics objects that are mis-identified as leptons.  
 802   The sources of fake leptons include those originating from heavy hadron decays, light hadron de-  
 803   cays or via the conversion of a photon to a lepton. In the ATLAS detector, the probability for a fake  
 804   to occur is very low. In this section, the method used to estimate the fake lepton contribution is described.  
 805

806   As  $t\bar{Z}$  is the dominant background process ( $\sim 75\%$  of the total background contribution), it is assumed  
 807   that  $t\bar{Z}$  will also dominate the events containing fake leptons. The fake lepton efficiency,  $\epsilon$ , can be  
 808   written as  $\epsilon = \frac{N_{\text{fake}}^{\text{tight}}}{N_{\text{fake}}^{\text{loose}}}$ , where  $N_{\text{fake}}^{\text{tight}}$  is the number of fake leptons which pass the tight lepton selection  
 809   (See Section 4.2.1) and  $N_{\text{fake}}^{\text{loose}}$  is the number of fake leptons which pass the loose lepton selection (See  
 810   Section 4.2.1). The probability of one fake lepton to occur,  $P(\text{one fake } \ell)$ , is proportional to  $\epsilon_1 \ll 1$  [65,  
 811   82] and the probability for two fakes to occur is,  $P(\text{two fakes } \ell)$ , is proportional to  $\epsilon_2 < \epsilon_1 \ll 1$ . In this  
 812   analysis, an estimation of the fake lepton component to the highest order is investigated and therefore  
 813   the case where at least one fake lepton occurs in a  $t\bar{Z}$  event is considered.

814  
 815   Firstly, the dominant  $t\bar{Z}$  background is split up into  $t\bar{Z}$  and  $(t\bar{Z})_{\text{fake}}$  components. Secondly, a  
 816    $(tWZ)_{\text{fake}}$  CR (See Section 4.4) is defined which is enhanced in fakes and aims to constrain the  $(t\bar{Z})_{\text{fake}}$   
 817   background in the SR. All events which contribute to the  $(t\bar{Z})_{\text{fake}}$  background are determined by the  
 818   **IFF Truth Classifier** [59]. The **IFF Truth Classifier** is a tool which aims to classify leptons based  
 819   off their truth information. It uses the more general **MCTruthClassifier** [70] tool's output as input and

820 returns one of the following lepton categories: `Unknown`, `KnownUnknown` (leptons which can (in principle) be  
 821 classified, but the `MCTruthClassifier` fails to classify the lepton's truth type or origin), `IsoElectron`,  
 822 `ChargeFlipIsoElectron`, `PromptMuon`, `PromptPhotonConversion`, `ElectronFromMuon`, `TauDecay`,  
 823 `BHadronDecay`, `CHadronDecay` or `LightFlavorDecay` (More details [59]). Given these categories, leptons  
 824 are considered as fake if they are classified as `PromptPhotonConversion`, `BHadronDecay`, `CHadronDecay`  
 825 or `LightFlavorDecay` (i.e. a lepton originating from the decay of a  $b$ -Hadron,  $c$ -Hadron or light-flavour  
 826 jet). Events which contribute to the  $(t\bar{t}Z)$ <sub>fake</sub> background are those where at least one lepton from the  
 827  $t\bar{t}Z$  sample are classified by the IFF Truth Classifier with one of the four aforementioned categories.

828

829 The  $(tWZ)$ <sub>fake</sub> CR aims to be as similar as possible to the  $tWZ$  SRs, but enhanced in fakes. This CR  
 830 can then be used to constrain the normalisation of the  $(t\bar{t}Z)$ <sub>fake</sub> template. To ensure that this region is  
 831 enhanced in fakes, it is required that it contains 3 tight leptons and 1 loose lepton, since loose leptons  
 832 are more likely to be fakes. Leptons from heavy decays are produced in jets and are typically surrounded  
 833 by other energetic particles. Since the loose lepton definition relaxes the isolation requirement, leptons  
 834 satisfying the loose criteria are more enhanced in these fake leptons. By using the  $p_T$  of the loose lepton  
 835 ( $p_T(\text{Loose Lepton})$ ) in this region as the variable used in the fit, the shape (and normalisation) of the  
 836  $(t\bar{t}Z)$ <sub>fake</sub> template can be constrained. In Figure 22, the number of leptons classified as fake and the relative  
 837 dominance of the different classifications for fake leptons, split up by their IFF Truth classification, in  
 838 each region are shown.

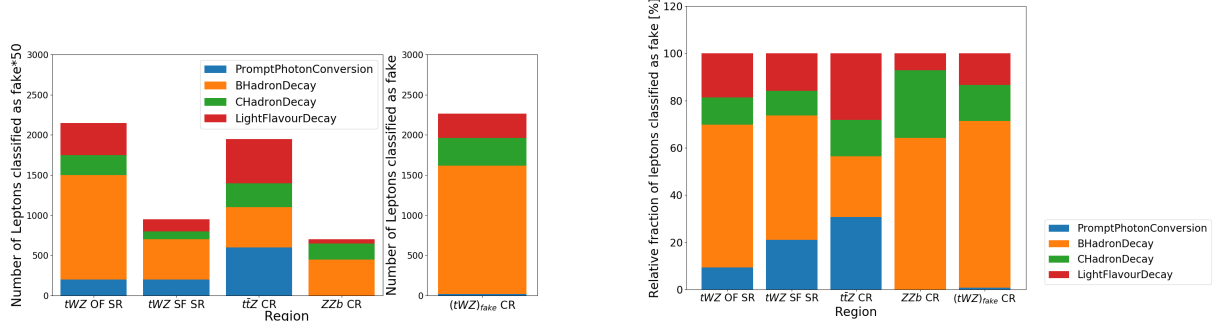


Figure 22: **Left:** The number of leptons classified as fake, split up by their IFF Truth classification, in each region is shown. The left panel shows the number of leptons classified as fakes, scaled by a factor of 50, on the y-axis. The right panel shows the number of leptons classified as fakes (unscaled), on the y-axis. The different signal and control regions are shown on the x-axes of the left and right panels. The different coloured stacked histograms correspond to the IFF truth classification of the leptons, as shown in the legend. **Right:** The relative dominance of the different classifications for fake leptons (classified by the IFF truth classified) in each region, is shown. The relative dominance of leptons classified as fakes, as a fraction of the total number of fake leptons (in each region), is shown on the y-axis. The different signal and control regions are shown on the x-axis. The different coloured stacked histograms correspond to the IFF truth classification of the leptons, as shown in the legend.

839 The plot on the left illustrates that there is a large amount of fake leptons which pass our selection criteria  
 840 for the  $(tWZ)$ <sub>fake</sub> CR, compared to remaining four regions. Therefore there is a significant amount  
 841 of fake leptons present in the  $(tWZ)$ <sub>fake</sub> CR which allow the fake lepton component to be sufficiently  
 842 constrained. The plot on the right illustrates that the majority of fake leptons which pass our selection

843 criteria originate from the decay of  $b$ -hadrons, in all regions but the  $t\bar{t}Z$  CR. The smaller proportion of fake  
 844 leptons originating from  $b$ -hadron decays in the  $t\bar{t}Z$  CR could possibly be due to statistical fluctuations  
 845 resulting from the low number of fake leptons which pass our selection criteria in this region ( $\sim 40$  fake  
 846 leptons). In Figure 23, the amount of fake and real  $t\bar{t}Z$  events which pass our selection criteria, in each  
 847 region, is shown.

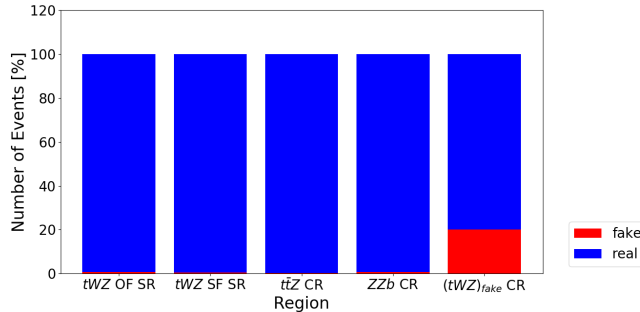


Figure 23: The percentage of fake and real  $t\bar{t}Z$  events which pass our selection criteria, in each region, is shown. The relative number of fake and real events (in % of the total number of events in the nominal and fake  $t\bar{t}Z$  background samples) is shown on the y-axis. The different signal and control regions are shown on the x-axis. The blue and red histograms represent the percentage of real and fake events (out of the total number of events in the nominal and fake  $t\bar{t}Z$  background samples), respectively.

848 Around 20% of all  $t\bar{t}Z$  events are classified as fake events (having one or more of its leptons being classified  
 849 as fake) in the  $(tWZ)_{fake}$  CR. The  $tWZ$  OF SR,  $tWZ$  SF SR,  $t\bar{t}Z$  CR and  $ZZb$  CR have less than 1% of  
 850 their total  $t\bar{t}Z$  events being fake. The significant fraction of fake  $t\bar{t}Z$  events present in the  $(tWZ)_{fake}$  CR  
 851 allows the  $t\bar{t}Z$  fake background to be sufficiently constrained by the  $(tWZ)_{fake}$  CR.

## 852 4.7 Improving signal vs background discrimination

853 The presence of different numbers of top quarks is a key discriminator between signal and the dominant  
 854 background process,  $t\bar{t}Z$ . This information is aimed to be exploited by reconstructing  $\ell b$  systems as a  
 855 proxy for top quarks (since,  $t \rightarrow W(\rightarrow \ell\nu)b$ ). This is done in two ways, firstly, by implementation of  
 856 a kinematic reconstruction algorithm (Two Neutrino Scanning Method) which aims to determine the  
 857 likelihood of an event containing two top quarks and secondly, by implementing a Boosted Decision Tree  
 858 (BDT) which is used to distinguish between  $\ell b$  systems that originate from top quarks and  $\ell b$  systems which  
 859 do not originate from top quarks. In this thesis, this BDT is referred to as an *object-level* BDT. Certain  
 860 variables constructed from event information show discrimination between signal and background events.  
 861 This information can be exploited to discriminate between signal and background events by constructing  
 862 a BDT which uses these discriminating variables for training. A BDT is implemented and is used to  
 863 discriminate between  $tWZ$  events and its major backgrounds,  $t\bar{t}Z$  and  $ZZ$ . Furthermore, this BDT takes  
 864 information from the kinematic reconstruction algorithm and the object-level BDT in order to maximize  
 865 its discriminating power. In this thesis, this BDT is referred to as an *event-level* BDT. The discriminator  
 866 output from the object-level BDT can be converted to a variable which can then be used as an input to  
 867 the event-level BDT.

### 4.7.1 Two Neutrino Scanning Method ( $2\nu$ SM) Algorithm

The difference in the number of resonant top quarks in the  $tWZ$  signal and the dominant background,  $t\bar{t}Z$ , is a key feature which can be exploited in order to discriminate between these two processes. In Section 4.7.3, a BDT was implemented which exploits this information by aiming to identify  $\ell b$  systems originating from top quarks. In this section, a kinematic reconstruction algorithm (Two Neutrino Scanning Method) is implemented which exploits the same feature. The Two Neutrino Scanning Method ( $2\nu$ SM) algorithm<sup>1</sup> [69, 68] aims to reconstruct  $t\bar{t}$  systems in the  $2\ell$ ,  $3\ell$  and  $4\ell$  final states (e.g.  $2\ell$  case:  $t\bar{t} \rightarrow \ell^+\nu_\ell b\ell^-\bar{\nu}_\ell b$ ). The  $2\nu$ SM algorithm aims to reconstruct a  $t\bar{t}$  system by finding two neutrinos ( $\nu_1$  and  $\nu_2$ ) which are most likely to correspond to the neutrinos that originate from the decay of a  $t\bar{t}$  system. This algorithm can be used in our analysis to discriminate between  $tWZ$  and  $t\bar{t}Z$ , since the OSSF leptons which decay from the  $Z$  boson can be easily reconstructed and removed before inputting the event into the algorithm. The removal of the  $Z$  boson results in  $tWZ$  events that don't resemble  $t\bar{t}$  systems and  $t\bar{t}Z$  events that do resemble  $t\bar{t}$  systems, which the algorithm is designed to distinguish between. It would then be expected that the  $2\nu$ SM algorithm returns a higher score from a  $t\bar{t}Z$  event ( $\sim 1$ , i.e. it resembles a  $t\bar{t}$  event after removal of the  $Z$  boson) and a lower score from a  $tWZ$  event ( $\sim 0$ , i.e. it does not resemble a  $t\bar{t}$  event after removal of the  $Z$  boson). The first step in the  $2\nu$ SM algorithm involves stating four equations which correspond to the invariant masses of the top quark ( $m(t)$ ) and  $W$  boson ( $m(W)$ ) for the two top quark decays (i.e.  $t \rightarrow W^+b \rightarrow \ell^+\nu_\ell$ ) in a dileptonic  $t\bar{t}$  event. These can be written as,

$$(\ell_1 + \nu_1)^2 = m(W)^2 = (80.385 \text{ GeV})^2 \quad (4.3)$$

$$(\ell_1 + \nu_1 + b_{1,2})^2 = m(t)^2 = (172.5 \text{ GeV})^2 \quad (4.4)$$

$$(\ell_2 + \nu_2)^2 = m(W)^2 = (80.385 \text{ GeV})^2 \quad (4.5)$$

$$(\ell_2 + \nu_2 + b_{2,1})^2 = m(t)^2 = (172.5 \text{ GeV})^2 \quad (4.6)$$

where the subscripts indicate that these particles originate from the decay of two different top quarks in a  $t\bar{t}$  system. An assumption is made such that the mass of the neutrinos ( $\nu_1$  and  $\nu_2$ ) are exactly zero, which leaves us with 6 unknowns,  $p_{T,\nu_1}$ ,  $\phi_{\nu_1}$ ,  $\eta_{\nu_1}$ ,  $p_{T,\nu_2}$ ,  $\phi_{\nu_2}$  and  $\eta_{\nu_2}$  (components of the two neutrino's 4-vectors). The 4-vectors of the two reconstructed leptons (not from the  $Z$  boson) and the two jets with the highest DL1r  $b$ -tagger score are used as input to the algorithm. For each neutrino ( $\nu_1$  and  $\nu_2$ ), a scan over a range of possible  $\eta$  and  $\phi$  values is performed. These values were chosen to be  $\phi_{\nu_1}, \phi_{\nu_2} \in [-\pi, \pi]$  with a step size of  $\approx 0.25$  and  $\eta_{\nu_1}, \eta_{\nu_2} \in [-5, 5]$  with a step size of  $\approx 0.31$ . These ranges were chosen to maximize accuracy and minimize computation time. For each of these possible  $\eta$  and  $\phi$  values, the corresponding  $p_T$  for each neutrino is calculated ( $p_{T,\nu_1}$  and  $p_{T,\nu_2}$ ) via,

$$p_{T,\nu} = \frac{\frac{1}{2}(m(W)^2 - m(\ell)^2)}{E_\ell \cosh \eta_\nu - p_{\ell,z} \sinh \eta_\nu - p_{\ell,x} \cos \phi_\nu - p_{\ell,y} \sin \phi_\nu} \quad (4.7)$$

where  $E_\ell$  is the energy of the lepton,  $m(\ell)$  is the invariant mass of the lepton and  $p_{\ell,z}, p_{\ell,x}, p_{\ell,y}$  are the  $z$ ,  $x$  and  $y$  components of lepton's momentum. After computing  $p_{T,\nu}$  for both neutrinos for each possible  $\eta$  and  $\phi$  combination in the defined ranges, a collection of possible 4-vectors for  $\nu_1$  and  $\nu_2$  can be reconstructed.

---

<sup>1</sup>software tool and weights provided by Thomas McCarthy ( $t\bar{t}Z$  analysis group - Max Planck Institute)

Using  $\nu_1$  and  $\nu_2$ , two possible  $t\bar{t}$  systems are reconstructed,

$$t_1 = \ell_1 + b_1 + \nu_1 \text{ and } t_2 = \ell_2 + b_2 + \nu_2 \quad (4.8)$$

**OR**

$$t_1 = \ell_1 + b_2 + \nu_1 \text{ and } t_2 = \ell_2 + b_1 + \nu_2 \quad (4.9)$$

895 The  $2\nu$ SM algorithm is extremely computationally intensive. The computation time depends on the  
 896 number step size of the  $\phi$  and  $\eta$  ranges which are scanned over to reconstruct the neutrinos. For example,  
 897 consider the step sizes chosen in this analysis,  $\Delta\eta \approx 0.31$  and  $\Delta\phi \approx 0.25$  which corresponds to 32 values  
 898 for  $\eta$  and 25 values for  $\phi$ . There will be  $(32)(32)(25)(25) = 640\,000$  possible pairs of neutrinos ( $\nu_1$  and  
 899  $\nu_2$ ) to consider per event. Since two possible  $t\bar{t}$  systems (See Equations 4.8 and 4.9) are considered, this  
 900 number effectively increases to  $(2)(640000) = 128\,000$  iterations per event. In order to reduce the  
 901 number of  $t\bar{t}$  systems needed to be considered, therefore decreasing computation time, distributions of  
 902 variables from  $t\bar{t}$  events are studied to apply a veto to a possible reconstructed  $t\bar{t}$  system if the variable  
 903 in question is improbable or unlikely to be observed in a  $t\bar{t}$  event. To achieve this, an allowed range is  
 904 defined for these variables (See Figure 25 and Figure 26), and if the possible reconstructed  $t\bar{t}$  system's  
 905 corresponding value for this variable lies outside this range, it is vetoed and the algorithm continues with  
 906 the next iteration. The first variable which is considered, is the difference between average mass of the  
 907 two possible  $\ell b$  system combinations,  $\Delta\langle m(\ell b) \rangle$ . The two possible  $\ell b$  system combinations are,

$$(\ell_1 b_1) = \ell_1 + b_1 \text{ and } (\ell_2 b_2) = \ell_2 + b_2 \quad (4.10)$$

**OR**

$$(\ell_1 b_2) = \ell_1 + b_2 \text{ and } (\ell_2 b_1) = \ell_2 + b_1 \quad (4.11)$$

908  $\Delta\langle m(\ell b) \rangle$  is therefore defined as,

$$\Delta\langle m(\ell b) \rangle = \frac{1}{2} |[(m(\ell_1 b_1) + m(\ell_2 b_2)) - (m(\ell_1 b_2) + m(\ell_2 b_1))]| \quad (4.12)$$

909 The idea here is that, in events where the average masses of the two possible  $\ell b$  system combina-  
 910 tions differ greatly, the correct combination is likely to be given by the combination with the smaller  
 911 average mass. Furthermore, it was shown in Ref. [69] that reconstructed top quarks in a  $t\bar{t}$  sys-  
 912 tem that contain  $b$ -tagged jets in opposite hemispheres<sup>2</sup> ( $\eta(b_1) \times \eta(b_2) < 0$ ) of the ATLAS detector  
 913 are easier to determine the correct  $\ell b$  system combination than reconstructed  $t\bar{t}$  systems that con-  
 914 tain  $b$ -tagged jets in the same hemispheres ( $\eta(b_1) \times \eta(b_2)$ ). To illustrate this, the distributions (con-  
 915 structed from  $t\bar{t}$  events) of the probability of choosing the correct  $\ell b$  system combination, given that  
 916 the one with the minimum  $\langle m(\ell b) \rangle$  chosen ( $P(\text{Correct combination of } \ell b \text{ systems} | \text{minimum} \langle m(\ell b) \rangle)$ ) vs  
 917  $\Delta\langle m(\ell b) \rangle$  for  $b$ -tagged jets in the same and opposite hemispheres are investigated. In Figure 24, the  
 918  $P(\text{Correct combination of } \ell b \text{ systems} | \text{minimum} \langle m(\ell b) \rangle)$  vs  $\Delta\langle m(\ell b) \rangle$ , for  $b$ -tagged jets in the same and  
 919 opposite hemispheres, constructed from  $t\bar{t}$  events are shown. From Figure 24, for both cases where the  
 920  $b$ -tagged jets are in the same and opposite hemispheres, the probability for a correct  $\ell b$  system being

<sup>2</sup>The ATLAS detector can be split into two regions or *hemispheres*, defined where  $z > 0$  and  $z < 0$

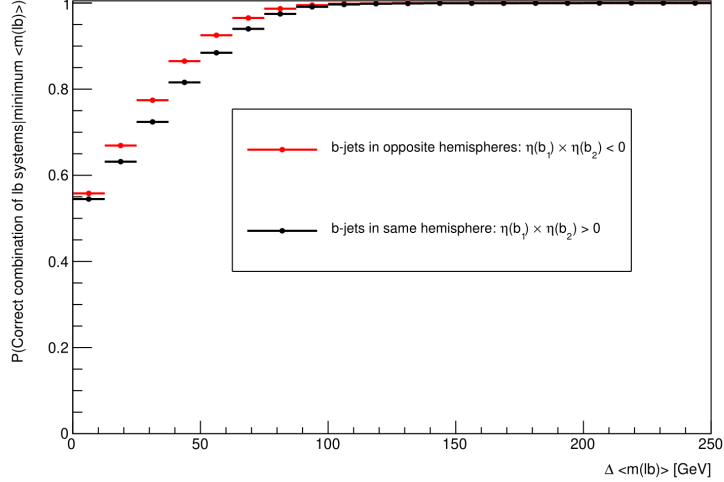


Figure 24:  $P(\text{Correct combination of } lb \text{ systems}|\text{minimum}\langle m(lb) \rangle)$  vs  $\Delta\langle m(lb) \rangle$ , for  $b$ -tagged jets in the same and opposite hemispheres, constructed from  $t\bar{t}$  events is shown. The horizontal red lines represent the distribution in the case when the two  $b$ -jets are in opposite hemispheres. The dot in the middle of the line represents the midpoint of the line. The horizontal black lines represent the distribution in the case when the two  $b$ -jets are in the same hemispheres. The dot in the middle of the line represents the midpoint of the line. The average  $m(lb)$  is shown on the x-axis. The  $P(\text{Correct combination of } lb \text{ systems}|\text{minimum}\langle m(lb) \rangle)$  is shown on the y-axis.

chosen, given that the  $lb$  system with the minimum average mass is under consideration, is an increasing function which plateaus to 1 at  $\sim 90$  GeV. One of these two distributions are used (depending on whether or not the two  $b$ -tagged jets are in the same or opposite hemispheres) to interpolate the  $P(\text{Correct combination of } lb \text{ systems}|\text{minimum}\langle m(lb) \rangle)$  from  $\Delta\langle m(lb) \rangle$ . A veto is applied to the  $lb$  combination with the maximum  $\Delta\langle m(lb) \rangle$  if  $P(\text{Correct combination of } lb \text{ systems}|\text{minimum}\langle m(lb) \rangle) > 0.8$ , indicating that there is at least an 80% certainty that the  $lb$  combination with the minimum  $\langle m(lb) \rangle$  is the correct combination. If  $P(\text{Correct combination of } lb \text{ systems}|\text{minimum}\langle m(lb) \rangle) < 0.8$ , both possible  $lb$  system combinations need to be considered. The  $\eta$  of the  $b\bar{b}\ell\ell$  system,  $\eta(b\bar{b}\ell\ell)$ , to veto improbable  $\eta(\nu_1)$  and  $\eta(\nu_2)$  values is then considered. In the same way as for  $\Delta\langle m(lb) \rangle$ , a distribution is generated to determine values  $\eta(\nu)$  which are improbable for a  $t\bar{t}$  event. In this case, a 2D histogram from simulated  $t\bar{t}$  events (dileptonic final state) at generator-level of  $\eta(\nu)$  vs  $\eta(b\bar{b}\ell\ell)$  is generated. Using this histogram, a veto region (where a  $t\bar{t}$  event is extremely unlikely to occur) is defined which contains 95% of events. A veto is applied if either possible neutrino lies within this region. In Figure 25, a heatmap of occupancy for  $\eta(\nu)$  vs  $\eta(b\bar{b}\ell\ell)$  (produced from simulated  $t\bar{t}$  events) and its corresponding veto region are shown. The final kinematic constraint which is considered is the scalar sum of lepton  $p_T$ ,  $L_T = p_T(\ell_1) + p_T(\ell_2)$ , which is used to veto certain possible neutrinos,  $\nu_1$  and  $\nu_2$ . Again, a distribution is generated to determine (and veto) improbable possible neutrinos in simulated  $t\bar{t}$  events (dilepton final state). Using the same method as described for Figure 25, a veto region is defined where a veto is applied if either possible neutrino lies within this region. In Figure 26, a heatmap of occupancy for  $\Delta R(\ell, \nu)$  vs  $L_T$  (produced from simulated  $t\bar{t}$  events) and its corresponding veto region are shown.

In order to choose the solution which best represents the two top quarks in a  $t\bar{t}$  system, the likelihood of

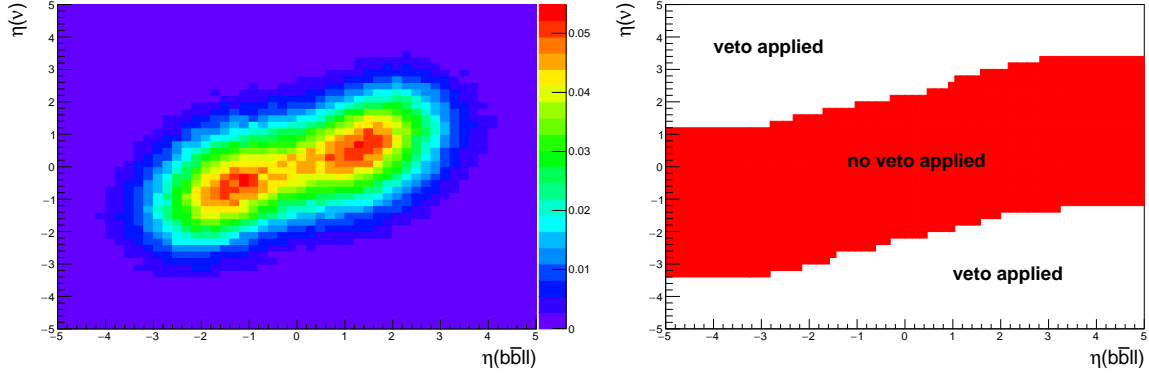


Figure 25: **Left:** Heatmap of occupancy for  $\eta(\nu)$  vs  $\eta(b\bar{b}\ell\ell)$  produced from simulated  $t\bar{t}$  events (dileptonic final state) at generator-level is shown.  $\eta$  of the  $b\bar{b}\ell\ell$  system is shown on the x-axis.  $\eta$  of the neutrino is shown on the y-axis. The colourbar on the right represents the fraction of events in the phase space. **Right:** The regions where vetoes are applied for the  $\eta(b_1 b_2 \ell_1 \ell_2)$  constraint is shown.  $\eta$  of the  $b\bar{b}\ell\ell$  system is shown on the x-axis.  $\eta$  of the neutrino is shown on the y-axis. The red band shows the region where the neutrino would not be vetoed. The white areas (above and below the red band) are regions where the neutrino is vetoed.

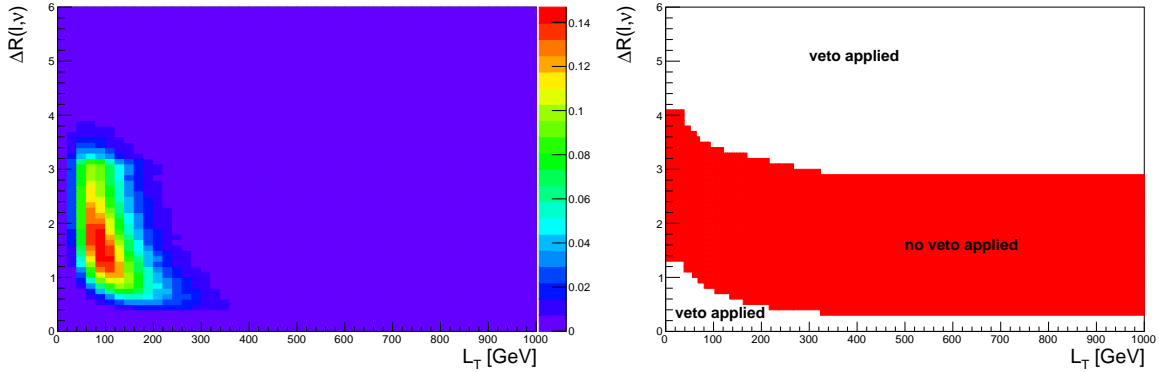
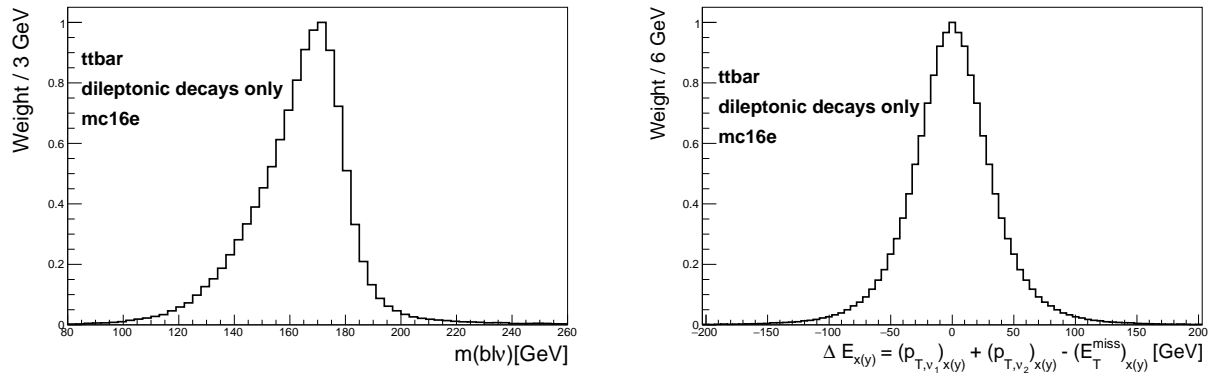


Figure 26: **Left:** A heatmap of occupancy for  $\Delta R(\ell, \nu)$  vs  $L_T$  produced from simulated  $t\bar{t}$  events (dileptonic final state) at generator-level is shown.  $\Delta R$  between leptons and neutrinos is shown on the x-axis.  $L_T$  (scalar sum of lepton  $p_T$ ) is shown on the y-axis. The colourbar on the right represents the fraction of events in the phase space. **Right:** The regions where vetoes are applied for the  $L_T$  constraint is shown.  $\Delta R$  between leptons and neutrinos is shown on the x-axis.  $L_T$  (scalar sum of lepton  $p_T$ ) is shown on the y-axis. The red band shows the region where the neutrino would not be vetoed. The white areas (above and below the red band) are regions where the neutrino is vetoed.

each solution is evaluated in the SM  $t\bar{t}$  hypothesis. This is performed using the product of probabilities derived from certain distributions of variables from simulated  $t\bar{t}$  events. The events in these distributions are obtained from an ATLAS simulation of generated  $t\bar{t}$  events in the dileptonic final state. A normalised distribution of the mass of reconstructed top quarks,  $m_{b\ell\nu}$ , from a  $t\bar{t}$  sample is generated to determine the probabilities  $P_{m_{t_1}}$  and  $P_{m_{t_2}}$  which correspond to the likelihood of the reconstructed top quarks under the SM  $t\bar{t}$  hypothesis. The distribution is generated from reco-level leptons, generator-level neutrinos and reco-level jets matched in  $\Delta R$  to generator-level  $b$ -quarks, therefore only filling the distribution with correct detector-level objects. For both reconstructed top quarks,  $m(b\ell\nu)$  is calculated and interpolated (i.e.

estimate the value of the distribution for some value of the independent variable), via linear interpolation based on the two nearest bin centres, against the  $m_{b\ell\nu}$  distribution which returns a weight value from 0 to 1, with higher values corresponding to a reconstructed top quark which has a mass close to that of a top quark from a  $t\bar{t}$  system. This interpolation is done for both reconstructed top quarks,  $t_1$  and  $t_2$ , corresponding to probabilities  $P_{m_{t_1}}$  and  $P_{m_{t_2}}$ . A similar method is used to determine  $P_{\Delta E_x}$  and  $P_{\Delta E_y}$ , which corresponds to the likelihood of the reconstructed top quarks under the SM  $t\bar{t}$  hypothesis. In this case, a weight distribution of  $\Delta E_x = (p_{T,\nu_1})_x + (p_{T,\nu_2})_x - (E_T^{\text{miss}})_x$  based off simulated  $t\bar{t}$  events is generated. In particular, this distribution is generated using reco-level  $E_T^{\text{miss}}$  and generator-level neutrinos. The use of this distribution lies under the assumption that neutrinos are the dominant source of  $E_T^{\text{miss}}$ , and therefore,  $(E_T^{\text{miss}})_x \approx (p_{T,\nu_1})_x + (p_{T,\nu_2})_x$  and  $(E_T^{\text{miss}})_y \approx (p_{T,\nu_1})_y + (p_{T,\nu_2})_y$ . This distribution is then used to interpolate the value of  $\Delta E_x$  and  $\Delta E_y$  from our reconstructed neutrinos. This returns a weight value from 0 to 1, with higher values corresponding to  $\Delta E_x$  and  $\Delta E_y$  (and in turn our reconstructed neutrino's  $p_T$ ) closer to those observed in a  $t\bar{t}$  event. It is expected that the  $\Delta E_x$  and  $\Delta E_y$  distributions have the same shapes, therefore only one is needed to be generated. In this case the the  $\Delta E_x$  distribution was chosen. In Figure 27, the  $m_{b\ell\nu}$  and  $\Delta E_x$  distributions (generated from simulated  $t\bar{t}$  events) are shown.

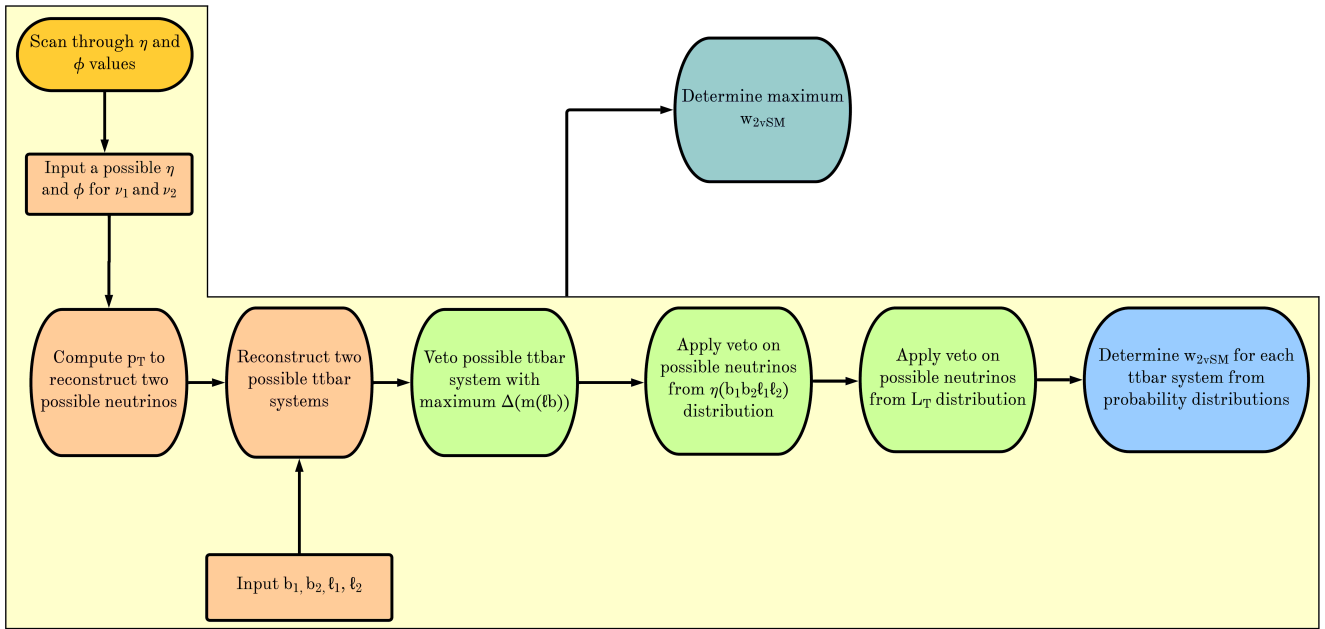


**Figure 27:** **Left:**  $m_{b\ell\nu}$  distribution generated from simulated  $t\bar{t}$  events, used to calculate  $P_{m_{t_1}}$  and  $P_{m_{t_2}}$  is shown. The  $m_{b\ell\nu}$  distribution is shown by the black lined histogram. The mass of the  $b\ell\nu$  system is shown on the x-axis. The corresponding weight of the  $m_{b\ell\nu}$  distribution is shown on the y-axis. **Right:**  $\Delta E_x$  distribution generated from simulated  $t\bar{t}$  events, used to calculate  $P_{\Delta E_x}$  and  $P_{\Delta E_y}$  is shown. The  $\Delta E_x$  distribution is shown by the black lined histogram.  $\Delta E_x$  is shown on the x-axis. The corresponding weight of  $\Delta E_x$  distribution is shown on the y-axis.

A final weight,  $w_{2\nu SM} \in [0, 1]$ , is then calculated by multiplying the four probabilities ( $P_{m_{t_1}}$ ,  $P_{m_{t_2}}$ ,  $P_{\Delta E_x}$  and  $P_{\Delta E_y}$ ) described above. This final weight represents a total probability of the reconstructed top quarks under the SM  $t\bar{t}$  hypothesis, and can be written as,

$$w_{2\nu SM} = P_{m_{t_1}} \times P_{m_{t_2}} \times P_{\Delta E_x} \times P_{\Delta E_y} \quad (4.13)$$

The  $w_{2\nu SM}$  is calculated for each pair of reconstructed neutrinos (or reconstructed  $t\bar{t}$  systems), with the maximum value being chosen as the final value for the event. In Figure 28, a flow chart that summarises the steps taken to calculate the  $w_{2\nu SM}$  for an event is shown.

Figure 28: A flow chart that summarises the steps taken to calculate the  $w_{2\nu SM}$  for an event is shown.

### 4.7.2 Boosted Decision Trees

Machine Learning techniques can be used to build multivariate discriminators that exploits information from many discriminators to form one discriminator with more discriminating power than the combination of those which it is built from. A BDT is a Machine Learning technique which classifies data in a dataset into different categories by iteratively applying binary cuts on features of the data (input variables, in the context of this analysis) [101]. The method in which a BDT combines many discriminators to build a single discriminator is called *boosting*. In boosting, weak discriminators are sequentially combined, where each classifier iteration is fitted to the difference between the observed and predicted values (residuals) of the training set from the previous step, such that the classifier performance improves [56]. A few concepts related to Machine Learning and BDTs that are used in this analysis, are described briefly in the following text. Performance metrics can be used to evaluate how well a classifier performs in a classification problem [74]. A performance metric used extensively in this analysis is the *accuracy* of a classifier. The accuracy is defined as the percentage of correct predictions for the test dataset (accuracy =  $\frac{\text{correct number of predictions}}{\text{total number of predictions}}$ ). Machine Learning classifiers can be susceptible to learning a training dataset too well, in such a way as to negatively affect its performance on unseen data. This is known as *over-training*. Over-training occurs when noise or random fluctuations in the training dataset are learnt by the classifier [28]. Cross Validation [77] is a procedure used to evaluate a Machine Learning classifier. Cross validation gives an estimate on how the classifier is expected to perform on unseen data and it can be useful tool to protect against over-training. In this analysis we use a type of cross validation called, *k-fold* cross validation. In k-fold cross validation, the training dataset is randomly split up into k subsets, or folds, of approximately equal size. A fold is defined as a test dataset and the remaining  $k-1$  folds are used to train the classifier. The classifier is then evaluated on the test set and a performance metric (or multiple) is evaluated. This procedure is performed once on each fold. Hyper-parameters are user-defined

parameters of a classifier that are govern the entire training process. Typical examples of hyper-parameters include the learning rate, the number of discriminators and the type of loss function to be minimised. The learning rate determines the step size at each iteration in determining the minimum of the loss function. Hyper-parameter optimisation is a process which aims to determine the best hyper-parameters for a classifier, based off some performance metric. In this analysis hyper-parameter optimisation is performed using a *grid search*. In a grid search, a user-defined list of hyper-parameter values are chosen for each hyper-parameter that one aims to optimise. The classifier is then trained using each permutation of hyper-parameters and determines the set of hyper-parameters in which the performance metric is maximised. BDTs are chosen to be used in this analysis, since they are not prone to over-training and perform well with minimal optimisation or tweaking of the hyper-parameters. A multi-layered sequential neutral network was tried, however, it was out-performed by a BDT. More specifically, Scikit-Learn’s `GradientBoostingClassifier` [86] was used.

#### 4.7.3 Object-level BDT

The object-level BDT was trained on an  $t\bar{t}$  sample simulated using the same generator, parton shower and to the same order of QCD as the  $t\bar{t}$  sample described in Section 4.1.2 but with an orthogonal baseline selection of exactly 1 tight lepton with  $p_T > 28$  GeV such that there is no overlap between this sample and the nominal  $t\bar{t}$  sample used in the analysis. Additionally, jets in this sample are required to have  $p_T > 20$  GeV. Jets are identified as  $b$ -tagged jets by the 77% DL1r working point. These baseline selections were chosen to mimic those used in the event selection of the analysis (outlined in Table 6). The leptons and  $b$ -jets used for training the object-level BDT are required to pass the aforementioned baseline selections. This  $t\bar{t}$  sample was utilised in training the BDT to avoid using a subset of events from the MC samples used in the rest of the analysis, therefore maximizing the amount of generated events available to use in other parts of the analysis. The signal class is defined to consist of reconstructed  $\ell b$  systems (defined as the sum of the 4-vectors of a lepton and a  $b$ -tagged jet) originating from top quarks which are well matched to their truth counterparts. All possible combinations of  $\ell$  and  $b$ -tagged jets are selected from the events. In particular, it is required that  $\Delta R$  between the reconstructed and truth  $\ell b$  system is less than 0.05. An additional requirement is implemented such that the reconstructed lepton and the truth top quark have charges with the same sign (since  $t \rightarrow b\ell^+\bar{\nu}_\ell$  and  $\bar{t} \rightarrow \bar{b}\ell^-\nu_\ell$ ). The background class is defined to consist of all reconstructed  $\ell b$  systems which fail to pass the criteria for  $\ell b$  systems which are labelled as signal. These definitions for the signal and background classes ensure that the signal class consists of mostly  $\ell b$  systems originating from top quarks and the background class consists of mostly  $\ell b$  systems which do not originate from top quarks. The input variables chosen to be used in the object-level BDT are related to measurable quantities of  $\ell b$  systems. The optimum values for the hyper-parameters used were determined via the use of a grid-search (See Section 4.7.2) that determined the set of hyper-parameters which maximized the mean accuracy (based off 5 fold kfold cross-validation). After hyper-parameter optimisation, the mean accuracy of each fold increased from 0.76 to 0.77 ( $\sim 1\%$  increase). Input variables can be assigned a score called *variable importance*, based on their usefulness on predicting a target variable (in this case, a signal or background event). The variable importance for any given input variable was obtained by computing the mean accuracy of the classifier, removing the input variable from training, retraining the classifier and computing the mean accuracy of this new classifier. The difference between

mean accuracies of the unaltered classifier and the retrained classifier (after removal of the input variable) gives us the variable importance of the given input variable. This method returns positive values for input variables which increase the mean accuracy of the classifier and negative values for input variables which decrease the mean accuracy of the classifier. Input variables with negative variable importances were completely removed from training. In Table 9, the input variables used for training the object-level BDT are shown. In Figure 29, normalised distributions of the input variables used in the object-level BDT, for

Input Variable	Description	Variable Importance
$m(\ell b)$	Invariant mass of the $\ell b$ system	0.0025
$p_T(\ell b)$	$p_T$ of the $\ell b$ system	0.0005
$\Delta\eta(\ell, b)$	$\Delta\eta$ between the $\ell$ and $b$ -tagged jet	0.0003
$\Delta\phi(\ell, b)$	$\Delta\phi$ between the $\ell$ and $b$ -tagged jet	0.0003
$\Delta R(\ell, b)$	$\Delta R$ between the $\ell$ and $b$ -tagged jet	0.0001

Table 9: A list of the input variables used in the object-level BDT, ordered by variable importance (descending, top to bottom) is shown.

1039

the signal and background classes, are shown. The input variables used in the object-level BDT show a

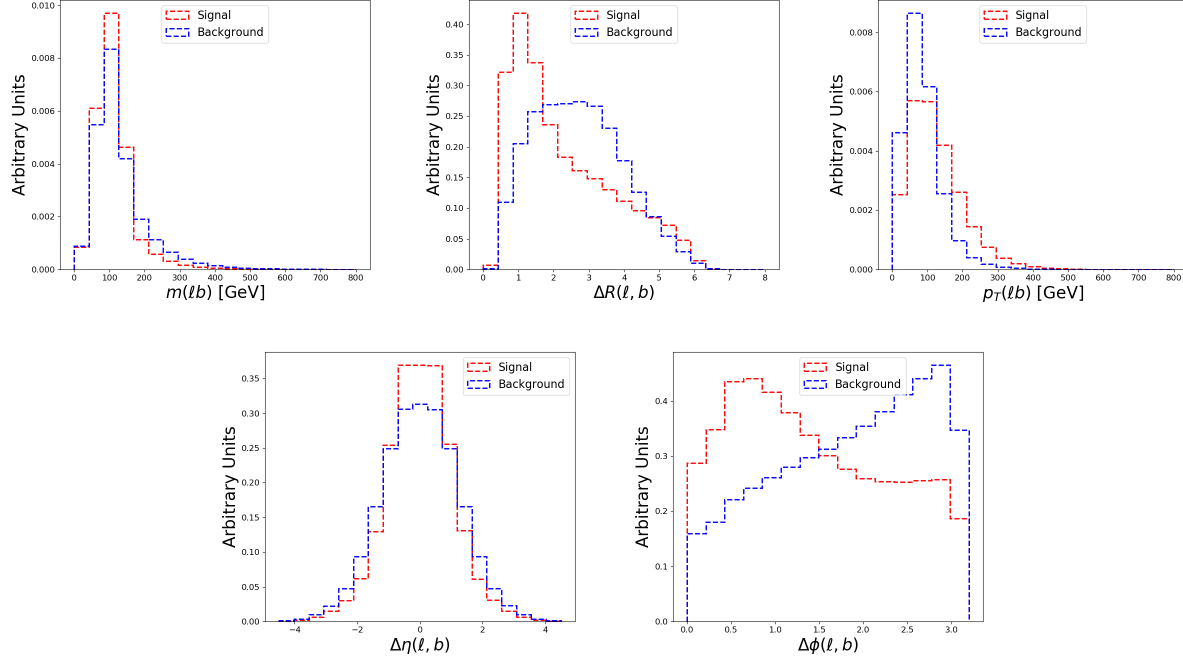


Figure 29: Normalised distributions of the input variables used in the object-level BDT (ordered from top left to bottom right via decreasing variable importance), for the signal and background classes are shown. **From top left to bottom right:** The invariant mass of the  $\ell b$  system,  $\Delta R$  between the  $\ell$  and  $b$ -tagged jet, the  $p_T$  of the  $\ell b$  system,  $\Delta\eta$  between the  $\ell$  and  $b$ -tagged jet, and  $\Delta\phi$  between the  $\ell$  and  $b$ -tagged jet. The red and blue dotted lined histograms represent the signal and background classes events (from the training set), respectively. These histograms are normalised to an area of 1. The input variable used in training is shown on the x-axis. The y-axis shows the relative number of events for the signal and background classes in arbitrary units.

1040

1041 clear distinction between signal and background  $\ell b$  systems. The modelling of the input variables used  
 1042 in the object-level BDT can be checked by studying the agreement between data and simulation in the  
 1043  $t\bar{t}Z$  CR. In Figure 30, MC predictions for the input variables used in the object-level BDT in the  $t\bar{t}Z$  CR  
 are shown. Overall, there is good agreement between data and simulation for the input variables used in

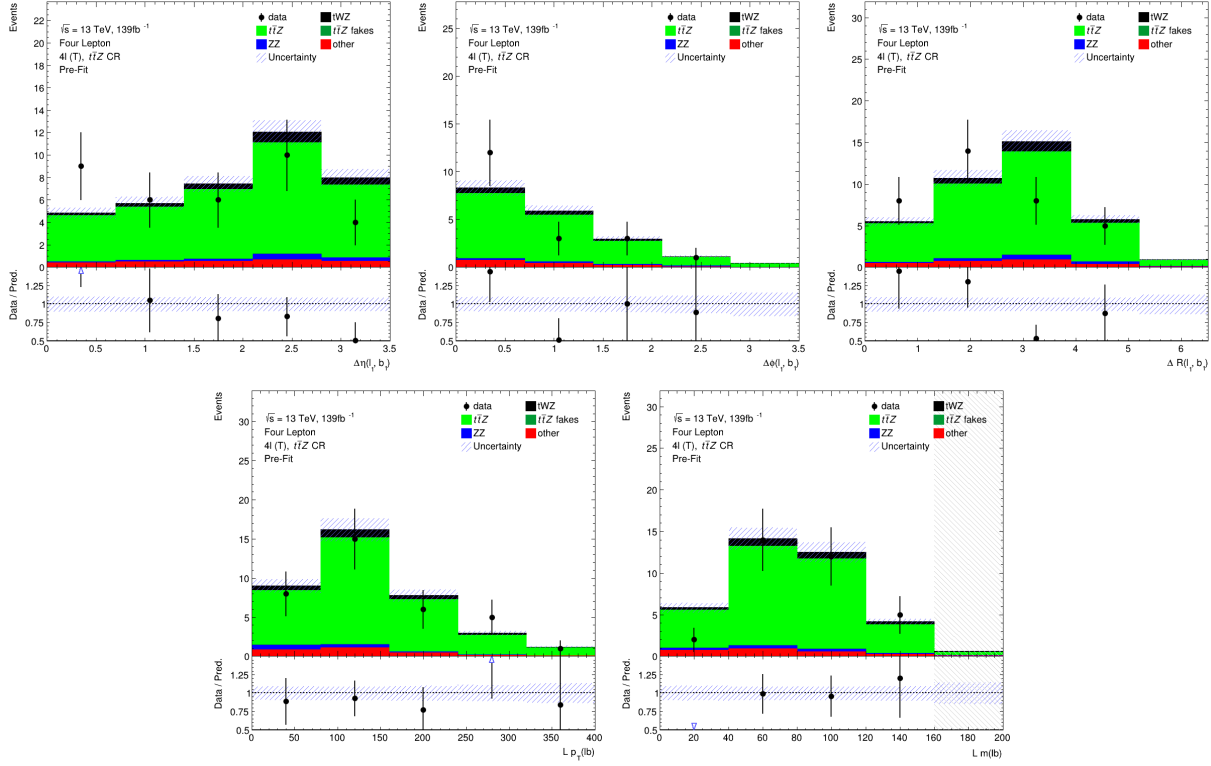


Figure 30: The expected number of events for the object-level BDT input variables (ordered from top left to bottom right via decreasing variable importance), in the  $t\bar{t}Z$  CR, are shown. **From top left to bottom right:**  $\Delta\eta$  between the lepton and  $b$ -jet of the leading  $\ell b$  system,  $\Delta\phi$  between the lepton and  $b$ -jet of the leading  $\ell b$  system,  $\Delta R$  between the lepton and  $b$ -jet of the leading  $\ell b$  system,  $p_T$  of the leading  $\ell b$  system, and the mass of the leading  $\ell b$  system. The data is given by the black points and the MC predictions for each process are given by the filled histograms. The vertical lines on the data points represent the statistical uncertainty in the data and the blue diagonally-lined bands represent the total (statistical and systematic added in quadrature) uncertainty. The lower panel in each plot shows the ratios of the data to the theoretical predictions. Bins with  $\frac{\text{signal}}{\text{background}}$  greater than 0.1 are kept blinded. Blinded bins are shaded with black diagonal lines and their data points are omitted.

1044 the object-level BDT, in the  $t\bar{t}Z$  CR. This suggests that the input variables used in the object-level BDT  
 1045 are well-modelled and are reasonable to include as inputs to the object-level BDT. A final check can be  
 1046 done to study the similarity of the  $\ell b$  systems present in the  $t\bar{t}$  sample which are used for training the  
 1047 object-level BDT, and the  $\ell b$  systems which are aimed to be identified using the object-level BDT. More  
 1048 specifically, the study is done to ensure that the modelling of the  $\ell b$  systems in the  $t\bar{t}$  sample are sufficiently  
 1049 similar to those in the  $tWZ$  and  $t\bar{t}Z$  samples (see Table 3). This is done to understand how well the  
 1050 BDT (trained on  $\ell b$  systems in the  $t\bar{t}$  sample) generalises to classifying  $\ell b$  systems in the analysis ( $tWZ$   
 1051 and  $t\bar{t}Z$  samples). In Figure 31, normalised distributions of the input variables used in the object-level  
 1052 BDT for the  $t\bar{t}$ ,  $tWZ$  and  $t\bar{t}Z$  samples, are shown. The distributions of the signal events from all three  
 1053

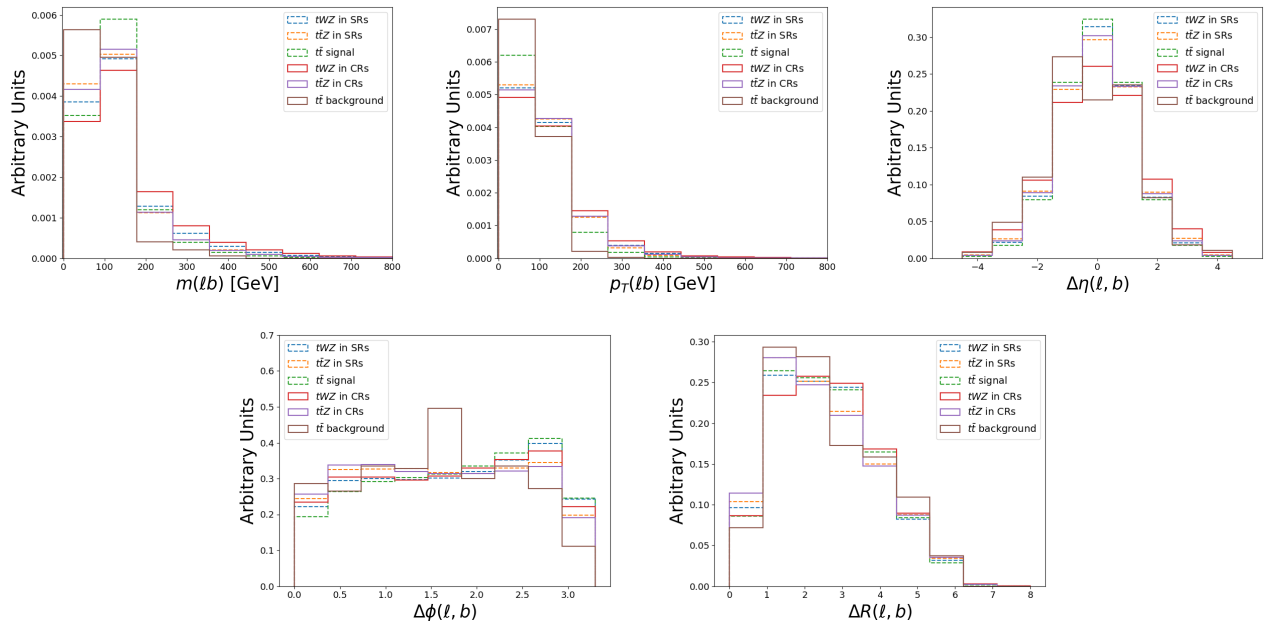


Figure 31: Normalised distributions of the input variables (ordered from top left to bottom right via decreasing variable importance) used in the object-level BDT for the  $t\bar{t}$ ,  $tWZ$  and  $ttZ$  samples, are shown. **From top left to bottom right:** The invariant mass of the  $\ell b$  system,  $\Delta R$  between the  $\ell$  and  $b$ -tagged jet, the  $p_T$  of the  $\ell b$  system,  $\Delta\eta$  between the  $\ell$  and  $b$ -tagged jet,  $\Delta\phi$  between the  $\ell$  and  $b$ -tagged jet. The blue and orange dotted lined histograms represent events from the  $tWZ$  and  $ttZ$  samples in the SRs, respectively. The red and purple solid lined histograms represent events from the  $tWZ$  and  $ttZ$  samples in the CRs, respectively. The dotted lined green histograms and the solid lined brown histograms represents signal and background events from the  $t\bar{t}$  sample, respectively. These histograms are normalised to an area of 1. The input variable used in training is shown on the x-axis. The y-axis shows the relative number of events in arbitrary units.

processes for all of the input variables show minimal deviation between one another. This suggests that the  $\ell b$  systems, that are classified as signal in training, are similar to those used in the analysis and are therefore sufficient to include in training. There are substantially larger deviations in the distributions of the background events (compared to the signal events) from all three processes for all of the input variables. The deviations are especially noticeable in the  $\Delta\phi(\ell, b)$  distribution, with a large excess of  $t\bar{t}$  background events over the remaining processes. These deviations suggest that the use of the  $t\bar{t}$  sample in training the object-level BDT may be sub-optimal in classifying  $\ell b$  systems which do not originate from top quarks. However, it still represents the best option available, since our other options involve utilising of a subset of generated events used in the other parts of the analysis. This would result in a smaller number of generated events used in the background prediction, leading to larger MC statistical uncertainties. In Table 10, the hyper-parameters used in the object-level BDT is shown. The number of events used in training for the signal and background classes were 49871 and 384152 respectively. Imbalanced datasets can cause ML classifiers to ignore small classes while concentrating on classifying large classes more accurately, which may result in the trained BDT performing sub-optimally. In order to correct this dataset imbalance, it is ensured that the relative weighting of each event is such that the sum of the signal weights is equal to the sum of the background weights. In order to avoid over-training,

Hyper-parameter	Value	Description
loss	deviance	The loss function to be optimised
criterion	friedman_mse	The function used to measure the quality of a split
n_estimators	200	The number of boosting stages to perform
learning_rate	0.1	The step size at each iteration during optimisation
max_depth	6	The maximum depth of the individual regression estimators
min_samples_split	2	The minimum number of samples (events) required to split an internal node
min_samples_leaf	1	The minimum number of samples (events) required to be at a leaf node
validation_fraction	0.1	The proportion of training data to set aside as validation set for early stopping
n_iter_no_change	20	Training terminates when the validation score does not improve in all of the previous

Table 10: A list of the hyper-parameters used in the object-level BDT is shown. Hyper-parameters not listed in this table use the default values as stated in the Scikit-learn Documentation[87].

1070 the BDT outputs to the training set and a test set can be studied. If over-training occurs, the BDT will  
 1071 fit the data in the training set too closely, resulting in the BDT outputs of the training and test sets to  
 1072 differ. In Figure 32 the normalised histograms of the training and test sets (extracted from fold 5 from a  
 1073 5 fold kfold cross validation) for signal and background is shown.

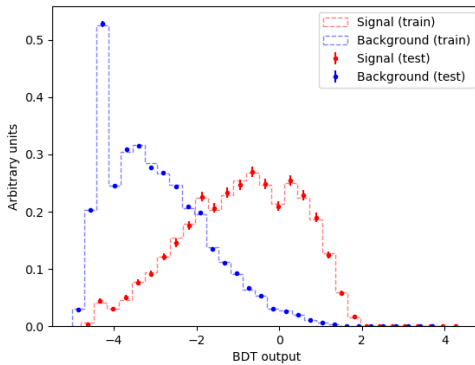


Figure 32: Normalised histograms of the object-level BDT discriminator output from the signal and background classes for the training and test sets from the 5th fold in a 5 fold kfold cross validation is shown. The output of the object-level BDT is shown on the x-axis and the relative number of events in arbitrary units, is shown on the y-axis. The training set for the signal class is shown by the red dotted histogram. The test set for the signal class is shown by the red points, with the total uncertainty represented by the vertical error bars. The training set for the background class is shown by the blue dotted histogram. The test set for the background class is shown by the blue points, with the total uncertainty represented by the vertical error bars.

1074 The shapes of the training and test sets for both signal and background agree within uncertainties in  
 1075 the vast majority of bins. This is a good indicator that no over-training occurred, since it indicates  
 1076 that statistical fluctuations (or noise) present in the training set was not learnt during training. Another  
 1077 over-training check is performed using 5 fold kfold cross validation. To ensure that the BDT is not over-  
 1078 training, it is ensured that the variance of the mean accuracy of each folds' test set in cross validation  
 1079 is substantially small. This tells us that the BDT does not perform better on different subsets of the  
 1080 training set over another and it is therefore not prone to learning statistical fluctuations of a dataset  
 1081 in training, which would result in the BDT not being able to generalise well to unseen datasets. For  
 1082 the object-level BDT, a variance of  $3.24 \times 10^{-7}$  was calculated for the mean accuracies of each folds' test

set in cross validation. This small variance therefore provides further evidence that no over-training occurred. The output of the object-level BDT is converted to an event-level variable to be used in the event-level BDT. This variable,  $\text{BDTScore}(\frac{\text{Best}}{\text{2nd Best}})$ , is defined as the ratios of the score of the best scoring  $\ell b$  system to the 2nd best scoring  $\ell b$  system. The 2nd best scoring  $\ell b$  system in a  $tWZ$  event is expected to be low, since there is only one  $\ell b$  system originating from a top quark. Thus  $\text{BDTScore}(\frac{\text{Best}}{\text{2nd Best}})$  is expected to be large for  $tWZ$  events and closer to one for  $t\bar{t}Z$  events, therefore providing discrimination between  $tWZ$  and  $t\bar{t}Z$ . In Figure 33, normalised distributions of the signal and total background of the  $\text{BDTScore}(\frac{\text{Best}}{\text{2nd Best}})$  variable in the  $tWZ$  OF SR,  $tWZ$  SF SR and  $t\bar{t}Z$  CR are shown. The amount of

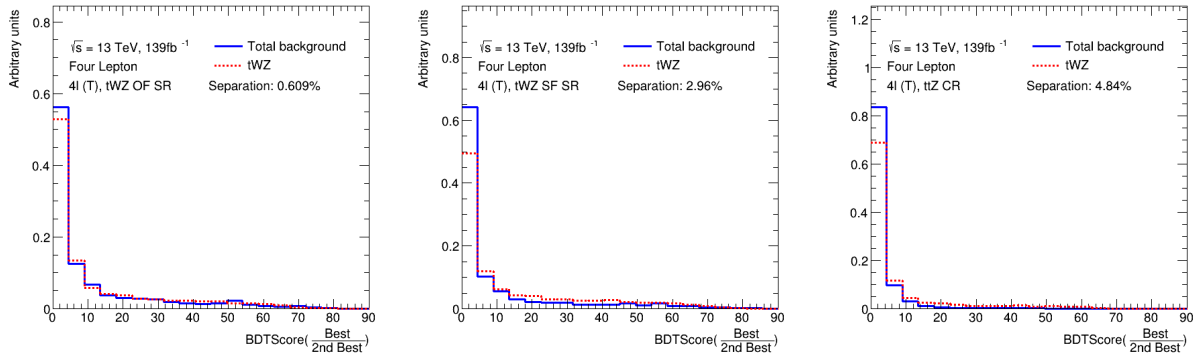


Figure 33: Normalised distributions of the signal and total background of the  $\text{BDTScore}(\frac{\text{Best}}{\text{2nd Best}})$  variable in the  $tWZ$  OF SR,  $tWZ$  SF SR and  $t\bar{t}Z$  CR (left to right) are shown. The dotted red and solid blue lines represent the distributions of the signal and total background events respectively. These histograms are normalised to an area of 1. The x-axis shows the  $\text{BDTScore}(\frac{\text{Best}}{\text{2nd Best}})$  and the y-axis show the relative number of events in arbitrary units.

discrimination can be quantified by the separation metric, which gives the percentage of the total area of the distributions which do not overlap. A value of 1 indicates that the distributions are fully separated (no overlap) and a value of 0 indicates that the distributions have no separation (fully overlapped). The separation between signal and background for  $\text{BDTScore}(\frac{\text{Best}}{\text{2nd Best}})$  in the  $tWZ$  OF SR,  $tWZ$  SF SR and  $t\bar{t}Z$  CR are 0.609%, 2.96% and 4.84% respectively. The larger separation in the  $t\bar{t}Z$  CR, compared to the  $tWZ$  SRs, can be explained since there is a larger proportion of  $t\bar{t}Z$  events (events with two  $\ell b$  systems) in this region, due to the baseline selection requirement of exactly two  $b$ -tagged jets. In a similar way, the smaller separation in the two  $tWZ$  SRs can be explained by the tighter selection on the number of  $b$ -tagged jets (exactly one) leading to regions which are enriched in only one  $\ell b$  system which originates from a top quark. Using the  $\text{BDTScore}(\frac{\text{Best}}{\text{2nd Best}})$  variable in training in the event-level BDT (see Section 4.7.4) improves the mean accuracy of the BDT. This tells us that the event-level BDT is taking advantage of the discrimination between signal and background present in the  $\text{BDTScore}(\frac{\text{Best}}{\text{2nd Best}})$  variable. In an attempt to optimise the performance of the object-level BDT, signal events which are pure in  $\ell b$  systems originating from top quarks are targeted for training the BDT. Similarly, background events which are pure in  $\ell b$  systems which do not originate from top quarks are targeted for training the BDT. This is done by studying the distribution of  $\Delta R$  between the reconstructed  $\ell b$  system and the truth  $\ell b$  system ( $\Delta R((lb)_{reco}, (lb)_{truth})$ ), and excluding  $\ell b$  systems from training which are moderately matched in  $\Delta R$  to their truth counterparts, leaving well matched  $\ell b$  systems being labelled as signal

and badly matched  $\ell b$  systems labelled as background. The  $\Delta R$  range where  $\ell b$  systems are excluded from training is referred to as the exclusion region. In Figure 34, the distribution of  $\Delta R$  between the reconstructed  $\ell b$  system and the truth  $\ell b$  system ( $\Delta R((lb)_{reco}, (lb)_{truth})$ ) in the  $t\bar{t}$  sample, along with the exclusion region, is shown. A large number of reconstructed  $\ell b$  systems have  $\Delta R((lb)_{reco}, (lb)_{truth})$  at

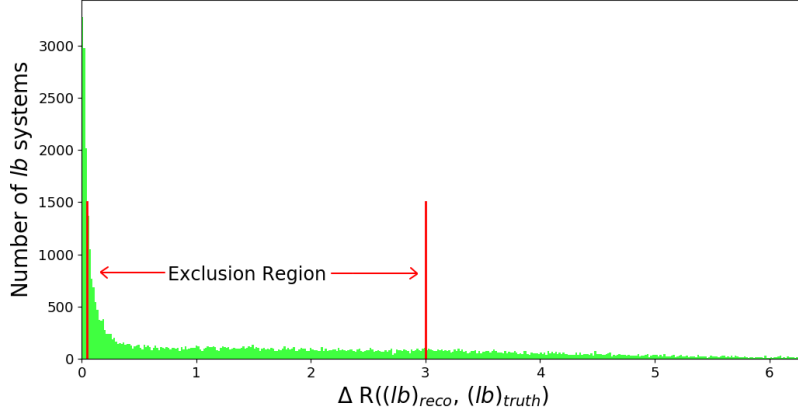


Figure 34: The distribution of  $\Delta R$  between the reconstructed  $\ell b$  system and the truth  $\ell b$  system ( $\Delta R((lb)_{reco}, (lb)_{truth})$ ) in the  $t\bar{t}$  sample, along with the exclusion region, is shown. The  $\Delta R$  distribution is shown in green.  $\Delta R$  between the reconstructed  $\ell b$  system and the truth  $\ell b$  system ( $\Delta R((lb)_{reco}, (lb)_{truth})$ ) is shown on the x-axis. The number of  $\ell b$  systems is shown on the y-axis. The exclusion region is shown between the vertical red lines situated at  $\Delta R((lb)_{reco}, (lb)_{truth}) = 0.05$  and  $\Delta R((lb)_{reco}, (lb)_{truth}) = 3.0$ . Reconstructed  $\ell b$  systems with  $\Delta R((lb)_{reco}, (lb)_{truth}) \leq 0.05$  are labelled as signal and reconstructed  $\ell b$  systems with  $\Delta R((lb)_{reco}, (lb)_{truth}) \geq 3.0$  are labelled as background.

values near 0. These are matched (in  $\Delta R$ ) extremely well to truth  $\ell b$  systems originating from top quarks. Therefore our exclusion region is defined to be between  $0.05 < \Delta R((lb)_{reco}, (lb)_{truth}) < 3.0$ , such that all reconstructed  $\ell b$  systems with  $\Delta R((lb)_{reco}, (lb)_{truth}) \leq 0.05$  are labelled as signal and reconstructed  $\ell b$  systems with  $\Delta R((lb)_{reco}, (lb)_{truth}) \geq 3.0$  are labelled as background. All reconstructed  $\ell b$  systems with  $0.05 < \Delta R((lb)_{reco}, (lb)_{truth}) < 3.0$  are excluded from training. The performance of the object-level BDT with and without the exclusion region can be compared by studying the discrimination between signal and background events in the  $BDTScore(\frac{\text{Best}}{\text{2nd Best}})$  variable (object-level output converted to an event-level variable to be used in the event-level BDT) for both object-level BDTs. In Figure 35, normalised distributions of  $BDTScore(\frac{\text{Best}}{\text{2nd Best}})$  using the object-level BDT without the exclusion region (see Figure 34) for the  $tWZ$  OF SR,  $tWZ$  SF SR and  $t\bar{t}Z$  CR are shown. The separation metrics can be compared between the  $BDTScore(\frac{\text{Best}}{\text{2nd Best}})$  variable in the  $tWZ$  OF SR,  $tWZ$  SF SR and  $t\bar{t}Z$  CR for the object-level BDT with (Figure 33) and without (Figure 35) the exclusion region by taking the absolute difference between the two values in each region. The differences are 0.31%, 0.37% and 0.36% for the  $tWZ$  OF SR,  $tWZ$  SF SR and  $t\bar{t}Z$  CR, respectively. These differences are minimal and the object-level BDT with the exclusion region outperforms the object-level BDT without the exclusion region in the  $tWZ$  SF SR. Due to the small differences in performance between the two BDTs, the BDT with the exclusion region was chosen to be kept.

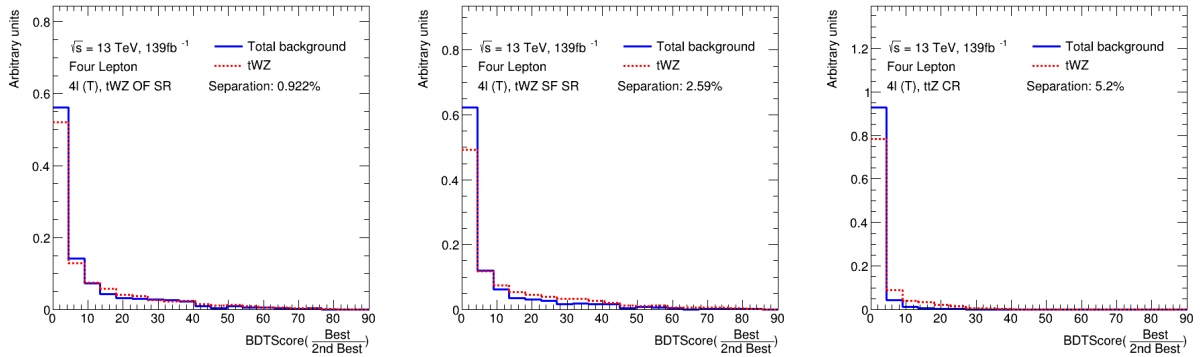


Figure 35: Normalised distributions of  $\text{BDTScore}(\frac{\text{Best}}{\text{2nd Best}})$  using the object-level BDT without the exclusion region (see Figure 34) for the  $tWZ$  OF SR,  $tWZ$  SF SR and  $t\bar{t}Z$  CR (left to right) are shown. The dotted red and solid blue lines represent the distributions of the signal and total background events respectively. These histograms are normalised to an area of 1. The x-axis shows the  $\text{BDTScore}(\frac{\text{Best}}{\text{2nd Best}})$  and the y-axis show the relative number of events in arbitrary units.

#### 1130 4.7.4 Event-level BDT

1131 The event-level BDT is used to distinguish between signal and its major background events,  $t\bar{t}Z$  and  
 1132  $ZZ$ . The key difference between the object-level BDT and the event-level BDT is that while the former  
 1133 exploits information associated with  $\ell b$  systems and thus distinguishes between  $\ell b$  systems, the event-level  
 1134 BDT exploits information based on the entirety of the event and thus distinguishes between events. The  
 1135 event-level BDT was trained on 50% of the  $tWZ$  MC sample's events for the signal class and similarly,  
 1136 50% of the  $t\bar{t}Z$  and  $ZZ$  MC sample's events were used for the background class. The input variables used  
 1137 to train the BDT are chosen on the basis that they are somewhat uncorrelated from one another and  
 1138 show some discrimination between  $tWZ$  and  $t\bar{t}Z$ . Similarly to the object-level BDT, the optimum values  
 1139 for the hyper-parameters used were determined via a grid-search (See Section 4.7.2) that determined the  
 1140 set of hyper-parameters which maximized the mean accuracy (based off 5 fold kfold cross-validation).  
 1141 After hyper-parameter optimisation, the mean accuracy of each fold (determined from 5 fold kfold cross  
 1142 validation) increased from 0.72 to 0.74 ( $\sim 3\%$  increase). The variable importance of each input variable  
 1143 was computed in the same way as described for the object-level BDT (See Section 4.7.3). In Table 11, the  
 input variables used for training the event-level BDT are shown. In Figure 36, normalised distributions

Input Variable	Description	Variable Importance
$2\nu\text{SM}$	Maximum weight from the $2\nu\text{SM}$ algorithm (See Section 4.7.1)	0.029
$HT$	Scalar sum of jet $p_T$	0.016
$LT$	Scalar sum of lepton $p_T$	0.011
$\sum p_T(b-jet)$	Scalar sum of $b$ -tagged jet $p_T$	0.006
$\text{BDTScore}(\frac{\text{Best}}{\text{2nd Best}})$	Ratio of the best to the 2nd best scoring $\ell b$ system from the object-level BDT	0.006
$\Delta\eta(\ell_{1,\text{non-}Z}, \ell_{2,\text{non-}Z})$	$\Delta\eta$ between the two leptons, not coming from a $Z$ candidate	0.005

Table 11: A list of the input variables used in the event-level BDT, ordered by variable importance (descending, top to bottom) is shown.

1144  
 1145 of the input variables used in the event-level BDT, for the signal and background classes are shown.  
 1146 The input variables used in the event-level BDT show a clear distinction between signal and background

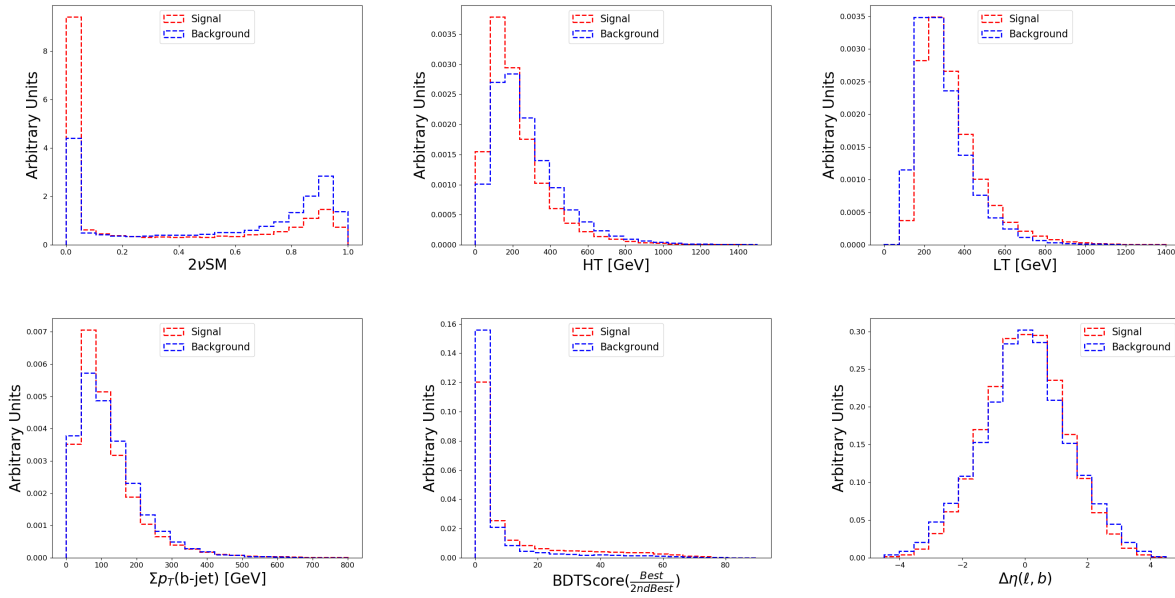


Figure 36: Normalised distributions of the input variables used in the event-level BDT (ordered from top left to bottom right via decreasing variable importance), for the signal and background classes are shown. **From top left to bottom right:** The output weight from the  $2\nu\text{SM}$  algorithm, the scalar sum of jet  $p_T$ , the scalar sum of lepton  $p_T$ , the sum of  $b$ -tagged jet  $p_T$ , the ratio of the best scoring  $\ell b$  system to the 2nd best scoring  $\ell b$  system from the output of the object-level BDT, and  $\Delta\eta$  between the two leptons, not coming from a  $Z$  candidate. The red and blue dotted lined histograms represent the signal and background classes events, respectively. These histograms are normalised to an area of 1. The input variable used in training is shown on the x-axis. The y-axis shows the relative number of events for the signal and background classes in arbitrary units.

events. In particular the output weight from the  $2\nu\text{SM}$  algorithm shows the most discrimination. When determining which input variables to use to train the event-level BDT, the output weight from  $2\nu\text{SM}$  was shown to provide the most sizeable boost in performance of the BDT. Surprisingly, the least important input variable,  $\Delta\phi$  between the non- $Z$  lepton system (leptons not originating from a  $Z$ -candidate) and the leading  $b$ -tagged jet, seem to discriminate well between signal and background. A possible explanation for its low ranking variable importance is due to it being relatively highly correlated with many of the other input variables used in the BDT. The modelling of the input variables used in the event-level BDT can be checked by referring to the expected number of events of data and simulation in control regions where they are defined. Note that certain input variables which are ill-defined in certain regions (e.g.  $\Delta\eta(\ell_{1,\text{non-}Z}, \ell_{2,\text{non-}Z})$  in the  $ZZb$  CR, as all leptons originate from a  $b$ -jet in this region) will not be shown. In Figure 37, MC predictions for the input variables used in the event-level BDT in the  $t\bar{t}Z$  CR are shown. The deviations between data and simulation, across all input variables used in the  $t\bar{t}Z$  CR, in all but three bins are within expected uncertainties. In Figure 38, MC predictions for the input variables used in the event-level BDT in the  $ZZb$  CR are shown. The deviations between data and simulation, across all input variables used in the  $ZZb$  CR, are within expected uncertainties. In Figure 39, MC predictions for the input variables used in the event-level BDT in the  $(tWZ)_{\text{fake}}$  CR are shown. The deviations between data and simulation, across all input variables used in the  $(tWZ)_{\text{fake}}$  CR, in all but one bin are within expected uncertainties. Overall, the vast majority of predictions between data and simulation in the bins

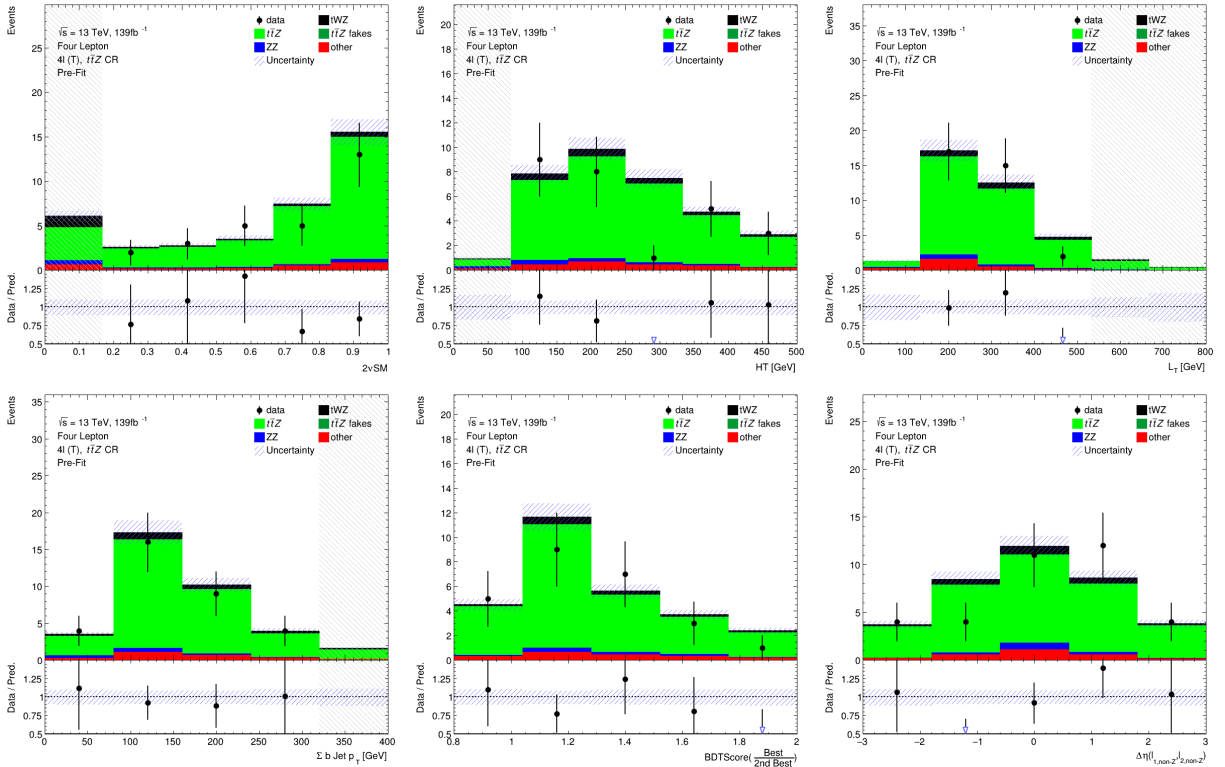


Figure 37: The expected number of events for the event-level BDT input variables (ordered from top left to bottom right via decreasing variable importance), in the  $t\bar{t}Z$  CR, are shown. **From top left to bottom right:** The output weight from the  $2\nu$ SM algorithm, the scalar sum of jet  $p_T$ , the scalar sum of lepton  $p_T$ , the sum of  $b$ -tagged jet  $p_T$ , ratio of the best scoring  $\ell b$  system to the 2nd best scoring  $\ell b$  system from the output of the object-level BDT, and  $\Delta\eta$  between the two leptons, not coming from a  $Z$  candidate. The data is given by the black points and the MC predictions for each process are given by the filled histograms. The vertical lines on the data points represent the statistical uncertainty in the data and the blue diagonally-lined bands represent the total (statistical and systematic added in quadrature) uncertainty. The lower panel in each plot shows the ratios of the data to the theoretical predictions. Bins with  $\frac{\text{signal}}{\text{background}}$  greater than 0.1 are kept blinded. Blinded bins are shaded with black diagonal lines and their data points are omitted.

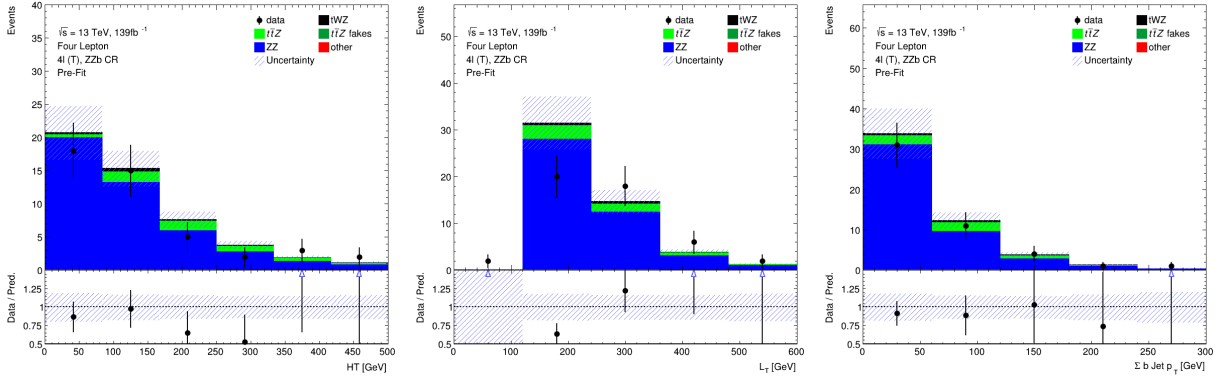


Figure 38: The expected number of events for the event-level BDT input variables (ordered from top left to bottom right via decreasing variable importance), in the  $ZZb$  CR, are shown. **From left to right:** The scalar sum of jet  $p_T$ , the scalar sum of lepton  $p_T$ , and the sum of  $b$ -tagged jet  $p_T$ . The data is given by the black points and the MC predictions for each process are given by the filled histograms. The vertical lines on the data points represent the statistical uncertainty in the data and the blue diagonally-lined bands represent the total (statistical and systematic added in quadrature) uncertainty. The lower panel in each plot shows the ratios of the data to the theoretical predictions. Bins with  $\frac{\text{signal}}{\text{background}}$  greater than 0.1 are kept blinded. Blinded bins are shaded with black diagonal lines and their data points are omitted.

of the event-level BDT distributions in the  $t\bar{t}Z$  CR,  $ZZb$  CR and  $(tWZ)_{\text{fake}}$  CR, are within the expected uncertainties. Therefore, these input variables are well-modelled and reasonable to include as inputs to the event-level BDT. In Table 12, the hyper-parameters used in the event-level BDT are shown. Since

Hyper-parameter	Value	Description
loss	deviance	The loss function to be optimised
criterion	friedman_mse	The function used to measure the quality of a split
n_estimators	200	The number of boosting stages to perform
learning_rate	0.1	The step size at each iteration during optimisation
max_depth	6	The maximum depth of the individual regression estimators
min_samples_split	2	The minimum number of samples (events) required to split an internal node
min_samples_leaf	1	The minimum number of samples (events) required to be at a leaf node
validation_fraction	0.1	The proportion of training data to set aside as validation set for early stopping
n_iter_no_change	20	Training terminates when the validation score does not improve in all of the previous

Table 12: A list of the hyper-parameters used in the event-level BDT is shown. Hyper-parameters not listed in this table use the default values as stated in the Scikit-learn Documentation[87].

the training is performed on  $t\bar{t}Z$  and  $ZZ$  events for the background class, it is ensured that the relative weighting of these events are such that they mimic the amount of  $t\bar{t}Z$  and  $ZZ$  expected to be present in the regions where the BDT discriminator is used. This is done by applying normalization weights to each event, defined as,

$$W = \frac{\sigma \mathcal{L} \text{weight(MC)}}{\text{totalWeight(MC)}} \quad (4.14)$$

where  $\sigma$  is the cross section of the process,  $\mathcal{L}$  is the integrated luminosity,  $\text{weight(MC)}$  is the weight assigned to the event by the MC event generator and  $\text{totalWeight(MC)}$  is the sum of those weights for all the generated events. The number of events used in training for the signal and background classes were 41066 and 22608 respectively. Similarly to the object-level BDT, there is a dataset imbalance. This imbalance is corrected for, in the same way as before with the object-level BDT, by ensuring that the

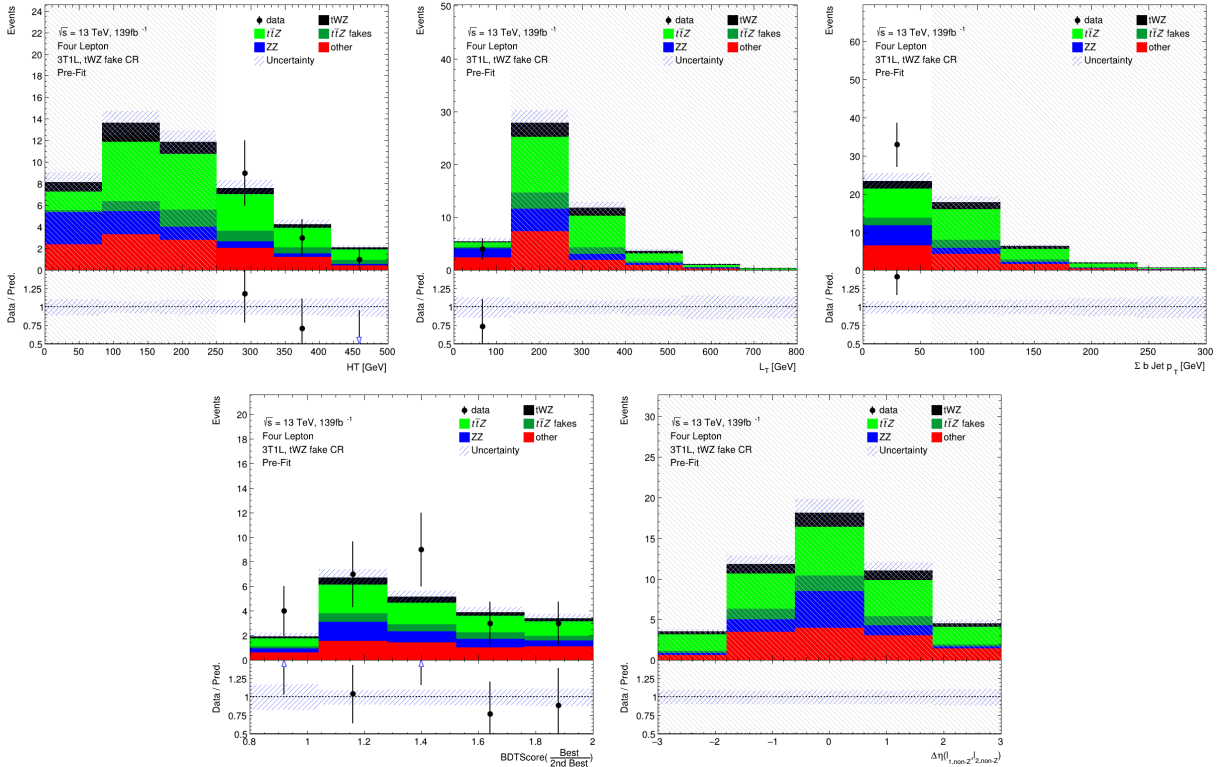


Figure 39: The expected number of events for the event-level BDT input variables (ordered from top left to bottom right via decreasing variable importance), in the  $(tWZ)_{\text{fake}}$  CR, are shown. **From top left to bottom right:** The output weight from the  $2\nu\text{SM}$  algorithm (See Section 4.7.1), the scalar sum of jet  $p_T$ , the scalar sum of lepton  $p_T$ , the sum of  $b$ -tagged jet  $p_T$ , ratio of the best scoring  $\ell b$  system to the 2nd best scoring  $\ell b$  system from the output of the object-level BDT (See Section 4.7.3), and  $\Delta\eta$  between the two leptons, not coming from a  $Z$  candidate. The data is given by the black points and the MC predictions for each process are given by the filled histograms. The vertical lines on the data points represent the statistical uncertainty in the data and the blue diagonally-lined bands represent the total (statistical and systematic added in quadrature) uncertainty. The lower panel in each plot shows the ratios of the data to the theoretical predictions. Bins with  $\frac{\text{signal}}{\text{background}}$  greater than 0.1 are kept blinded. Blinded bins are shaded with black diagonal lines and their data points are omitted.

relative weighting of each event is such that the sum of the signal weights is equal to the sum of the background weights. In order to avoid over-training, in the same way that was performed for the object-level BDT (See Section 4.7.3), the BDT outputs to the training set and a test set can be studied. In Figure 40 the normalised histograms of the training and test sets (extracted from fold 5 from a 5 fold kfold cross validation) for signal and background is shown. The shapes of the training and test sets for both signal

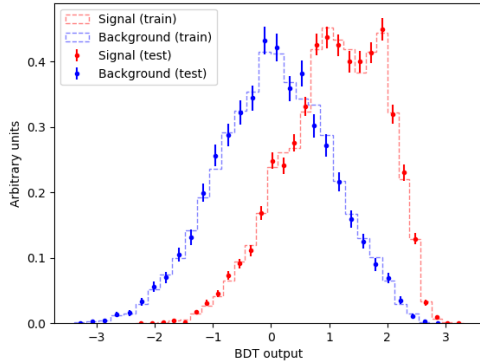


Figure 40: Normalised histograms of the event-level BDT discriminator output from the signal and background classes for the training and test sets from the 5th fold in a 5 fold kfold cross validation are shown. The output of the event-level BDT is shown on the x-axis and the relative number of events (normalised to have an area of 1, in arbitrary units) is shown on the y-axis. The training set for the signal class is shown by the red dotted histogram. The test set for the signal class is shown by the red points, with the total uncertainty represented by the vertical error bars. The training set for the background class is shown by the blue dotted histogram. The test set for the background class is shown by the blue points, with the total uncertainty represented by the vertical error bars.

and background agree within uncertainties in the vast majority of bins. This is a good indicator that no over-training occurred, since it indicates that statistical fluctuations (or noise) present in the training set was not learnt during training. As with the object-level BDT, another over-training check is performed, by ensuring that the variance of the mean accuracy of each folds' test set in a 5 fold kfold cross validation is sufficiently small. This indicates that fluctuations in features from different training sets are not learnt by the BDT. For the event-level BDT, a variance of 0.00026 was calculated for the mean accuracies of each folds' test set in cross validation, providing further evidence that no over-training occurred. In Figure 41, normalised distributions of the signal and total background of the event-level BDT discriminator output in the  $tWZ$  OF SR,  $tWZ$  SF SR and  $t\bar{t}Z$  CR, are shown.

The event-level BDT discriminates well between signal and background events in the  $tWZ$  OF SR,  $tWZ$  SF SR and  $t\bar{t}Z$  CR, with separations of 8.98%, 10.6% and 20.6%, respectively.

## 4.8 Systematic Uncertainties

The final results are obtained with a maximum likelihood fit (described in Section 4.9.1) in which normalisations and shapes of distributions are allowed to vary to account for uncertainties of both experimental and theoretical origin. Systematic uncertainties are allowed to vary within a pre-determined envelope (consisting of two MC templates) which defines the bounds within which the systematic can vary. In this

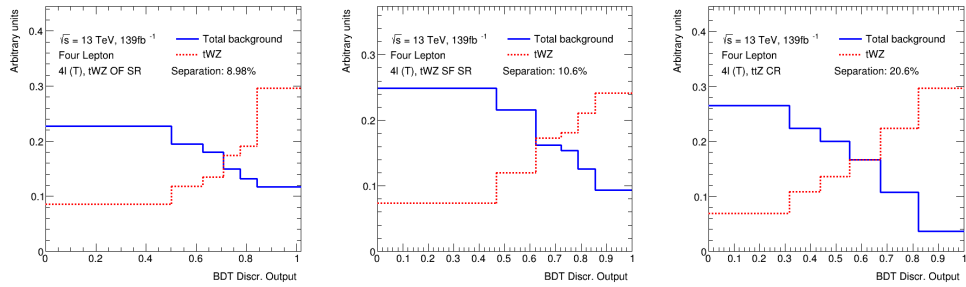


Figure 41: Normalised distributions of the signal and total background of the event-level BDT discriminator output in the  $tWZ$  OF SR,  $tWZ$  SF SR and  $t\bar{t}Z$  CR (left to right) are shown. The dotted red and solid blue lines represent the distributions of the signal and total background events respectively. These histograms are normalised to an area of 1. The x-axis shows the event-level BDT discriminator output and the y-axis shows the relative number of events in arbitrary units.

1198 section, the methods used to determine the variations that form the inputs to the fit are described.

#### 1199 4.8.1 Experimental uncertainties

1200 In this section, the experimental systematic uncertainties are outlined.

- 1201 • **Luminosity:**

1202 The 2015–2018 luminosity estimate of  $139 \text{ fb}^{-1}$  has a relative uncertainty of 3%. The uncertainty  
 1203 associated with the luminosity is obtained using the LUCID-2 detector [22], which is the primary  
 1204 luminosity monitor for ATLAS. This systematic uncertainty affects all processes modelled using MC  
 1205 simulations.

- 1206 • **Pile-up modelling:**

1207 An uncertainty related to the SFs used for MC to account for differences in pile-up distributions  
 1208 between MC and data is applied. This uncertainty is obtained by re-scaling the  $\langle \mu \rangle$  value in data  
 1209 by 1.00 and 1/1.18 corrections are only applied to MC.

- 1210 • **Jet vertex tagger:**

1211 Uncertainties associated to the  $JVT$  are applied via the `JetJvtEfficiency` package [20] which  
 1212 account for the residual contamination from pile-up jets after pile-up suppression and the MC  
 1213 generator choice [14].

- 1214 • **Heavy- and light-flavour tagging:**

1215 An additional uncertainty is assigned to account for the extrapolation of the  $b$ -tagging efficiency  
 1216 measurement from the  $p_T$  region used to determine the correction factors to regions with higher  $p_T$ .

- 1217 • **Electron identification efficiency:**

1218 Uncertainties associated with the electron efficiency SFs arise from the reconstruction, ID, isolation  
 1219 and trigger efficiencies [18]. They correct for the efficiency difference between data and MC [13] and

are measured with a "tag-and-probe" method in  $Z \rightarrow e^+e^-$  and  $J/\psi \rightarrow e^+e^-$  events. The information on the correlation of the different components of the systematic uncertainties are provided for all efficiency measurements. The default correlation model for the uncertainties is used, which provides one up/down variation for each of the SF components separately [18, 19].

• **Muon identification efficiency:**

As for electrons, SFs obtained from  $Z \rightarrow \mu^+\mu^-$  and  $J/\psi \rightarrow \mu^+\mu^-$  events are applied to correct for the differences between data and MC in the muon ID, isolation and trigger efficiencies [16]. Uncertainties on these SFs are applied as up/down variations of the nominal SFs for each component.

## 4.8.2 Theoretical uncertainties

In this section, the theoretical systematic uncertainties are outlined.

•  **$t\bar{t}Z$  background:**

An overall normalization uncertainty of 10% is considered for the  $t\bar{t}Z$  background. Two generic shape systematic uncertainties are considered for the  $t\bar{t}Z$  background. They are constructed (see Section 4.8.3) by either applying a linear or triangular interpolation to up and down variations which are defined to be  $\pm 20\%$  from the nominal  $t\bar{t}Z$  background. These linear and triangular variations are applied to distributions used in the maximum likelihood fit (described in Section 4.9.1).

•  **$ZZ$  background:**

An overall normalization uncertainty of 30% is considered for the  $ZZ$  background.

•  **$t\bar{t}H$  background:**

An overall normalization uncertainty of 20% is considered for the  $t\bar{t}H$  background.

•  **$tZq$  background:**

An overall normalization uncertainty of 14% is considered for the  $tZq$  background.

•  **$t\bar{t}Z$  fake background:**

An overall normalization uncertainty of 50% is considered for the  $t\bar{t}Z$  fake background.

• **other background processes:**

The 'other' background consists of many processes which have minimal but non-negligible contribution in the signal regions (See Table 7). An overall normalization uncertainty of 30% is considered for the 'other' background processes.

•  **$tWZ$ :**

A modelling uncertainty on  $tWZ$  is considered by comparing the nominal sample (using the DR1 scheme) and a DR2 sample. Two generic shape systematic uncertainties are applied to the  $tWZ$  signal. They are constructed (see Section 4.8.3) by either applying a linear or triangular interpolation to up and down variations which are defined to be  $\pm 20\%$  from the nominal  $tWZ$  signal.

### 1253 4.8.3 Generic shape systematic uncertainties

1254 The quantity which is measured from the maximum likelihood fit, the expected signal strength of  $tWZ$   
 1255 ( $\mu(tWZ)$ ), is defined as the ratio of the cross section of  $tWZ$ ,  $\sigma(tWZ)$ , to the SM cross section of  $tWZ$ ,  
 1256  $\sigma_{SM}(tWZ)$  (described in more detail in Section 4.9.1). It is evident that the tetralepton channel is sta-  
 1257 tistically limited, as seen by the small number of expected events in the control plots shown previously  
 1258 in Section 4.5. Therefore it is expected that the uncertainty on  $\mu(tWZ)$  is dominated by statistical  
 1259 uncertainty and that the impact of shape systematic uncertainties will be negligible in comparison. In  
 1260 this analysis, not all of the systematic uncertainties have been estimated, as this involves time consum-  
 1261 ing analysis of extra event samples, especially those related to the modelling of background processes.  
 1262 However, as described above, these missing systematic uncertainties are likely to have a negligible im-  
 1263 pact. To check this assumption, generic systematic uncertainties are generated as a proxy for the missing  
 1264 systematic uncertainties for the modelling of processes. If these generic shape systematic uncertainties  
 1265 have negligible impact on the measurement of the expected  $\mu(tWZ)$ , it would give us confidence that the  
 1266 missing systematic uncertainties will not greatly alter our results when they are eventually added. An  
 1267 envelope consisting of two MC templates is constructed that represents the bounds in which the system-  
 1268 atic can vary in the fit. One with the nominal MC template increased by 20% on its normalisation and  
 1269 the other with the nominal MC template decreased by 20% on its normalisation. The templates are then  
 1270 modified from their original shape either by doing linear interpolation (from the leftmost-up variation to  
 1271 the rightmost-down variation) or triangular interpolation (shape is set to zero at the higher and lower  
 1272 parts and extends towards the envelope in the middle). The linear and triangular interpolation is done  
 1273 using TRF’s **ForceShape** option [81], which alter the original templates (as described above). In Figure  
 1274 42 the envelope before and after the shape change, for both the linear and triangular interpolations, for  
 1275 the  $t\bar{t}Z$  background in the  $t\bar{t}Z$  CR is shown.

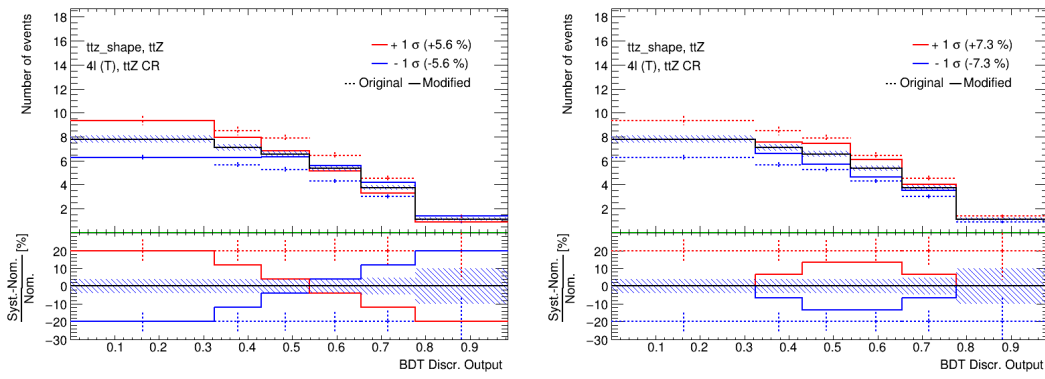


Figure 42: The  $t\bar{t}Z$  generic systematic uncertainty before and after linear (left) and triangular (right) interpolation in the  $t\bar{t}Z$  CR is shown. The output from the event-level BDT shown on the x-axis. In the upper panel, the number of events is shown on the y-axis. In the lower panel, the difference between the systematic variation and the nominal template, divided by the nominal template, is shown on the y-axis. The nominal  $t\bar{t}Z$  template is shown by the solid black lined histogram, with the diagonal lined bands representing its total uncertainty. The templates of the upper and lower envelopes, before modification, is given by the dotted red and blue lined histograms respectively. The templates of the upper and lower envelopes, after modification, is given by the solid red and blue lined histograms respectively, with the vertical dotted lines representing its total uncertainty.

1276 Both a linear and a triangular generic systematic uncertainty are considered for  $tWZ$  and the most  
1277 dominant background process,  $t\bar{t}Z$ .

## 1278 4.9 Analysis Pipeline and TRexFitter

1279 For this analysis, we make use of CERN’s high energy data analysis framework, **ROOT**, which is written in  
1280 *C++*, through **Python** using **PyROOT**. **Python** is used extensively in many fields of science (not limited to  
1281 physics and data science) due to its simplicity and ongoing support by the communities which utilize it.  
1282 In **PyROOT** users are able to access the full **ROOT** functionality within **Python**. More specifically, **PyROOT**  
1283 provides **Python** bindings for **ROOT**. To produce all control plots (including fit statistics, e.g. limit,  
1284 significance,  $\mu_{tWZ}$ ), we used **TRexFitter** (tag: **TRexFitter-00-04-13**), which is a framework for binned  
1285 template profile likelihood fits [96].

1286  
1287 The analysis pipeline starts with sample derivations (data and simulation from ATLAS with certain  
1288 selection criteria applied in order to reduce its file size such that it is more manageable to work with)  
1289 being submitted to the grid for dataset production. This applies cuts and selections to the already reduced  
1290 derivations and produces datasets with trees containing variables (e.g. scale factors, variables, MC truth  
1291 flags) that will be used at future stages in the analysis. These datasets are then read by **PyROOT** where the  
1292 events are looped over, before being written to **ROOT** files as input to **TRexFitter**. The **Python** scripts are  
1293 used to define the different regions and apply the final cuts and selections outlined in Table 6. In addition  
1294 to this purpose, they are used to train the two BDTs and to produce the output from these trained BDTs.  
1295 As each event is looped over, the cuts and selection criteria are checked for the given event and is either  
1296 discarded (if the event does not pass the selection criteria), or gets written to a **ROOT** file (if the event  
1297 passes the selection criteria) corresponding to the MC sample and Run 2 data-set which it belongs to.  
1298 These **ROOT** files contain all variables, weights and scale factors (corresponding to an event) which we wish  
1299 to use in **TRexFitter**. **TRexFitter** then takes these files as input, runs a maximum likelihood fit and  
1300 produces relevant plots (e.g. expected number of events, pull plots) and statistical parameters (e.g. limit,  
1301 significance,  $\mu_{tWZ}$ ).

### 1302 4.9.1 Fitting Procedure

1303 Maximum likelihood fits can be used to calculate the probability of data being consistent with a given  
1304 hypothesis. In this analysis, the hypothesis is represented by the signal strength of  $tWZ$  production,  
1305  $\mu(tWZ)$ , defined as,

$$\mu(tWZ) = \frac{\sigma(tWZ)}{\sigma_{SM}(tWZ)} \quad (4.15)$$

1306 where  $\sigma_{(tWZ)}$  expected cross section of  $tWZ$  and  $\sigma_{SM}(tWZ)$  is the SM cross section of  $tWZ$ . The  
1307 maximum likelihood fit is performed by finding the set of values for the parameters which maximize a  
1308 likelihood function or equivalently by minimizing the negative logarithm of the likelihood function. In  
1309 this context, the likelihood function is constructed from probability distributions of the expected number  
1310 of events in each bin of a distribution and the nuisance parameters. The data in a given bin of a distribu-  
1311 tion is expected to follow a Poisson probability distribution representing its expected number of events.

1312 Nuisance parameters represent the systematic uncertainties that could affect the estimation of signal and  
 1313 background but are not directly related to our final measurement. The likelihood function,  $L(\mu, \theta)$ , used  
 1314 in analyses involving binned histograms of signal and background events is therefore constructed as a  
 1315 product of Poisson probability terms for all bins ( $N_{bins}$ ) and probability density functions that define the  
 1316 nuisance parameters, and is given by [24],

$$L(\mu, \theta) = \prod_i^{N_{bins}} \frac{(\mu s_i(\vec{\theta}) + b_i(\vec{\theta}))^{n_i}}{n_i!} e^{-(\mu s_i(\vec{\theta}) + b_i(\vec{\theta}))} \prod_{\theta \in \vec{\theta}} \rho(\theta) \quad (4.16)$$

1317 where  $\mu$  is the signal strength of the process of interest,  $s_i$  and  $b_i$  represent the expected number of signal  
 1318 and background events in bin  $i$  of the distribution respectively,  $\theta$  represents a nuisance parameter contained  
 1319 in the set of all nuisance parameters ( $\vec{\theta}$ ) and  $\rho(\theta)$  represents the probability density functions which define  
 1320 the nuisance parameter's distribution. In analyses with multiple regions, the likelihood function contains  
 1321 all bins across the regions. A fit across all regions in the tetralepton channel is performed to determine  
 1322 the sensitivity of  $tWZ$  in this channel. Plots shown prior to the fit are referred to as *pre-fit* and those  
 1323 shown after the fit are referred to as *post-fit*. In this analysis, the *mixed data and MC* fit setup [97]  
 1324 is used. This is done to obtain the most accurate prediction of the expected results while keeping the  
 1325 signal regions blinded. For this setup, first a background-only fit to the control regions using data is  
 1326 performed to estimate the nuisance parameters. Then these estimates are used to construct a modified  
 1327 Asimov dataset in the signal regions. Finally, the fit is performed using data in the control regions and  
 1328 the aforementioned modified Asimov data-set in the signal regions. In these fits, the POI is  $\mu(tWZ)$ . The  
 1329 POI is ultimately the quantity to be measured and it is set as a *free parameter* in the fit. This means that  
 1330 during the fitting procedure,  $\mu(tWZ)$  is unconstrained and can take any value in the fit. The nuisance  
 1331 parameters are assigned to the systematic uncertainties outlined in Section 4.8. Furthermore, a gamma  
 1332 ( $\gamma$ ) nuisance parameter for a bin is added to the likelihood function if the statistical uncertainty in the  
 1333 bin exceeds 0.1% of its nominal value. A sample's shape and normalisation nuisance parameter is pruned  
 1334 (removed from the limit/fit) if the impact of the systematic uncertainty on the POI is less than 0.01.  
 1335 Pruning is done per sample and per region on the shape and normalisation uncertainties for samples.  
 1336 An auto-binning algorithm, `TransfoD` [32, 33], was used to define the binning. This aims to maximise  
 1337  $\frac{\text{signal}}{\text{background}}$  in each bin. Furthermore, it aims to avoid defining bins with a low number of events. The  
 1338 auto-binning algorithm works by scanning through the bins of the given distribution with user-defined  
 1339 bins of equal width, and merges bins until a certain fraction of  $\frac{\text{signal}}{\text{background}}$  events is obtained. The merging  
 1340 threshold,  $MT$ , is defined as,

$$MT = z_s \frac{n_s}{N_s} + z_b \frac{n_b}{N_b} \quad (4.17)$$

1341 where  $n_s$  and  $n_b$  are the number of signal and background events in the merging bin, respectively. The total  
 1342 number of signal and background events is given by  $N_s$  and  $N_b$ , respectively. User-defined parameters,  
 1343  $z_s$  and  $z_b$ , control the maximum fraction of signal and background events in each bin with the condition,  
 1344  $z_s + z_b = \text{number of bins}$ . A bin is formed when  $MT \geq 1$ . To characterise the sensitivity and associated  
 1345 uncertainty of our measurement of  $\mu(tWZ)$ , we compute two metrics: the expected significance ( $Z_\mu^{exp}$ )  
 1346 and the expected upper limit ( $\mu_{up}^{exp}$ ). In this context, the expected significance can be interpreted as,  
 1347 the probability that the expected signal is due to a background fluctuation. The expected significance,

1348  $Z_\mu^{exp}$ , is related to the  $p$ -value. The  $p$ -value can be defined as the probability, under the assumption of a  
1349 given hypothesis (in the context of this analysis, this would refer to the background-only hypothesis), of  
1350 finding data of equal or greater incompatibility with the predictions of the hypothesis [43]. The expected  
1351 significance can be written in terms of the  $p$ -value ( $p$ ) by,

$$Z_\mu^{exp} = \Phi^{-1}(1 - p) \quad (4.18)$$

1352 where  $\Phi^{-1}$  is the inverse of the cumulative function of the standard Gaussian distribution. This is defined  
1353 such that a Gaussian distributed variable found  $Z_\mu^{exp}$  standard deviations above its mean has an area  
1354 under its rightmost tail equal to  $p$ . Larger values indicate lower probabilities and smaller values indicate  
1355 higher probabilities. Particle physicists have adopted a standard to define the significance necessary  
1356 for evidence and discovery of a particular particle or phenomena. A  $3\sigma$  (corresponding to a background  
1357 fluctuation probability of  $\approx 10^{-3}$ ) significance is considered to be evidence and a  $5\sigma$  (corresponding to a  
1358 background fluctuation probability of  $\approx 10^{-7}$ ) is considered to be a discovery. The expected upper limit  
1359 is a single-sided interval test statistic, associated with the parameter of interest (POI) in the maximum-  
1360 likelihood fit ( $\mu(tWZ)$ , in our case). In this context, the expected upper limit can be understood in the  
1361 following way: consider running an ensemble of MC toy experiments, each with their own confidence  
1362 interval (a range of possible values for  $\mu(tWZ)$ ). An expected upper limit, at some fixed percentage  $x\%$   
1363 (or *confidence level*), can be determined from this ensemble. The expected upper limit tells us that,  $x\%$   
1364 of the toy MC experiment's confidence intervals will contain the true value of  $\mu(tWZ)$ . A commonly used  
1365 percentage in particle physics is 95%, which we adopt for this analysis. In particle physics, this is referred  
1366 to as the *CLs Method* [43]. The test statistic derived from the CLs method can be calculated 'brute  
1367 force' by running these MC toy experiments, however this is very CPU intensive. Asymptotic formulae  
1368 are able to describe the underlying CLs test statistic distributions under certain approximations [10].  
1369 Instead of running toy MC experiments, we use asymptotic formulae to perform the CLs method, which  
1370 considerably reduces computation time. The significance and upper limits which are calculated in this  
1371 analysis are given a prefix of 'expected' in order to indicate that these are results from a blinded analysis.

## 1372 4.10 Results

1373 In the section, an expected upper limit and an expected significance are set on the signal strength of  $tWZ$ .  
1374 This is performed for the current analysis in the tetralepton channel as well as for a combined analysis  
1375 across the trilepton and tetralepton channels. The trilepton analysis was performed as an independent  
1376 study by Benjamin Warren (UCT) [99]. Note that throughout this section, all signal regions remain  
1377 blinded.

### 1378 4.10.1 Tetralepton Channel

1379 In Figure 43, the pre-fit distributions of the expected number of events as a function of the variables used  
1380 in the likelihood fit in each region are shown.  
1381 In Figure 44, the post-fit distributions of the expected number of events as a function of the variables  
1382 used in the likelihood fit in each region are shown.

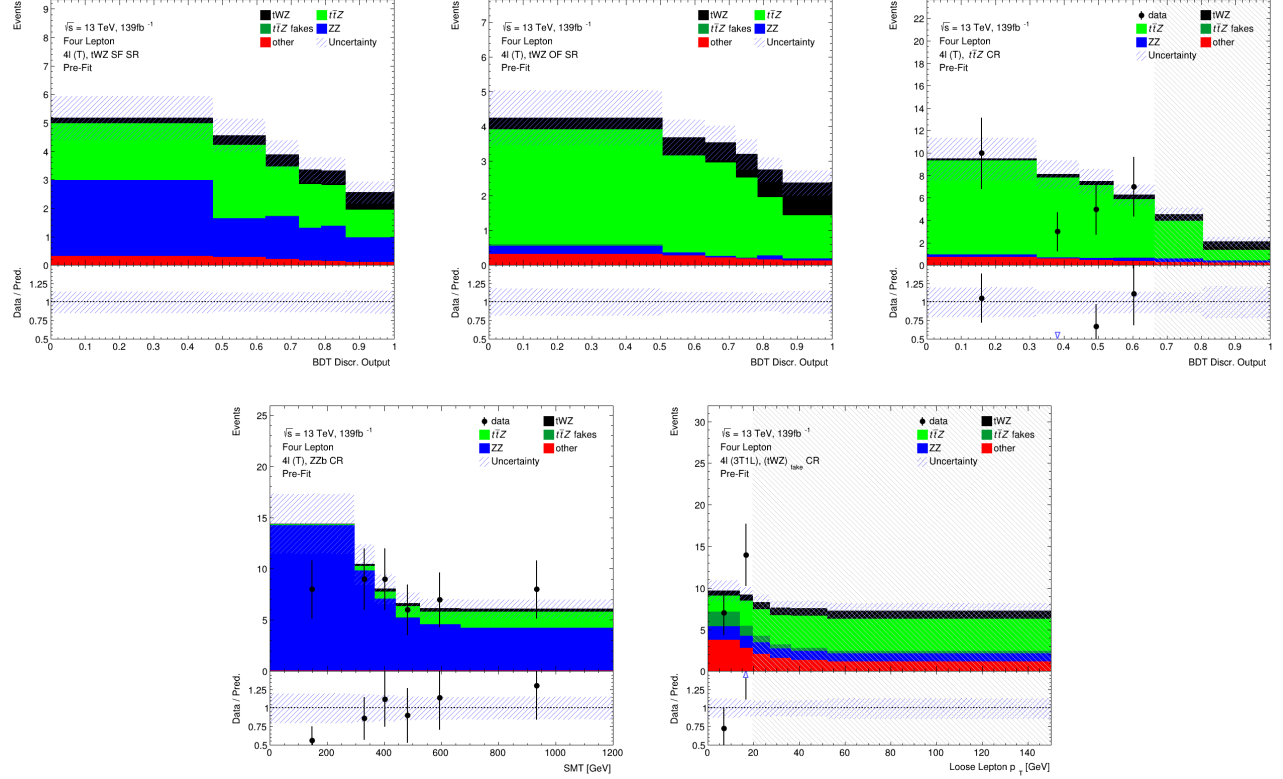


Figure 43: Pre-fit distributions (blinded) of variables used in the fit. **From top left to bottom right:** The event-level BDT Discr. Output in the  $tWZ$  SF SR, the event-level BDT Discr. Output in the  $tWZ$  OF SR, the event-level BDT Discr. Output in the  $t\bar{Z}$  CR,  $SMT = \sum p_T(\ell) + \sum p_T(jet) + E_T^{\text{miss}}$  in the  $ZZb$  CR, and  $p_T$ (loose lepton) in the  $(tWZ)_{\text{fake}}$  (3T1L) CR. The data is given by the black points and the MC predictions for each process are given by the filled histograms. The vertical lines on the data points represent the statistical uncertainty in the data and the diagonally-lined bands represent the total (statistical and systematic added in quadrature) uncertainty. The lower panel in each plot shows the ratios of the data to the theoretical predictions. Bins in the CRs with  $\frac{\text{signal}}{\text{background}}$  greater than 0.1 are kept blinded. Blinded bins in the CRs are shaded with black diagonal lines and their data points are omitted. The plots in the  $tWZ$  OF SR and  $tWZ$  SF SR are kept blinded by omitting the data points.

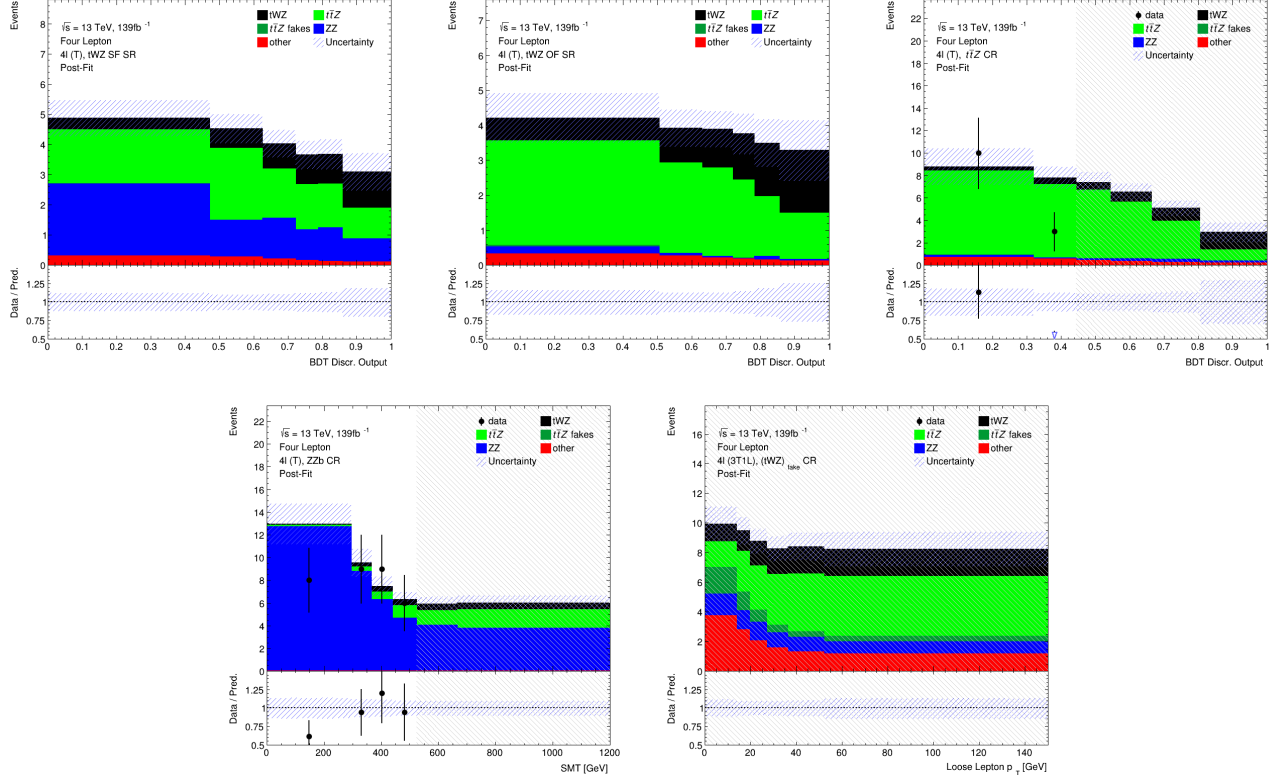


Figure 44: Post-fit distributions (blinded) of variables used in the fit are shown. **From top left to bottom right:** The event-level BDT Disc. Output in the  $tWZ$  SF SR, the event-level BDT Disc. Output in the  $tWZ$  OF SR, the event-level BDT Disc. Output in the  $t\bar{Z}$  CR,  $SMT = \sum p_T(\ell) + \sum p_T(jet) + E_T^{\text{miss}}$  in the  $ZZb$  CR, and  $p_T$ (loose lepton) in the  $(tWZ)_\text{fake}$  (3T1L) CR. The data is given by the black points and the MC predictions for each process are given by the filled histograms. The vertical lines on the data points represent the statistical uncertainty in the data and the diagonally-lined bands represent the total (statistical and systematic added in quadrature) uncertainty. The lower panel in each plot shows the ratios of the data to the theoretical predictions. Bins in the CRs with  $\frac{\text{signal}}{\text{background}}$  greater than 0.1 are kept blinded. Blinded bins in the CRs are shaded with black diagonal lines and their data points are omitted. The plots in the  $tWZ$  OF SR and  $tWZ$  SF SR are kept blinded by omitting the data points.

In Table 13, the expected number of events (after the fit) for each sample in each region is shown. The

		$tWZ$ OF SR	$tWZ$ SF SR	$t\bar{Z}$ CR	$ZZb$ CR	$(tWZ)_{\text{fake}}$ CR
$t\bar{Z}$		$13.2 \pm 1.5$	$9.6 \pm 1.1$	$29.9 \pm 3.6$	$5.1 \pm 0.6$	$18.5 \pm 2.2$
$t\bar{Z}$ fakes		$0.070 \pm 0.047$	$0.033 \pm 0.026$	$0.072 \pm 0.042$	$0.052 \pm 0.021$	$5.1 \pm 2.3$
$tWZ$		$7.8 \pm 3.3$	$5.3 \pm 2.2$	$5.7 \pm 2.6$	$2.9 \pm 1.2$	$10.2 \pm 4.3$
$ZZ$		$0.48 \pm 0.12$	$7.7 \pm 1.2$	$1.1 \pm 0.2$	$40.6 \pm 6.3$	$6.9 \pm 1.1$
other	$t\bar{t}$	$6e-06 \pm 3e-06$	$0.25 \pm 0.44$	$0.27 \pm 0.22$	$6e-06 \pm 3e-06$	$2.4 \pm 0.9$
	$tZq$	$0.083 \pm 0.040$	$0.076 \pm 0.035$	$0.064 \pm 0.030$	$0.060 \pm 0.024$	$4.9 \pm 0.7$
	$t\bar{t}tW$	$0.0067 \pm 0.0079$	$0.0028 \pm 0.0028$	$6e-06 \pm 3e-06$	$0.0023 \pm 0.0056$	$0.94 \pm 0.29$
	$WZ$	$0.04 \pm 0.02$	$0.04 \pm 0.02$	$0.013 \pm 0.013$	$0.047 \pm 0.033$	$1.8 \pm 0.4$
	$t\bar{t}t$	$0.0010 \pm 0.0007$	$0.002 \pm 0.001$	$0.014 \pm 0.005$	$6e-06 \pm 3e-06$	$0.010 \pm 0.003$
	$t\bar{t}t\bar{t}$	$0.009 \pm 0.008$	$0.011 \pm 0.008$	$0.06 \pm 0.02$	$6e-06 \pm 3e-06$	$0.02 \pm 0.01$
	$t\bar{t}WW$	$0.029 \pm 0.026$	$0.03 \pm 0.02$	$0.3 \pm 0.1$	$0.01 \pm 0.03$	$0.2 \pm 0.1$
	$VVV(V = W/Z)$	$0.3 \pm 0.1$	$0.2 \pm 0.1$	$0.10 \pm 0.02$	$0.17 \pm 0.05$	$0.26 \pm 0.08$
	$t\bar{t}H$	$0.9 \pm 0.2$	$0.7 \pm 0.1$	$2.0 \pm 0.4$	$0.20 \pm 0.03$	$2.2 \pm 0.5$
	Total	$22.9 \pm 3.0$	$24.0 \pm 2.1$	$39.4 \pm 3.4$	$49.1 \pm 6.0$	$53.4 \pm 4.3$
	data	-	-	36	49	57

Table 13: The expected number of events (after the fit) for each sample in each region is shown.

1383

1384 expected upper limit of  $tWZ$  in the tetralepton channel is measured as,  $\mu_{up}^{exp} = 1.61^{+2.35}_{-1.16}$ . The expected  
 1385 significance of  $tWZ$  in the tetralepton channel is measured as,  $Z_\mu^{exp} = 1.44\sigma$ . The best-fit value of the  
 1386 signal strength,  $\mu(tWZ) = \frac{\sigma(tWZ)}{\sigma(tWZ)_{SM}}$ , from the likelihood fit is measured as,  $\mu(tWZ) = 1.91^{+0.95}_{-0.82}$ . The  
 1387 best fit value of the signal strength is inconsistent with 1 by 9%. This indicates a disagreement between  
 1388 data and the post-fit model within post-fit model uncertainties. This may suggest that there is some  
 1389 mis-modelling in the backgrounds of the post-fit model. Since there is a small number of events in the re-  
 1390 gions of tetralepton channel, the disagreement may be due to statistical fluctuations in data or simulation.

1391

1392 The effect of each systematic uncertainty on the POI,  $\mu(tWZ)$ , in the fit can be studied from a *ranking*  
 1393 *plot* [84]. A ranking plot lists the nuisance parameters used in the fit in order of their *impact* on the POI.  
 1394 The impact of a nuisance parameter describes how much the nuisance parameter effects the extracted  
 1395 value of the POI from the fit. The impact of a nuisance parameter,  $\theta$ , is calculated by first fixing the  
 1396 pre-fit and post-fit uncertainties, given by  $\Delta\theta$  and  $\Delta\hat{\theta}$  respectively, of all the nuisance parameters to  
 1397  $\pm 1$ , performing the fit, and extracting the nominal value of the POI. The impact of a given nuisance  
 1398 parameter is then defined by the difference in this reference POI value to a POI value extracted from  
 1399 a fit performed by removing the given nuisance parameter. In Figure 45, a ranking plot showing the  
 1400 impact of the systematic uncertainties on the POI,  $\mu(tWZ)$  is shown. The systematic uncertainties with  
 1401 largest impacts are the cross sections of  $t\bar{Z}$  and  $ZZ$ , and shape modelling on  $t\bar{Z}$  ( $t\bar{Z}$  triangular shape)  
 1402 and  $tWZ$  ( $tWZ$ -DR2 and  $tWZ$  triangular shape). The cross section of  $ZZ$  is slightly shifted down in  
 1403 the fit. The  $t\bar{Z}$  cross section,  $tWZ$ -DR2 and  $t\bar{Z}$  triangular shape nuisance parameters are similarly  
 1404 shifted down in the fit from their nominal values, but to a much lesser degree than the cross section of  
 1405  $ZZ$ . These pulls are all within  $1\sigma$  uncertainty and are thus relatively small. It is expected that the  
 1406 modelling uncertainties (shape and normalisations) of the most dominant backgrounds (e.g.  $t\bar{Z}$ ,  $ZZ$ )  
 1407 have relatively large impacts on  $\mu(tWZ)$ , since the uncertainty of the analysis is dominated by statistical  
 1408 uncertainty.

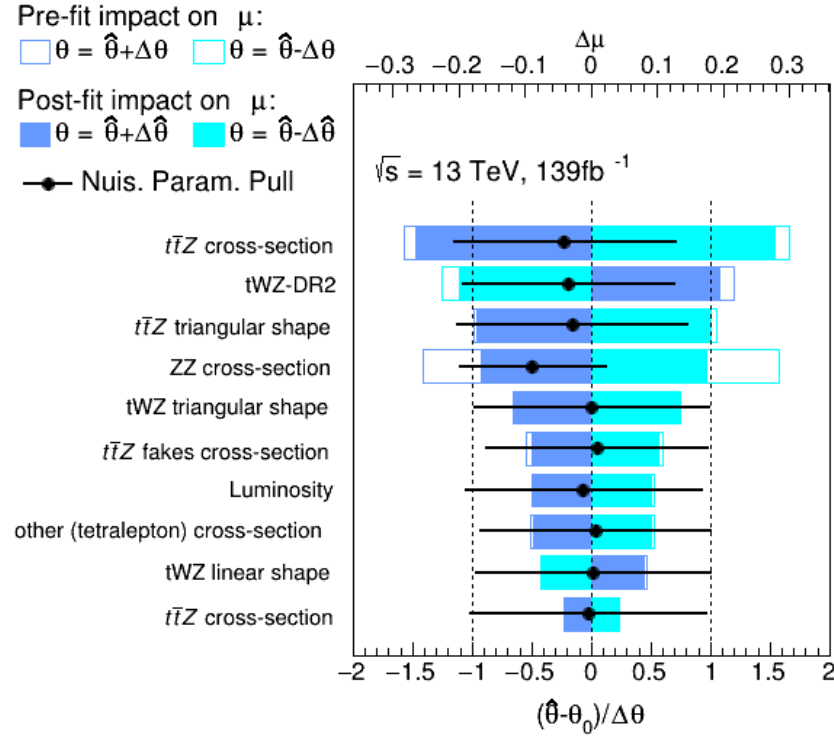


Figure 45: A ranking plot showing the impact (ordered from top to bottom via decreasing impact) of the systematic uncertainties (top 10) on the POI,  $\mu(tWZ)$ , in the tetralepton channel is shown. The best-fit value of the nuisance parameter is given by  $\hat{\theta}$ . The post-fit and pre-fit uncertainties are given by  $\Delta\hat{\theta}$  and  $\Delta\theta$  respectively. The post-fit and pre-fit impact of each nuisance parameter on  $\mu(tWZ)$  are shown with the solid and lined rectangles respectively. The empty and solid blue rectangles correspond to the pre-fit and post-fit impacts on  $\mu(tWZ)$  respectively. These impacts are shown on the upper axis ( $\Delta\mu$ ). On the lower axis, the nuisance parameter pull,  $\frac{\theta - \theta_0}{\Delta\theta}$ , is shown ( $\theta_0$  is the nominal pre-fit value of the nuisance parameter). The nuisance parameter pull is indicated by the black points, with their relative post-fit errors ( $\frac{\Delta\hat{\theta}}{\Delta\theta}$ ) shown by the black horizontal error bars.

#### 1409 4.10.2 Trilepton and Tetralepton Channels

1410 In the section, an expected upper limit and an expected significance are set on the signal strength of  $tWZ$   
 1411 ( $\mu(tWZ)$ ) from the combined fit across all regions of  $tWZ$  in the tetralepton and trilepton channels. The  
 1412 trilepton channel is an entirely independent analysis [99] that uses separate data and simulated events  
 1413 compared to the tetralepton channel. Although the trilepton channel uses separate data and simulated  
 1414 events, the treatment of the statistical and systematic uncertainties (and therefore the statistical model)  
 1415 in the combined fit is entirely coherent with the tetralepton channel. Therefore the inclusion of the  
 1416 trilepton channel in the combined fit is only a matter of adding the regions in the trilepton channel to the  
 1417 likelihood definition. The trilepton analysis follows a similar analysis strategy to that of the tetralepton  
 1418 analysis. It includes an event-level BDT which aims to discriminate between the  $tWZ$  and all background  
 1419 as well as an object-level BDT which aims to identify hadronically decaying  $W$  bosons to discriminate  
 1420 between  $tWZ$  and the large  $WZ$  background. One  $tWZ$  SR is defined and five CRs are defined. The  $WZ$   
 1421 and  $t\bar{t}Z$  CRs are defined to constrain the dominant  $WZ$  and  $t\bar{t}Z$  backgrounds. Three CRs which require  
 1422 that one of the three selected leptons are loose, are defined for  $WZ$ ,  $t\bar{t}Z$  and  $tWZ$  in order to constraint

the fake lepton component (using the MC template method - similar to the method used in Section 4.6 to estimate the fake lepton component). The expected upper limit of  $tWZ$  in the trilepton channel is measured as,  $\mu_{up}^{exp} = 2.65^{+3.67}_{-1.91}$ . The expected significance of  $tWZ$  in the trilepton channel is measured as,  $Z_\mu^{exp} = 0.75\sigma$ . The best-fit value of the signal strength,  $\mu(tWZ) = \frac{\sigma(tWZ)}{\sigma(tWZ)_{SM}}$ , from the likelihood fit is measured as,  $\mu(tWZ) = 1.16^{+1.33}_{-1.30}$ . The best fit value of the signal strength is consistent with 1. This indicates an agreement between data and the post-fit model within post-fit model uncertainties. Therefore, this demonstrates that the model is able to sufficiently model the background processes. In Table 14, the nuisance parameters that are included (or excluded) in terms of the likelihood function corresponding to a certain channel, used in the fit, are shown. Note that the  $\sigma(tWZ - DR2)$  systematic

Nuisance Parameter	Channel	
	trilepton	tetralepton
$\sigma(t\bar{t}H)$	✓	✓
$\sigma(t\bar{t}Z)$	✓	✓
$\sigma(WZ)$	✓	✓
$\sigma(tZq)$	✓	✓
$\sigma(ZZ)$	✓	✓
$\sigma(\text{other(trilepton)})$	✓	✗
$\sigma(\text{other(tetralepton)})$	✗	✓
$\sigma(t\bar{t}Z)_{fakes}$	✗	✓
$\sigma(t\bar{t})_{fakes}$	✓	✗
$\sigma(Z + jets)_{fakes}$	✓	✗
Luminosity	✓	✓
$jvt$	✓	✓
pileup	✓	✓
DL1r SF (b jets)	✓	✓
DL1r SF (light jets)	✓	✓
$\sigma(tWZ - DR2)$	✗	✓
lepton SF	✓	✓
$t\bar{t}Z$ triangular shape	✓	✓
$t\bar{t}Z$ linear shape	✓	✓
$WZ + b$ triangular shape	✓	✗
$WZ + b$ linear shape	✓	✗
$WZ + c$ triangular shape	✓	✗
$WZ + c$ linear shape	✓	✗

Table 14: A summary of the nuisance parameters used in the combined fit is shown. Nuisance parameters that are included in terms of the likelihood function corresponding to a certain channel are indicated with a ✓ and those which are excluded are indicated with a ✗.

uncertainty was not included in the trilepton analysis, and the trilepton analysis was unaltered when used in this analysis for the combined fit. The expected upper limit of  $tWZ$  across both channels is measured as,  $\mu_{up}^{exp} = 1.43^{+2.04}_{-1.03}$ . The expected significance of  $tWZ$  across both channels is measured as,  $Z_\mu^{exp} = 1.61\sigma$ . The best-fit value of the signal strength,  $\mu(tWZ) = \frac{\sigma(tWZ)}{\sigma(tWZ)_{SM}}$ , from the likelihood fit is measured as,  $\mu(tWZ) = 1.80^{+0.70}_{-0.65}$ . In Figure 46, the expected upper limits and the best-fit values of  $\mu(tWZ)$  in the trilepton channel, tetralepton channel and both channels combined are shown. It can be seen that the sensitivity of  $tWZ$  is mostly driven by the tetralepton analysis, with the trilepton analysis attributing a small decrease in the expected upper limit of the combined analysis, and its associated uncertainty. The best fit value for the signal strength on  $tWZ$ ,  $\mu(tWZ)$ , and the expected limits for the tri- and tetralepton channels are consistent with one-another (their uncertainties overlap). Therefore it is appropriate to combine these two analyses. In Figure 47, a ranking plot showing the impact of the

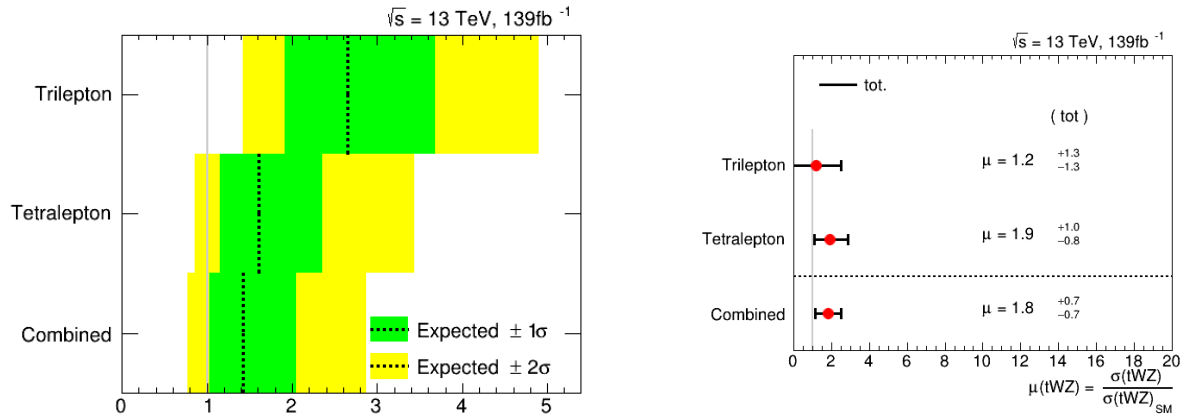


Figure 46: **Left:** The expected upper limits of the trilepton channel, tetralepton channel and both channels combine are shown. The y-axis shows the channels in which the fitting procedure was performed. The expected limits are represented by the vertical dotted line. One- and two-  $\sigma$  uncertainty bands are shown in green and yellow respectively. The vertical grey line indicates when  $\mu(tWZ) = 1$ . **Right:** The best-fit values of  $\mu(tWZ)$  from the fit for the trilepton channel, tetralepton channel and both channels combined are shown. The y-axis shows the channels in which the fitting procedure was performed. The signal strength  $\mu(tWZ)$  is shown on the x-axis. The nominal signal strengths are represented by the red dots. The total uncertainty associated with the best-fit  $\mu(tWZ)$  value is shown by the black error bars.

1443 systematic uncertainties on the POI,  $\mu(tWZ)$ , in the combined fit across both the tri- and tetralepton  
 1444 channels is shown. Some nuisance parameters are pulled down from their nominal pre-fit values, however  
 1445 these are all within 1  $\sigma$  uncertainty and are thus relatively small. The systematic uncertainties with  
 1446 largest impacts are the cross sections of  $t\bar{t}Z$ ,  $ZZ$  and  $WZ + b$ , and shape modelling on  $t\bar{t}Z$  ( $t\bar{t}Z$  triangular  
 1447 shape). The aforementioned nuisance parameters are slightly shifted down in the fit from their nominal  
 1448 value. The lower ranked systematic uncertainties are pulled in the fit from their nominal values, but to  
 1449 a much lesser degree than the cross section of those mentioned above. It is expected that the modelling  
 1450 uncertainties of the most dominant backgrounds (e.g.  $t\bar{t}Z$ ,  $ZZ$  and  $WZ + b$ ) have relatively large impacts  
 1451 on  $\mu(tWZ)$ , since the uncertainty of the analysis is dominated by statistical uncertainty.

#### 1452 4.10.2.1 Projection to Higher Luminosity

1453 The expected significance of  $tWZ$  across both channels was measured as  $1.61\sigma$  and it is likely that the  
 1454 analysis is statistically limited. Therefore, the question naturally arises whether or not it is possible to  
 1455 observe  $tWZ$  with a  $3\sigma$  or  $5\sigma$  significance and how much data one would need to achieve this. In this  
 1456 section we apply a fully blinded fit to the Asimov dataset for integrated luminosities larger than the  
 1457  $139\text{fb}^{-1}$  currently available from the ATLAS Full Run 2 dataset. This study gives us insight into the  
 1458 sensitivity of this analysis to the cross section of  $tWZ$  which we could expect if we were to replicate the  
 1459 current analysis, given more data. Given the upgrades planned for the LHC and the ATLAS detector,  
 1460 we will soon expect a large increase in available  $pp$  collision data (reaching  $\mathcal{L} = 3000\text{fb}^{-1}$  [36]). This  
 1461 study therefore gives us an idea of the sensitivity of this analysis to the cross section of  $tWZ$  which we  
 1462 can expect in the future. It would also provide a clear indication whether or not the uncertainties in this  
 1463 analysis is dominated by statistical uncertainties. In Figure 48, the expected upper limit and significance  
 1464 for combined fully blinded fits to the Asimov dataset across both the tri- and tetralepton channels for a

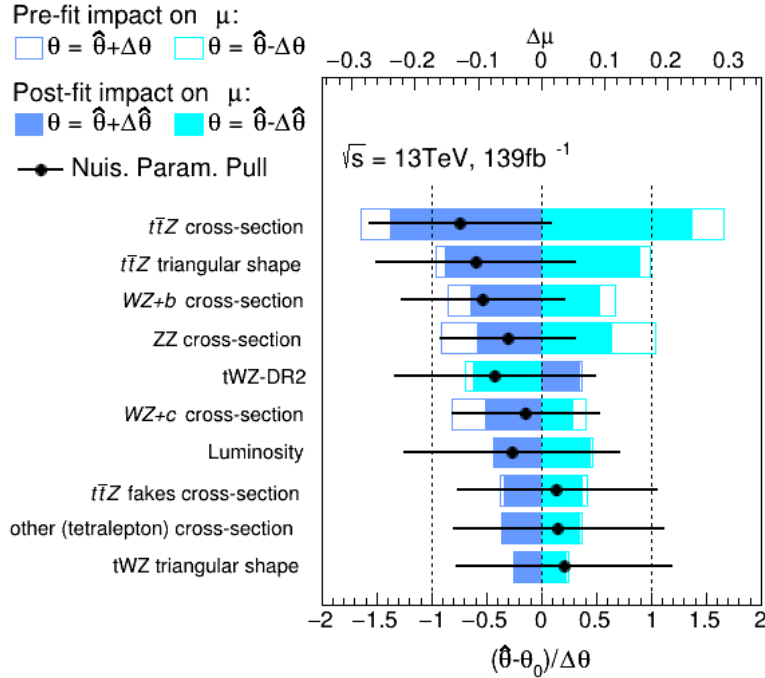


Figure 47: A ranking plot showing the impact of the systematic uncertainties (top 10) on the POI,  $\mu(tWZ)$ , in the combined fit across both the tri- and tetralepton channels is shown. The best-fit value of the nuisance parameter is given by  $\hat{\theta}$ . The post-fit and pre-fit uncertainties are given by  $\Delta\hat{\theta}$  and  $\Delta\theta$  respectively. The post-fit and pre-fit impact of each nuisance parameter on  $\mu(tWZ)$  are shown with the solid and lined rectangles respectively. The empty and solid blue rectangles correspond to the pre-fit and post-fit impacts respectively. These impacts are shown on the upper axis ( $\Delta\mu$ ). On the lower axis, the nuisance parameter pull,  $\frac{\hat{\theta}-\theta_0}{\Delta\theta}$ , is shown ( $\theta_0$  is the nominal pre-fit value of the nuisance parameter). The nuisance parameter pull is indicated by the black points, with their relative post-fit errors ( $\frac{\Delta\hat{\theta}}{\Delta\theta}$ ) shown by the black horizontal error bars.

range integrated luminosities are shown.

As we increase the total integrated luminosity, the sensitivity of this analysis to the  $tWZ$  process increases. The increase in sensitivity is shown by the rapid decrease of the expected upper limit and the rapid increase of the expected significance with increasing integrated luminosity. It can be noted that a  $3\sigma$  expected significance is achieved at  $\mathcal{L} \sim 400 \text{ fb}^{-1}$ , indicating evidence for observation of  $tWZ$ . The  $5\sigma$  significance 'discovery' standard is above our  $1000 \text{ fb}^{-1}$  luminosity range of study. Furthermore, these plots show that the sensitivity of  $tWZ$  is hindered by the low amount of events we observe, rather than the systematic effects. This is evident since increasing the luminosity, therefore increasing the number of events we see in the detector, directly causes a steady increase in sensitivity.

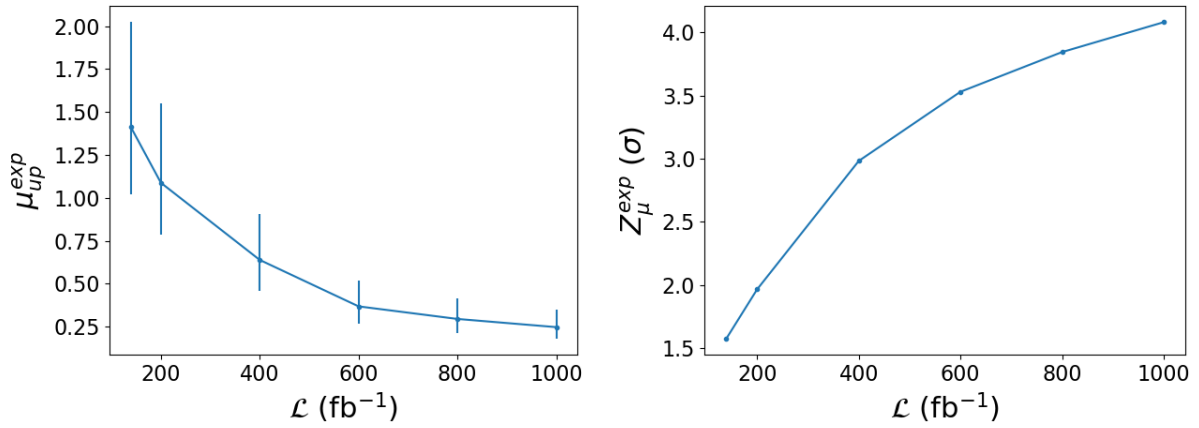


Figure 48: The expected upper limit (left) and significance (right) for combined fully blinded fits to the Asimov dataset across both the tri- and tetralepton channels for a range integrated luminosities are shown. **Left:** The integrated luminosity,  $\mathcal{L}$ , is shown on the x-axis. The expected upper limit,  $\mu_{up}^{exp}$ , is shown on the y-axis. The vertical lines represent the total uncertainty ( $\pm 1\sigma$ ) on the expected upper limit. **Right:** The integrated luminosity,  $\mathcal{L}$ , is shown on the x-axis. The expected significance,  $Z_\mu^{exp}$ , is shown on the y-axis. The vertical lines represent the total uncertainty ( $\pm 1\sigma$ ) on the expected significance.

1474

## Chapter 5

1475

# Summary and Conclusions

1476 The  $tWZ$  process is an important process in the search for new physics since its cross section is sensitive to  
 1477 the charged and neutral couplings to the top quark, which is strongly coupled to the Higgs boson. The top  
 1478 quark's couplings are modified in many scenarios of new physics that aim to resolve the Hierarchy Problem,  
 1479 therefore a constraint placed on the cross section of  $tWZ$  is expected to be impactful in constraining such  
 1480 BSM models. A search for  $tWZ$  production using  $139 \text{ fb}^{-1}$  of  $pp$  collision data at a centre-of-mass energy  
 1481 of  $\sqrt{s} = 13 \text{ TeV}$ , recorded by the ATLAS experiment at CERN, has been presented. This thesis targeted  
 1482 the tetralepton final state channel. The dominant background processes,  $t\bar{t}Z$  and  $ZZ$  were constrained  
 1483 by the definition of  $t\bar{t}Z$  and  $ZZ$  CRs, respectively. The dominant source of fake leptons, originating  
 1484 from the  $t\bar{t}Z$  background, was constrained by the  $(tWZ)_{\text{fake}}$  CR, using the MC template method. Two  
 1485 BDTs were implemented: an object-level BDT which aims to classify between  $\ell b$  systems coming from  
 1486 top quarks and an event-level BDT which aims to discriminate between  $tWZ$  and our major backgrounds,  
 1487  $t\bar{t}Z$  and  $ZZ$ . The output from the object-level BDT was converted to an event-level variable to be used  
 1488 as input to the event-level BDT. A kinematic reconstruction algorithm,  $2\nu\text{SM}$ , was used to reconstruct  
 1489 top quarks in order to discriminate between  $tWZ$  and  $t\bar{t}Z$ . The output from this algorithm was used as  
 1490 an input variable to the event-level BDT. The BDT was shown to discriminate well between signal and  
 1491 background events. Using a modified Asimov dataset in the SRs and real data in the CRs, a blinded  
 1492 maximum-likelihood fit was performed across all regions in the tetralepton channel. The best-fit value of  
 1493 the signal strength in the tetralepton channel was,

$$\mu(tWZ) = 1.91^{+0.95}_{-0.82} \quad (5.1)$$

1494 with an expected significance of  $1.44\sigma$ . The expected upper limit on the signal strength of  $tWZ$  in the  
 1495 tetralepton channel was,

$$\mu_{up}^{\exp} = 1.61^{+2.35}_{-1.16} \quad (5.2)$$

1496 To further increase the sensitivity of this analysis to the  $tWZ$  process, a blinded maximum-likelihood fit  
 1497 was performed across all regions across the trilepton (studied in an independent analysis by Benjamin  
 1498 Warren (UCT) [99]) and tetralepton channels. The best-fit value of the signal strength across both the  
 1499 trilepton and tetralepton channels were,

$$\mu(tWZ) = 1.80^{+0.70}_{-0.65} \quad (5.3)$$

1500 with an expected significance of  $1.61\sigma$ . The expected upper limit on the signal strength of  $tWZ$  across  
1501 both the trilepton and tetralepton channels were,

$$\mu_{up}^{exp} = 1.43^{+2.04}_{-1.03} \quad (5.4)$$

1502 The results in this analysis are heavily statistically limited, it is therefore expected that future analyses  
1503 of this process, using larger datasets (such as that from the HL-LHC), would significantly improve the  
1504 results.

1505

# Bibliography

- [1] M. Aaboud et al. “Electron reconstruction and identification in the ATLAS experiment using the 2015 and 2016 LHC proton–proton collision data at  $\sqrt{s} = 13$  TeV”. In: *The European Physical Journal C* 79.8 (Aug. 2019). ISSN: 1434-6052. DOI: 10.1140/epjc/s10052-019-7140-6. URL: <http://dx.doi.org/10.1140/epjc/s10052-019-7140-6>.
- [2] M. Aaboud et al. “Measurement of the  $t\bar{t}Z$  and  $t\bar{t}W$  cross sections in proton-proton collisions at  $\sqrt{s} = 13$  TeV with the ATLAS detector”. In: *Phys. Rev. D* 99 (7 Apr. 2019), p. 072009. DOI: 10.1103/PhysRevD.99.072009. URL: <https://link.aps.org/doi/10.1103/PhysRevD.99.072009>.
- [3] Aaboud, M. and Aad, G. and Abbott, B. and Abbott, D. C. and Abdinov, O. and Abed Abud, A. and Abhayasinghe, D. K. and Abidi, S. H. and AbouZeid, O. S. and et al. “Measurement of ZZ production in the  $\ell\ell\nu\nu$  final state with the ATLAS detector in pp collisions at  $s \sqrt{s} = 13$  TeV”. In: *Journal of High Energy Physics* 2019.10 (Oct. 2019). ISSN: 1029-8479. DOI: {10.1007/jhep10(2019)127}. URL: %7B[http://dx.doi.org/10.1007/JHEP10\(2019\)127](http://dx.doi.org/10.1007/JHEP10(2019)127)%7D.
- [4] G. Aad et al. “Measurement of the  $t\bar{t}$  production cross-section in the lepton+jets channel at  $s=13$  TeV with the ATLAS experiment”. In: *Physics Letters B* 810 (2020), p. 135797. ISSN: 0370-2693. DOI: <https://doi.org/10.1016/j.physletb.2020.135797>. URL: <https://www.sciencedirect.com/science/article/pii/S0370269320306006>.
- [5] G. Aad et al. “Muon reconstruction performance of the ATLAS detector in proton–proton collision data at  $\sqrt{s} = 13$  TeV”. In: *The European Physical Journal C* 76.5 (May 2016). ISSN: 1434-6052. DOI: 10.1140/epjc/s10052-016-4120-y. URL: <http://dx.doi.org/10.1140/epjc/s10052-016-4120-y>.
- [6] Shunichi Akatsuka and Shion Chen. *Isolation WPs summary: PLV + LowPtPLV*. Oct. 2019. URL: [https://indico.cern.ch/event/854783/contributions/3595486/attachments/1929380/3195230/PLV\\_Summary.pdf](https://indico.cern.ch/event/854783/contributions/3595486/attachments/1929380/3195230/PLV_Summary.pdf).
- [7] G. ALTARELLI, R. BARBIERI, and F. CARAVAGLIOS. “ELECTROWEAK PRECISION TEST: A CONCISE REVIEW”. In: *International Journal of Modern Physics A* 13.07 (Mar. 1998), pp. 1031–1058. ISSN: 1793-656X. DOI: 10.1142/s0217751x98000469. URL: <http://dx.doi.org/10.1142/S0217751X98000469>.
- [8] Guido Altarelli. *The Higgs and the Excessive Success of the Standard Model*. 2014. arXiv: 1407.2122 [hep-ph].

- [9] J. Alwall et al. “The automated computation of tree-level and next-to-leading order differential cross sections, and their matching to parton shower simulations”. In: *JHEP* 07 (2014), p. 079. DOI: 10.1007/JHEP07(2014)079. arXiv: 1405.0301 [hep-ph].
- [10] Aaron Armbruster. *Asymptotic Formulae*. Feb. 2013. URL: [https://indico.cern.ch/event/233551/contributions/493678/attachments/389871/542293/asymptotics\\_armbruster.pdf](https://indico.cern.ch/event/233551/contributions/493678/attachments/389871/542293/asymptotics_armbruster.pdf).
- [11] Pierre Astier et al. “Kalman filter track fits and track breakpoint analysis”. In: *Nuclear Instruments and Methods in Physics Research Section A: Accelerators, Spectrometers, Detectors and Associated Equipment* 450.1 (2000), pp. 138–154. ISSN: 0168-9002. DOI: [https://doi.org/10.1016/S0168-9002\(00\)00154-6](https://doi.org/10.1016/S0168-9002(00)00154-6). URL: <https://www.sciencedirect.com/science/article/pii/S0168900200001546>.
- [12] ATLAS Collaboration. “ATLAS  $b$ -jet identification performance and efficiency measurement with  $t\bar{t}$  events in  $pp$  collisions at  $\sqrt{s} = 13\text{TeV}$ ”. In: *Eur. Phys. J. C* 79 (2019), p. 970. DOI: 10.1140/epjc/s10052-019-7450-8. arXiv: 1907.05120 [hep-ex].
- [13] ATLAS Collaboration. “Electron and photon performance measurements with the ATLAS detector using the 2015–2017 LHC proton-proton collision data”. In: *JINST* 14 (2019), P12006. DOI: 10.1088/1748-0221/14/12/P12006. arXiv: 1908.00005 [hep-ex].
- [14] ATLAS Collaboration. “Identification and rejection of pile-up jets at high pseudorapidity with the ATLAS detector”. In: *Eur. Phys. J. C* 77 (2017), p. 580. DOI: 10.1140/epjc/s10052-017-5081-5. arXiv: 1705.02211 [hep-ex].
- [15] ATLAS Collaboration. “Measurements of  $b$ -jet tagging efficiency with the ATLAS detector using  $t\bar{t}$  events at  $\sqrt{s} = 13\text{TeV}, \text{TeV}$ ”. In: *JHEP* 08 (2018), p. 089. DOI: 10.1007/JHEP08(2018)089. arXiv: 1805.01845 [hep-ex].
- [16] ATLAS Collaboration. “Muon reconstruction and identification efficiency in ATLAS using the full Run 2  $pp$  collision data set at  $\sqrt{s} = 13\text{TeV}$ ”. In: (2020). arXiv: 2012.00578 [hep-ex].
- [17] Manuel Guth on behalf of the ATLAS collaboration. *Deep-Neural-Network-based  $b$ -Tagging as Basis for Improvements in Top Analyses*. URL: <https://cds.cern.ch/record/2693088/files/ATL-PHYS-SLIDE-2019-751.pdf>.
- [18] ATLAS Internal. *Electron Efficiencies for Analyses*. 2021. URL: <https://twiki.cern.ch/twiki/bin/viewauth/AtlasProtected/ElectronEfficienciesForAnalysis>.
- [19] ATLAS Internal. *Electron Efficiency Correlation Model*. 2021. URL: <https://twiki.cern.ch/twiki/bin/view/AtlasProtected/ElectronEfficiencyCorrelationModel>.
- [20] ATLAS Internal. *Jet Vertex Tagger for Run 2 in reco and analysis*. 2021. URL: <https://twiki.cern.ch/twiki/bin/view/AtlasProtected/JetVertexTaggerTool>.
- [21] ATLAS Internal. *Muon Efficiencies for Analyses*. 2021. URL: <https://twiki.cern.ch/twiki/bin/view/AtlasProtected/MuonEfficienciesForAnalysis>.
- [22] G. Avoni et al. “The new LUCID-2 detector for luminosity measurement and monitoring in ATLAS”. In: *JINST* 13.07 (2018), P07017. DOI: 10.1088/1748-0221/13/07/P07017.

- [23] Richard D. Ball et al. “Parton distributions for the LHC run II”. In: *Journal of High Energy Physics* 2015.4 (Apr. 2015). ISSN: 1029-8479. DOI: 10.1007/jhep04(2015)040. URL: [http://dx.doi.org/10.1007/JHEP04\(2015\)040](http://dx.doi.org/10.1007/JHEP04(2015)040).
- [24] Roger Barlow and Christine Beeston. “Fitting using finite Monte Carlo samples”. In: *Computer Physics Communications* 77.2 (1993), pp. 219–228. ISSN: 0010-4655. DOI: [https://doi.org/10.1016/0010-4655\(93\)90005-W](https://doi.org/10.1016/0010-4655(93)90005-W). URL: <https://www.sciencedirect.com/science/article/pii/001046559390005W>.
- [25] Olga Bessidskaia Bylund. *Measurement of ttZ and ttW production at ATLAS in 13 TeV data, using trilepton and same charge dimuon final states*. Tech. rep. Geneva: CERN, Aug. 2016. DOI: 10.22323/1.276.0237. URL: <http://cds.cern.ch/record/2211022>.
- [26] Enrico Bothmann et al. “Event generation with Sherpa 2.2”. In: *SciPost Physics* 7.3 (Sept. 2019). ISSN: 2542-4653. DOI: 10.21468/scipostphys.7.3.034. URL: <http://dx.doi.org/10.21468/SciPostPhys.7.3.034>.
- [27] Ilaria Brivio and Michael Trott. “The standard model as an effective field theory”. In: *Physics Reports* 793 (Feb. 2019), pp. 1–98. ISSN: 0370-1573. DOI: 10.1016/j.physrep.2018.11.002. URL: <http://dx.doi.org/10.1016/j.physrep.2018.11.002>.
- [28] Jason Brownlee. *Overfitting and Underfitting With Machine Learning Algorithms*. URL: <https://machinelearningmastery.com/overfitting-and-underfitting-with-machine-learning-algorithms/>.
- [29] Oliver Sim Brüning et al. *LHC Design Report*. CERN Yellow Reports: Monographs. Geneva: CERN, 2004. DOI: 10.5170/CERN-2004-003-V-1. URL: <https://cds.cern.ch/record/782076>.
- [30] Gustavo Burdman et al. “Colorless top partners, a 125 GeV Higgs boson, and the limits on naturalness”. In: *Physical Review D* 91.5 (Mar. 2015). ISSN: 1550-2368. DOI: 10.1103/physrevd.91.055007. URL: <http://dx.doi.org/10.1103/PhysRevD.91.055007>.
- [31] Matteo Cacciari, Gavin P. Salam, and Gregory Soyez. “The anti- $k_t$  jet clustering algorithm”. In: *JHEP* 04 (2008), p. 063. DOI: 10.1088/1126-6708/2008/04/063. arXiv: 0802.1189 [hep-ph].
- [32] Thomas Calvet. *Automatic binning implementation in TTHFitter - Htop(bb)*. URL: [https://indico.cern.ch/event/455289/contributions/1953694/attachments/1209081/1762963/Calvet\\_binning\\_Htop\\_160108.pdf](https://indico.cern.ch/event/455289/contributions/1953694/attachments/1209081/1762963/Calvet_binning_Htop_160108.pdf).
- [33] Thomas Philippe Calvet. “Search for the production of a Higgs boson in association with top quarks and decaying into a b-quark pair and b-jet identification with the ATLAS experiment at LHC”. Presented 08 Nov 2017. Dec. 2017. URL: <https://cds.cern.ch/record/2296985>.
- [34] Anadi Canepa. “Searches for supersymmetry at the Large Hadron Collider”. In: *Reviews in Physics* 4 (2019), p. 100033. ISSN: 2405-4283. DOI: <https://doi.org/10.1016/j.revip.2019.100033>. URL: <https://www.sciencedirect.com/science/article/pii/S2405428318300091>.
- [35] *CERN Twiki - TOP WG Summary Plots*. URL: <https://twiki.cern.ch/twiki/bin/view/LHCPhysics/LHCTopWGSummaryPlots>.

- [36] CERN Yellow Reports: Monographs. *CERN Yellow Reports: Monographs, Vol. 10 (2020): High-Luminosity Large Hadron Collider (HL-LHC): Technical design report.* en. 2020. DOI: 10.23731/CYRM-2020-0010. URL: <https://e-publishing.cern.ch/index.php/CYRM/issue/view/127>.
- [37] Shion Chen. *Track isolation variable for the PFlow WPs.* Oct. 2019. URL: [https://indico.cern.ch/event/854783/contributions/3595529/attachments/1926980/3190772/IFF\\_20191003\\_PflowWPs.pdf](https://indico.cern.ch/event/854783/contributions/3595529/attachments/1926980/3190772/IFF_20191003_PflowWPs.pdf).
- [38] KyungEon Choi. “Tracking and Vertexing with the ATLAS Inner Detector in the LHC Run-2”. In: *Springer Proc. Phys.* 213 (2018). Ed. by Zhen-An Liu, pp. 400–403. DOI: 10.1007/978-981-13-1316-5\_75.
- [39] CMS Collaboration. *Measurements of  $pp \rightarrow ZZ$  production cross sections and constraints on anomalous triple gauge couplings at  $\sqrt{s} = 13$  TeV.* 2020. arXiv: {2009.01186} (hep-ex).
- [40] CMS Collaboration. “Measurement of the ttbar production cross section using events with one lepton and at least one jet in pp collisions at  $\sqrt{s}=13$  TeV”. In: (Jan. 2017).
- [41] The ATLAS Collaboration et al. “The ATLAS Experiment at the CERN Large Hadron Collider”. In: *Journal of Instrumentation* 3.08 (Aug. 2008), S08003–S08003. DOI: 10.1088/1748-0221/3/08/s08003. URL: <https://doi.org/10.1088/1748-0221/3/08/s08003>.
- [42] I. Connelly. “Performance and calibration of b-tagging with the ATLAS experiment at LHC Run-2”. In: 2017.
- [43] Glen Cowan et al. “Asymptotic formulae for likelihood-based tests of new physics”. In: *The European Physical Journal C* 71.2 (Feb. 2011). ISSN: 1434-6052. DOI: 10.1140/epjc/s10052-011-1554-0. URL: <http://dx.doi.org/10.1140/epjc/s10052-011-1554-0>.
- [44] Federico Demartin et al. “tWH associated production at the LHC”. In: *Eur. Phys. J. C* 77.1 (2017), p. 34. DOI: 10.1140/epjc/s10052-017-4601-7. arXiv: 1607.05862 [hep-ph].
- [45] *Electron identification efficiency in data for electrons with  $E_T > 30\text{GeV}$ .* URL: [https://atlas.web.cern.ch/Atlas/GROUPS/PHYSICS/PAPERS/EGAM-2018-01/fig\\_16.png](https://atlas.web.cern.ch/Atlas/GROUPS/PHYSICS/PAPERS/EGAM-2018-01/fig_16.png).
- [46] F. Englert and R. Brout. “Broken Symmetry and the Mass of Gauge Vector Mesons”. In: *Phys. Rev. Lett.* 13 (9 Aug. 1964), pp. 321–323. DOI: 10.1103/PhysRevLett.13.321. URL: <https://link.aps.org/doi/10.1103/PhysRevLett.13.321>.
- [47] *Errors in weighted histograms.* URL: <https://www.zeuthen.desy.de/~wischnew/amanda/discussion/wgterror/working.html>.
- [48] Lyndon Evans and Philip Bryant. “LHC Machine”. In: *Journal of Instrumentation* 3.08 (Aug. 2008), S08001–S08001. DOI: 10.1088/1748-0221/3/08/s08001. URL: <https://doi.org/10.1088/1748-0221/3/08/s08001>.
- [49] Guido Fantini et al. *The formalism of neutrino oscillations: an introduction.* 2020. arXiv: 1802.05781 [hep-ph].

- [50] *Forward Jet Vertex Tagging: A new technique for the identification and rejection of forward pileup jets*. Tech. rep. All figures including auxiliary figures are available at <https://atlas.web.cern.ch/Atlas/GROUPS/PHYSICS/PUBNOTES/ATL-PHYS-PUB-2015-034>. Geneva: CERN, Aug. 2015. URL: <https://cds.cern.ch/record/2042098>.
- [51] Stefano Frixione, Paolo Nason, and Carlo Oleari. “Matching NLO QCD computations with parton shower simulations: the POWHEG method”. In: *JHEP* 11 (2007), p. 070. DOI: 10.1088/1126-6708/2007/11/070. arXiv: 0709.2092 [hep-ph].
- [52] Michele Gallinaro. “Top quark physics: A tool for discoveries”. In: *Journal of Physics Conference Series* 447 (July 2013), pp. 2012–. DOI: 10.1088/1742-6596/447/1/012012.
- [53] *Good Run Lists for Analysis Run 2 - ATLAS Twiki*. URL: <https://twiki.cern.ch/twiki/bin/viewauth/AtlasProtected/GoodRunListsForAnalysisRun2>.
- [54] *GoodRunListsForAnalysisRun2*. URL: <https://twiki.cern.ch/twiki/bin/viewauth/AtlasProtected/GoodRunListsForAnalysisRun2>.
- [55] Particle Data Group et al. “Review of Particle Physics”. In: *Progress of Theoretical and Experimental Physics* 2020.8 (Aug. 2020). 083C01. ISSN: 2050-3911. DOI: 10.1093/ptep/ptaa104. eprint: <https://academic.oup.com/ptep/article-pdf/2020/8/083C01/33653179/ptaa104.pdf>. URL: <https://doi.org/10.1093/ptep/ptaa104>.
- [56] Trevor Hastie. *The elements of statistical learning : data mining, inference, and prediction*. New York: Springer, 2009. ISBN: 978-0-387-84858-7.
- [57] Peter W. Higgs. “Broken Symmetries and the Masses of Gauge Bosons”. In: *Phys. Rev. Lett.* 13 (1964). Ed. by J. C. Taylor, pp. 508–509. DOI: 10.1103/PhysRevLett.13.508.
- [58] Peter W. Higgs. “Spontaneous Symmetry Breakdown without Massless Bosons”. In: *Phys. Rev.* 145 (1966), pp. 1156–1163. DOI: 10.1103/PhysRev.145.1156.
- [59] *IFFTruthClassifier GitLab Repository*. URL: <https://gitlab.cern.ch/ATLAS-IFF/IFFTruthClassifier/-/tree/master>.
- [60] *IFFTruthClassifier Lepton Categories*. URL: <https://gitlab.cern.ch/ATLAS-IFF/IFFTruthClassifier/-/tree/master#3-details-about-the-lepton-categories>.
- [61] N. Jarosik et al. “SEVEN-YEAR WILKINSON MICROWAVE ANISOTROPY PROBE ( WMAP ) OBSERVATIONS: SKY MAPS, SYSTEMATIC ERRORS, AND BASIC RESULTS”. In: *The Astrophysical Journal Supplement Series* 192.2 (Jan. 2011), p. 14. ISSN: 1538-4365. DOI: 10.1088/0067-0049/192/2/14. URL: <http://dx.doi.org/10.1088/0067-0049/192/2/14>.
- [62] F. Jegerlehner. “The hierarchy problem of the electroweak Standard Model revisited”. In: (May 2013).
- [63] V. Khachatryan et al. “Measurement of the ZZ production cross section and  $Z \rightarrow \ell^+\ell^-\ell^+\ell^-$  branching fraction in pp collisions at  $\sqrt{s} = 13\text{TeV}$ ”. In: *Physics Letters B* 763 (2016), pp. 280–303. ISSN: 0370-2693. DOI: <https://doi.org/10.1016/j.physletb.2016.10.054>. URL: <https://www.sciencedirect.com/science/article/pii/S0370269316306256>.

- [64] H. J. W. Kirsten. *Introduction to supersymmetry*. Singapore Hackensack, NJ: World Scientific, 2010. ISBN: 978-9814293426.
- [65] Arthur Alexis Jules Lesage. *Lepton and photon performance at ATLAS and CMS*. 2017. arXiv: 1709.02598 [hep-ex].
- [66] Fabio Maltoni, Luca Mantani, and Ken Mimasu. “Top-quark electroweak interactions at high energy”. In: *Journal of High Energy Physics* 2019.10 (Oct. 2019). ISSN: 1029-8479. DOI: 10.1007/jhep10(2019)004. URL: [http://dx.doi.org/10.1007/JHEP10\(2019\)004](http://dx.doi.org/10.1007/JHEP10(2019)004).
- [67] Luigi Marchese. *Lepton and photon reconstruction and identification performance in ATLAS and CMS*. Tech. rep. Geneva: CERN, Sept. 2019. DOI: 10.22323/1.350.0237. URL: <https://cds.cern.ch/record/2688452>.
- [68] Thomas McCarthy. *Macro developed to compare t/W/Z reconstruction performance (2ℓ, 3ℓ, 4ℓ)*. URL: [https://indico.cern.ch/event/986357/contributions/4172907/attachments/2169451/3666801/reco\\_performance\\_macro\\_20210112.pdf](https://indico.cern.ch/event/986357/contributions/4172907/attachments/2169451/3666801/reco_performance_macro_20210112.pdf).
- [69] Thomas McCarthy and Florian Fischer. *Exploiting full/partial  $t\bar{t}$  reconstruction for background suppression in  $2\ell$* . URL: [https://indico.cern.ch/event/955360/contributions/4016465/attachments/2102418/3534816/top\\_reco\\_bkgd\\_suppression\\_2L\\_20200915.pdf](https://indico.cern.ch/event/955360/contributions/4016465/attachments/2102418/3534816/top_reco_bkgd_suppression_2L_20200915.pdf).
- [70] *MCTruthClassifier - ATLAS Twiki*. URL: <https://twiki.cern.ch/twiki/bin/view/AtlasProtected/MCTruthClassifier>.
- [71] *Measurement of the  $t\bar{t}$  production cross-section and lepton differential distributions in  $e\mu$  dilepton events from  $pp$  collisions at  $\sqrt{s} = 13$  TeV with the ATLAS detector*. Tech. rep. All figures including auxiliary figures are available at <https://atlas.web.cern.ch/Atlas/GROUPS/PHYSICS/CONFNOTES/ATLAS-CONF-2019-041>. Geneva: CERN, Aug. 2019. URL: <https://cds.cern.ch/record/2686255>.
- [72] F. Meloni. “Primary vertex reconstruction with the ATLAS detector”. In: *Journal of Instrumentation* 11.12 (Dec. 2016), pp. C12060–C12060. DOI: 10.1088/1748-0221/11/12/c12060. URL: <https://doi.org/10.1088/1748-0221/11/12/c12060>.
- [73] Ken Mimasu. *Top quark electroweak interactions*. 2021. arXiv: 2105.10261 [hep-ph].
- [74] Aditya Mishra. *Metrics to Evaluate your Machine Learning Algorithm*. URL: <https://towardsdatascience.com/metrics-to-evaluate-your-machine-learning-algorithm-f10ba6e38234>.
- [75] Users MissMJ and Cush. *Standard model of elementary particles - Wikimedia Commons*. URL: [https://en.wikipedia.org/wiki/File:Standard\\_Model\\_of\\_Elementary\\_Particles.svg](https://en.wikipedia.org/wiki/File:Standard_Model_of_Elementary_Particles.svg).
- [76] *Monte Carlo to Monte Carlo scale factors for flavour tagging efficiency calibration*. Tech. rep. ATL-PHYS-PUB-2020-009. Geneva: CERN, May 2020. URL: <https://cds.cern.ch/record/2718610>.
- [77] Hussain Mujtaba. *What is Cross Validation in Machine learning? Types of Cross Validation*. URL: <https://www.mygreatlearning.com/blog/cross-validation/>.
- [78] *MuonSelectionTool, ATLAS TWiki*. URL: <https://twiki.cern.ch/twiki/bin/view/Atlas/MuonSelectionTool>.

- [79] O. Ogul Oncel. “Search for Single Top Quark Production in Association with a  $W$  and a  $Z$  Boson in the 3 Lepton Final State with the ATLAS Experiment at 13 TeV”. Presented 04 Jun 2018. May 2018. URL: <http://cds.cern.ch/record/2625170>.
- [80] António Onofre. “Top Quark Couplings and Search for New Physics at the LHC”. In: *Journal of Physics Conference Series* 447 (July 2013), pp. 2030–. DOI: 10.1088/1742-6596/447/1/012030.
- [81] *Option to force a shape withing an error band by hand - TRF documentation*. URL: [https://trexfitter-docs.web.cern.ch/trexfitter-docs/model\\_building/shape/](https://trexfitter-docs.web.cern.ch/trexfitter-docs/model_building/shape/).
- [82] *Performance of the ATLAS Electron and Photon Trigger in p-p Collisions at  $\sqrt{s} = 7$  TeV in 2011*. Tech. rep. All figures including auxiliary figures are available at <https://atlas.web.cern.ch/Atlas/GROUPS/PHYSICS/CONFNOTES/ATLAS-CONF-2012-048>. Geneva: CERN, May 2012. URL: <https://cds.cern.ch/record/1450089>.
- [83] *Pileup jet recommendations*. URL: <https://twiki.cern.ch/twiki/bin/view/AtlasProtected/PileupJetRecommendations>.
- [84] Michele Pinamonti. *Statistical methods at ATLAS and CMS*. URL: [https://indico.cern.ch/event/727396/contributions/3021899/attachments/1657532/2654085/Statistical\\_methods\\_at\\_ATLAS\\_and\\_CMS\\_2.pdf](https://indico.cern.ch/event/727396/contributions/3021899/attachments/1657532/2654085/Statistical_methods_at_ATLAS_and_CMS_2.pdf).
- [85] *Recommended isolation working points*. URL: <https://twiki.cern.ch/twiki/bin/view/AtlasProtected/RecommendedIsolationWPs>.
- [86] *scikit-learn Documentation - Gradient Boosting Classifier*. URL: <https://scikit-learn.org/stable/modules/generated/sklearn.ensemble.GradientBoostingClassifier.html>.
- [87] *Scikit-Learn GradientBoostingClassifier Documentation*. URL: <https://scikit-learn.org/stable/modules/generated/sklearn.ensemble.GradientBoostingClassifier.html>.
- [88] Pedro Ferreira da Silva. *Top quark production at the LHC*. 2016. arXiv: 1605.05343 [hep-ex].
- [89] T. Sjöstrand, S. Mrenna, and P. Skands. “A brief introduction to PYTHIA 8.1”. In: *Comput. Phys. Commun.* 178 (2008), pp. 852–867. DOI: 10.1016/j.cpc.2008.01.036. arXiv: 0710.3820 [hep-ph].
- [90] Torbjörn Sjöstrand et al. “An introduction to PYTHIA 8.2”. In: *Comput. Phys. Commun.* 191 (2015), p. 159. DOI: 10.1016/j.cpc.2015.01.024. arXiv: 1410.3012 [hep-ph].
- [91] Jory Sonneveld. *Searches for physics beyond the standard model at the LHC*. 2019. arXiv: 1905.06239 [hep-ex].
- [92] Mark Thomson. *Modern particle physics*. Cambridge, United Kingdom New York: Cambridge University Press, 2013. ISBN: 9781107034266.
- [93] *TopRecoObjTwikiModel*. URL: <https://twiki.cern.ch/twiki/bin/view/AtlasProtected/TopRecoObjTwikiModel>.
- [94] *Total Integrated Luminosity and Data Quality in 2015-2018 - LuminosityPublicResultsRun2*. URL: <https://twiki.cern.ch/twiki/bin/view/AtlasPublic/LuminosityPublicResultsRun2>.

- 1755 [95] Daniel R. Tovey. “Transformation properties of the transverse mass under transverse Lorentz  
1756 boosts at hadron colliders”. In: *The European Physical Journal C* 79.4 (Apr. 2019). ISSN: 1434-6052.  
1757 DOI: 10.1140/epjc/s10052-019-6813-5. URL: <http://dx.doi.org/10.1140/epjc/s10052-019-6813-5>.
- 1759 [96] *TRExFitter*. URL: <https://twiki.cern.ch/twiki/bin/viewauth/AtlasProtected/TtHFitter>.
- 1760 [97] *TRExFitter: Mixed data and MC fit*. URL: <https://trexfitter-docs.web.cern.ch/trexfitter-docs/AdvancedTutorial2020/Mixed/>.
- 1762 [98] Tommy Tschida. “Cross section measurements of processes with a single top quark and two vector  
1763 bosons with the CMS experiment”. MA thesis. Vienna, Tech. U., 2020. DOI: 10.34726/hss.2020.  
1764 79420.
- 1765 [99] Benjamin Warren. “A search for tWZ production in the trilepton channel using Run 2 data from  
1766 the ATLAS experiment.” In: (2021).
- 1767 [100] Kenneth G. Wilson. “Confinement of quarks”. In: *Phys. Rev. D* 10 (8 Oct. 1974), pp. 2445–2459.  
1768 DOI: 10.1103/PhysRevD.10.2445. URL: <https://link.aps.org/doi/10.1103/PhysRevD.10.2445>.
- 1770 [101] Katherine Woodruff. *Introduction to boosted decision trees*. URL: <https://indico.fnal.gov/event/15356/contributions/31377/attachments/19671/24560/DecisionTrees.pdf>.